

國立交通大學

機械工程學系

碩士論文

利用流體體積法之雙流體計算

Calculation of Two-Fluids Flow

Using Volume-of-Fluid Method



研究生：鄭東庭

指導教授：崔燕勇博士

中華民國九十六年七月

利用流體體積法之雙流體計算

Calculation of Two-Fluids Flow Using Volume-of-Fluid Method

研 究 生：鄭 東 庭

Student : Tong-Ting Cheng

指導教授：崔 燕 勇

Advisor : Yeng-Yung Tsui

國立交通大學

機械工程研究所

碩士論文



Submitted to Institute of Mechanical Engineering

Collage of Engineering

National Chiao Tung University

In Partial Fulfillment of the Requirements

For the degree of

Master of Science

In

Mechanical Engineering

July 2007

Hsinchu, Taiwan, Republic of China

國立交通大學

論文口試委員會審定書

本校 機械工程 學系碩士班 鄭東庭 君

所提論文(中文)利用流體體積法之雙流體計算

(英文)Calculation of Two-Fluids Flow Using
Volume-of-Fluid Method

合於碩士資格水準、業經本委員會評審認可。

口試委員：黃如 陳俊逸
傅武雄 崔燕亭

指導教授：崔燕亭

系主任：周學 教授

中華民國 96 年 7 月 16 日

Calculation of Two-Fluids Flow Using Volume-of-Fluid Method

Student : Tong-Ting Cheng

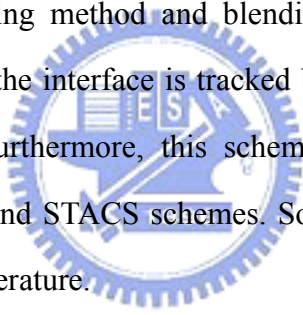
Advisor : Prof. Yeng-Yung Tsui

Institute of Mechanical Engineering

National Chiao Tung University

ABSTRACT

In two fluid flow investigation, the simulation of flows with free surfaces is difficult because neither the shape nor the position of the interface can be identifies in advance between two immiscible fluids. The aim of this study is to develop a scheme, which ensures the preservation of the sharpness and the shape of the interface while retaining boundedness of the field, by volume tracking method and blending strategy without explicit interface reconstruction. The motion of the interface is tracked by the solution of a transport equation for a phase-indicator field. Furthermore, this scheme is formed and compared with the well-known HRIC, CICSAM and STACS schemes. Some favorable cases are simulated and comparisons are made in the literature.



利用流體體積法之雙流體計算

研究生 鄭東庭

指導教授 崔燕勇 博士

國立交通大學機械工程學系

摘要

在雙流體之研究中，在模擬流場時兩不互溶流體之自由液面的位置與形狀難以去確認。本研究之目的為以流體體積法及混合策略建立一模擬架構，且不需經由以重建自由液面之方式，以期能保持自由液面形狀之明確性並符合流場中之邊界性。而流場中自由液面之運動乃經由求解一傳輸方程式所得。更進一步地，在模擬架構建立之後，將與前人所發展之方法比較，如 Muzaferija 提出之 HRIC 法、Ubbink 提出之 CICSAM 法、以及 Dariwish 所提出之 STACS 法。另外，此架構將應用在一些案例，並與實驗成果及前人數值模擬之結果作比較。

Acknowledgments

I would like to express my deepest gratitude to my supervisor, Prof. Yeng-Youg Tsui, for his constructive criticism, guidance provided throughout my research, patience and continuous support. I've learned the research methods and attitudes from his instruction during the two-year courses.

I would like to thank all the members and previous members of CFD Laboratory. Thanks to the senior students, Yu-Chang Hu and Tian-Cherng Wu for their suggestion and guidance. They helped me solve many problems and introduced me good research directions. Thanks to Eatrol Lu for his great help and companion. We built a good friendship during the two years. It's definitely too hard to forget the time we work together, especially the month before oral presentation.

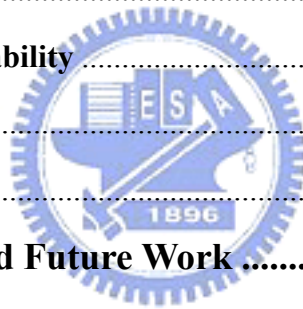
I would like to thank all the members of Ballroom Dance Club in our school. Dancing is the most important and stress-releasing recreation in my leisure time. Y-Ching Cheng, Yun-Yun Song, Deniel Wu and Jing-Wen Wu are all famous dancers. Thanks to them for teaching me to dance. Thanks to Gloria Lin and Jamin Chang. We gave good performances together.

Finally, I would like to thank my family for their support and encouragement. Thanks to my uncle Wen-Fong Cheng and Sunny Gao. I really appreciate that they taught me the style of handling problem and getting along with people. I am also so appreciated my dad Wen-Yao Cheng, my mom Yue-Feng Chen, my brother Andy Cheng and my girlfriend Karen Liu. They are the most important spiritual support in my whole life.

Content

ABSTRACT	i
Content	iv
List of Figures	vi
Nomenclature.....	x
Abbreviation	xii
Chapter 1 Introduction.....	1
1.1 Background	1
1.2 Related Studies.....	1
1.3 Present study of this thesis	7
Chapter 2 Mathematical Model.....	9
2.1 Introduction	9
2.2 General transport equation.....	9
2.3 Governing equations	10
Mass conservation	10
2.4 Surface tension.....	12
2.5 Boundary Conditions	14
2.6 Closure.....	14
Chapter 3 Numerical Method for the VOF Equation.....	15
3.1 Introduction	15
3.2 The approximation for the face value of α	15
3.3 Linear difference schemes.....	17
3.4 Non-linear difference schemes.....	19
3.5 The normalized variables for unstructured-grids	24
3.6 Discretization of the indicator equation	25
3.7 Blending strategy	27
Chapter 4 Numerical Method for the Velocity Field	32

4.1 Introduction	32
4.2 Discretization	32
4.3 Pressure-velocity coupling with PISO	35
4.4 Solution procedure for the two-fluid system	40
Chapter 5 Results and Discussion.....	41
5.1 Introduction	41
5.2 The VOF schemes test in an oblique velocity field.....	41
5.3 Surface tension.....	59
5.4 Drop splash.....	62
5.5 Bubble.....	65
5.6 Sloshing.....	68
5.7 Rayleigh-Taylor instability.....	74
5.8 Column collapse.....	93
5.9 Hydraulic bore	113
Chapter 6 Conclusion and Future Work	120
Reference.....	121



List of Figures

FIGURE 1.1 (A) SURFACE METHODS (B) VOLUME METHODS	2
FIGURE 1.2 SCHEMATIC REPRESENTATION OF MARKER AND CELL MESH LAYOUT.....	3
FIGURE 1.3 INTERFACE RECONSTRUCTIONS OF (A) ACTUAL FLUID CONFIGURATION, (B) SLIC IN X-DIRECTION, (C) SLIC IN Y-DIRECTION (D) YOUNGS' VOF.....	4
FIGURE 2.1 GENERAL FORM OF THE CONSERVATION LAW	10
FIGURE 2.2 FLUIDS ARE MARKED WITH INDICATOR FUNCTION	11
FIGURE 2.3 CONTINUITY OF THE VELOCITY FIELD AND DISCONTINUITY OF THE MOMENTUM.....	12
FIGURE 2.4 FLUID ARRANGEMENT AND THE SIGN OF THE CURVATURE	13
FIGURE 3.1 THE RELATIONSHIP OF A CONTROL VOLUME AND ITS NEIGHBOR CELLS.....	15
FIGURE 3.2 NORMALIZED VARIABLE DIAGRAM (NVD).	17
FIGURE 3.3 RELATIONSHIP BETWEEN γ AND r FOR LINEAR DIFFERENCE SCHEMES.	19
FIGURE 3.4 TVD CONSTRAINTS IN (A) NVD AND (B) TVD DIAGRAM.....	20
FIGURE 3.5 SMART	22
FIGURE 3.6 MUSCL.....	22
FIGURE 3.7 SUPERBEE	22
FIGURE 3.8 STOIC	23
FIGURE 3.9 OSHER	23
FIGURE 3.10 BDS.....	23
FIGURE 3.11 VAN LEER	24
FIGURE 3.12 CHARM.....	24
FIGURE 3.13. THE PREDICTION OF UPWIND VALUE FOR AN ARBITRARY CELL ARRANGEMENT	25
FIGURE 3.14 (A) THE INTERFACE IS PARALLEL TO THE FLOW DIRECTION AND THE COMPRESSIVE SCHEME WILL BE USED (B) THE INTERFACE IS PERPENDICULAR TO THE FLOW DIRECTION AND HIGH RESOLUTION SCHEMES ARE APPROPRIATE.	27
FIGURE 3.15 THE NVD OF (A) HYPER-C AND (B) UQ AT Co_f EQUAL 0.5	29
FIGURE 3.16A, 3.16B AND 3.16C SHOW THE RELATIONSHIP BETWEEN TWO SCHEMES FOR HRIC, CICSAM AND STACS. THE X-AXIS STAND FOR θ_f AND Y-AXIS MEANS THE VALUE OF $f(\theta_f)$	31
FIGURE 4.1 ILLUSTRATION OF THE PRIMARY CELL P AND THE NEIGHBOR CELL NB WITH A CONSIDER FACE F.....	33
FIGURE 5.1 THE FLOW FIELD DOMAIN AND INITIAL CONDITION OF (A) HOLLOW SQUARE, (B) HOLLOW CIRCLE	43
FIGURE 5.3 (A) COMPARISON OF DIFFERENT SCHEMES WITH GRIDS 100*100 AND COURANT NUMBER=0.75 ($\Delta T=0.01$).....	45
FIGURE 5.3(B) COMPARISON OF DIFFERENT SCHEMES WITH GRIDS 100*100 AND COURANT NUMBER=0.50 ($\Delta T=0.00667$).....	46
FIGURE 5.3(C) COMPARISON OF DIFFERENT SCHEMES WITH GRIDS 100*100 AND COURANT NUMBER=0.25 ($\Delta T=0.00333$).....	47
FIGURE 5.4(A) COMPARISON OF DIFFERENT SCHEMES WITH GRIDS 100*100 AND COURANT NUMBER=0.75 ($\Delta T=0.01$).....	48
FIGURE 5.4(B) COMPARISON OF DIFFERENT SCHEMES WITH GRIDS 100*100 AND COURANT NUMBER=0.50	

($\Delta t=0.00667$)	49
FIGURE 5.4(C) COMPARISON OF DIFFERENT SCHEMES WITH GRIDS 100*100 AND COURANT NUMBER=0.25	
($\Delta t=0.00333$)	50
FIGURE 5.5 COMPARISON OF HRIC, CICSAM AND STACS WITH GRIDS 100*100.	53
FIGURE 5.6 (CONTINUE) COMPARISON OF DIFFERENT COMPOSITE SCHEMES WITH GRIDS: 100*100.....	54
FIGURE 5.6 COMPARISON OF DIFFERENT COMPOSITE SCHEMES WITH GRIDS: 100*100	55
FIGURE 5.7 COMPARISON OF HRIC, CICSAM AND STACS WITH GRIDS: 100*100.....	56
FIGURE 5.8 COMPARISON OF DIFFERENT COMPOSITE SCHEMES WITH GRIDS: 100*100	57
FIGURE 5.8 COMPARISON OF DIFFERENT COMPOSITE SCHEMES WITH GRIDS: 100*100.	58
FIGURE 5.9 TIME EVOLUTION OF THE SHAPE CHANGES OF A SQUARE SUBJECTED TO SURFACE TENSION FORCES. ...	60
FIGURE 5.10 PARASITE CURRENTS FOR DIFFERENT VISCOSITY OF FLUID 1 AND SURFACE TENSION COEFFICIENT. ...	61
FIGURE 5.11 THE WATER DROPLET FALLING AIR ONTO SURFACE AT TIMES $t=0.0s, 0.00677s, 0.00980s, 0.01220s,$ $0.01485s, 0.01781s, 0.01995s, 0.02146s.$ (BY PUCKETT ET AL. [38])	63
FIGURE 5.12 WATER DROPLET FALLING THROUGH AIR ONTO WATER SURFACE. THE TIME STEP SIZE IS 0.00005 AND COMPUTATIONAL DOMAIN IS $0.007*0.014(64*128)$. THE MAXIMUM COURANT NUMBER DURING COMPUTATION IS 0.24	64
FIGURE 5.13 TIME EVOLUTION OF AN AIR BUBBLE RISING THROUGH WATER WITHOUT SURFACE TENSION.	66
FIGURE 5.14 TIME EVOLUTION OF AN AIR BUBBLE RISING THROUGH WATER WITH SURFACE TENSION.	67
FIGURE 5.15 THE PHYSICAL MODEL OF SLOSING.....	68
FIGURE 5.16 TIME EVOLUTION OF THE WAVE POSITION AND VELOCITY VECTORS FOR THE FIRST PERIOD OF SLOSING OF AN INVISCID FLOW FIELD WHICH INFLUENCED BY GRAVITY. THE COMPUTATIONAL GRIDS ARE $160*104$. THE MAXIMUM COURANT NUMBER DURING THE COMPUTATION: 0.03.....	72
FIGURE 5.17 POSITION OF THE INTERFACE AT THE LEFT BOUNDARY AGAINST THE TIME (INVISCID FLOW).	73
FIGURE 5.18 POSITION OF THE INTERFACE AT THE LEFT BOUNDARY AGAINST THE TIME (VISCOUS FLOW). THE AMPLITUDE OF SLOSING WILL DECREASE WITH THE TIME GOES BY.....	73
FIGURE 5.19(A) THE PHYSICAL MODEL OF RAYLEIGH-TAYLOR INSTABILITY. (B) THE ARRANGEMENT OF UNIFORM GRIDS ($64*192$). (C) THE ARRANGEMENT OF NON-UNIFORM GRIDS ($80*284$)	74
FIGURE 5.20 (A) THE FIRST KIND OF INITIAL CONDITION. (B) THE SECOND KIND OF INITIAL CONDITION (C) THE THIRD KIND OF INITIAL CONDITION.	76
FIGURE 5.21 THE NUMERICAL RESULTS OF RAYLEIGH-TAYLOR INSTABILITY ADOPTING 1ST KIND OF INITIAL CONDITION WITH UNIFORM GRIDS $64*192$	77
FIGURE 5.22 THE NUMERICAL RESULTS OF RAYLEIGH-TAYLOR INSTABILITY ADOPTING 1ST KIND OF INITIAL CONDITION WITH NON-UNIFORM GRIDS $80*284$	78
FIGURE 5.23 THE NUMERICAL RESULTS OF RAYLEIGH-TAYLOR INSTABILITY ADOPTING 2ND KIND OF INITIAL CONDITION WITH UNIFORM GRIDS $64*192$	79
FIGURE 5.24 THE NUMERICAL RESULTS OF RAYLEIGH-TAYLOR INSTABILITY ADOPTING 2ND KIND OF INITIAL CONDITION WITH NON-UNIFORM GRIDS $80*284$	80
FIGURE 5.25 THE NUMERICAL RESULTS OF RAYLEIGH-TAYLOR INSTABILITY ADOPT 3RD INITIAL CONDITION WITH UNIFORM GRIDS $64*192$	81
FIGURE 5.26 THE NUMERICAL RESULTS OF RAYLEIGH-TAYLOR INSTABILITY ADOPTING 3RD KIND OF INITIAL CONDITION WITH NON-UNIFORM GRIDS $80*284$	82
FIGURE 5.27 THE NUMERICAL RESULTS OF RAYLEIGH-TAYLOR INSTABILITY ADOPTING 4 TH KIND OF INITIAL	

CONDITION WITH UNIFORM GRIDS 64*192	83
FIGURE 5.28 THE NUMERICAL RESULTS OF RAYLEIGH-TAYLOR INSTABILITY ADOPTING 4 TH KIND OF INITIAL CONDITION WITH NON-UNIFORM GRIDS 80*284.	84
FIGURE 5.29 THE NUMERICAL RESULTS OF RAYLEIGH-TAYLOR INSTABILITY ADOPTING 5 TH KIND OF INITIAL CONDITION WITH UNIFORM GRIDS 64*192.	85
FIGURE 5.30 THE NUMERICAL RESULTS OF RAYLEIGH-TAYLOR INSTABILITY ADOPTING 5 TH KIND OF INITIAL CONDITION WITH NON-UNIFORM GRIDS 80*284.	86
FIGURE 5.31 THE NUMERICAL RESULTS OF RAYLEIGH-TAYLOR INSTABILITY ADOPTING 1 ST KIND OF INITIAL CONDITION WITH NON-UNIFORM GRIDS 64*192 AND SLIP BOUNDARY CONDITION.	88
FIGURE 5.32 THE NUMERICAL RESULTS OF RAYLEIGH-TAYLOR INSTABILITY ADOPTING 2 ND KIND OF INITIAL CONDITION WITH NON-UNIFORM GRIDS 64*192 AND SLIP BOUNDARY CONDITION.	89
FIGURE 5.33 THE NUMERICAL RESULTS OF RAYLEIGH-TAYLOR INSTABILITY ADOPTING 3 RD KIND OF INITIAL CONDITION WITH NON-UNIFORM GRIDS 64*192 AND SLIP BOUNDARY CONDITION.	90
FIGURE 5.34 THE NUMERICAL RESULTS OF RAYLEIGH-TAYLOR INSTABILITY ADOPTING 4 TH KIND OF INITIAL CONDITION WITH NON-UNIFORM GRIDS 64*192 AND SLIP BOUNDARY CONDITION.	91
FIGURE 5.35 THE NUMERICAL RESULTS OF RAYLEIGH-TAYLOR INSTABILITY ADOPTING 5 TH KIND OF INITIAL CONDITION WITH NON-UNIFORM GRIDS 64*192 AND SLIP BOUNDARY CONDITION.	92
FIGURE 5.36 EXPERIMENTAL RESULTS OF A COLLAPSING WATER COLUMN BY KOSHIZUKA [40].	95
FIGURE 5.37 THE NUMERICAL RESULTS OF COLUMN COLLAPSE WHICH THE TIME STEP SIZE IS 0.00025S AND THE SPATIAL SIZE IS 4.86E-3M (GRIDS: 120*70). THE MAXIMUM COURANT NUMBER DURING THE COMPUTATION IS 0.699.	96
FIGURE 5.38 THE NUMERICAL RESULTS OF COLUMN COLLAPSE WHICH THE TIME STEP SIZE IS 0.001S AND THE SPATIAL SIZE IS 0.0121M (GRIDS: 48*28). THE MAXIMUM COURANT NUMBER DURING THE COMPUTATION IS 0.621.	97
FIGURE 5.39 THE NUMERICAL RESULTS OF COLUMN COLLAPSE WHICH THE TIME STEP SIZE IS 0.000125S AND THE SPATIAL SIZE IS 2.43E-03M (GRIDS: 240*140). THE MAXIMUM COURANT NUMBER DURING THE COMPUTATION IS 0.563.	98
FIGURE 5.40 THE NUMERICAL RESULTS OF COLUMN COLLAPSE WHICH THE TIME STEP SIZE IS 0.00025S AND THE SPATIAL SIZE IS 4.86E-03M (GRIDS: 120*165). THE MAXIMUM COURANT NUMBER DURING THE COMPUTATION IS 0.615.	100
FIGURE 5.41 THE NUMERICAL RESULTS OF COLUMN COLLAPSE WITH SURFACE TENSION WHICH THE TIME STEP SIZE IS 0.00025S AND THE SPATIAL SIZE IS 4.86E-3M (GRIDS: 120*70). THE MAXIMUM COURANT NUMBER DURING THE COMPUTATION IS 0.699.	101
FIGURE 5.42 THE NUMERICAL RESULTS OF COLUMN COLLAPSE WITH SURFACE TENSION WHICH THE TIME STEP SIZE IS 0.001S AND THE SPATIAL SIZE IS 0.0121M (GRIDS: 48*28). THE MAXIMUM COURANT NUMBER DURING THE COMPUTATION IS 0.611.	102
FIGURE 5.43 THE NUMERICAL RESULTS OF COLUMN COLLAPSE WITH SURFACE TENSION WHICH THE TIME STEP SIZE IS 0.000125S AND THE SPATIAL SIZE IS 2.43E-03M (GRIDS: 240*140). THE MAXIMUM COURANT NUMBER DURING THE COMPUTATION IS 0.485.	103
FIGURE 5.44 THE NUMERICAL RESULTS OF COLUMN COLLAPSE WITH SURFACE TENSION WHICH THE TIME STEP SIZE IS 0.00025S AND THE SPATIAL SIZE IS 4.86E-03M (GRIDS: 120*165). THE MAXIMUM COURANT NUMBER DURING THE COMPUTATION IS 0.597.	105

FIGURE 5.45 THE POSITION OF THE LEADING EDGE VERSUS TIME.	106
FIGURE 5.46 THE HEIGHT OF THE COLLAPSING WATER COLUMN VERSUS TIME.....	106
FIGURE 5.47 EXPERIMENTAL RESULTS OF A COLLAPSING WATER COLUMN HITTING AN OBSTACLE (KOSHIZUKA [40])	108
FIGURE 5.48 THE NUMERICAL RESULTS OF COLUMN COLLAPSE WITH OBSTACLE WITHOUT SURFACE TENSION. THE UPPER BOUNDARY AT THE COMPUTATIONAL DOMAIN IS WALL.	109
FIGURE 5.49 THE NUMERICAL RESULTS OF COLUMN COLLAPSE WITH OBSTACLE WITHOUT SURFACE TENSION. THE UPPER BOUNDARY AT THE COMPUTATIONAL DOMAIN IS OPEN BOUNDARY WHICH PRESSURE IS FIXED.	110
FIGURE 5.50 THE NUMERICAL RESULTS OF COLUMN COLLAPSE WITH OBSTACLE WITH SURFACE TENSION. THE UPPER BOUNDARY AT THE COMPUTATIONAL DOMAIN IS WALL.	111
FIGURE 5.52 THE PHYSICAL MODEL OF HYDRAULIC BORE.....	113
FIGURE 5.53 SCHEMATIC REPRESENTATION OF GRID CONFIGURATION FOR THE BORE.	113
FIGURE 5.54 VELOCITY VECTORS AND FLUID CONFIGURATION FOR THE BORE CALCULATED WITH $G=1.0$ AT TIMES 3.5s, 4.9s, 8.0s, 10.0s AND 12.0s.	115
FIGURE 5.55 VELOCITY VECTORS AND FLUID CONFIGURATION WITH VELOCITY $U=1.0$ AT INLET.....	117
FIGURE 5.56 VELOCITY VECTORS AND FLUID CONFIGURATION WITH VELOCITY $U=2.0$ AT INLET.....	118
FIGURE 5.57 VELOCITY VECTORS AND FLUID CONFIGURATION WITH VELOCITY $U=3.0$ AT INLET.....	119



Nomenclature

A	Coefficient of algebraic equation
Co	Courant number
F_C	Boundary flux due to convection
F_D	Boundary flux due to diffusion
f	Face, point in the centre of the face
f_P	Weighting factor
f_σ	Surface tension force
g	Gravitational acceleration
\dot{m}_f	Mass flow rate cross face
P	Pressure
S	Source term in discretized momentum equation
S_α	Source term in discretized the indicator equation
t	Time
w_f	Weighting factor
x, y	Components of Cartesian coordinate
$\vec{\delta}_{pnb}$	Vector pointing from center of primary cell to the center of neighbor one
Γ	Diffusivity
ϕ	Property
ΔV	Volume
$\gamma(r)$	Flux limiter equation
α	Volume fraction
σ	Surface tension coefficient
ν	Kinetic viscosity

ρ	Fluid density
μ	Viscosity coefficient
Δ	Difference operator
∇	Gradient
θ_f	Angle between the normal to interface and orthogonal component of the face area vector
n	New time level
o	Old time level



Abbreviation

BD	Bounded Downwind Scheme
CBC	Convective Boundedness Criterion
CFD	Computational Fluid Dynamics
CDS	Central Difference Scheme
CICSAM	Compressive Interface Capturing Scheme for Arbitrary Meshes
CN	Crank-Nicolson
CUBISTA	Convergent and Universally Bounded Interpolation Scheme
CUS	Cubic upwind difference scheme
CV	Control Volume
DDS	Downwind Difference Scheme
HRS	High Resolution Scheme
LUS	Linear Upwind Scheme
MAC	Marker and cell
MINMOD	Minimum Modulus
MUSCL	Monotonic Upwind Scheme for Conservation Law
NVD	Normalized Variable Diagram
PISO	Pressure Implicit with Splitting of Operator
QUICK	Quadratic Upwind Interpolation for Convection Kinematics
SLIC	Simple Line Interface Calculation
SMART	Sharp and Monotonic Algorithm for Realistic Transport
STOIC	Second- and Third-Order Interpolation for Convection
TVD	Total Variation Diminishing
UDS	Upwind Difference Scheme
UQ	ULTIMATE-QUICKEST

Chapter 1 Introduction

1.1 Background

The simulation of two immiscible fluids separated by a well-defined interface has many applications. One area is the biochemical science engineering where it is used to simulate biochemical material or fluids such as blood being transported through the capillary tubing and channels in the vascular system or in Micro Electro Mechanical Systems (MEMS) devices. In the environmental engineering, free surface flows are used in the simulation of motion of water in the marine environment, volcanic flows and plumes, and Dam and dyke breaks. On the other hand, to shorten the design of the digital inkjet printing technology, numerical simulations seem to be the require tool. Yeh [1] used a simple but versatile finite element method for the simulation of piezoelectric inkjet. Liou et al. [2] simulated the SEAjet (Static-Electricity Actuator inkJET) [3] by finite volume method. This technology has significant influences on other relevant applications, such as IC package process and LED screens, etc.

1.2 Related Studies

The computation of flows with free surfaces is difficult in the prediction of the shape and the position of the interface between two immiscible fluids. Hirt and Nichols [4] illustrated that three types of problems arise in the numerical treatment of free surfaces: (1) their discrete representation, (2) their evolution in time, and (3) the manner in which boundary conditions are imposed. Therefore, it is important to develop robust methods to capture interfaces. Such methods in finite volume approach can be classified into two typical categories: surface methods and volume methods [5]. In the following, these methods are briefly reviewed.

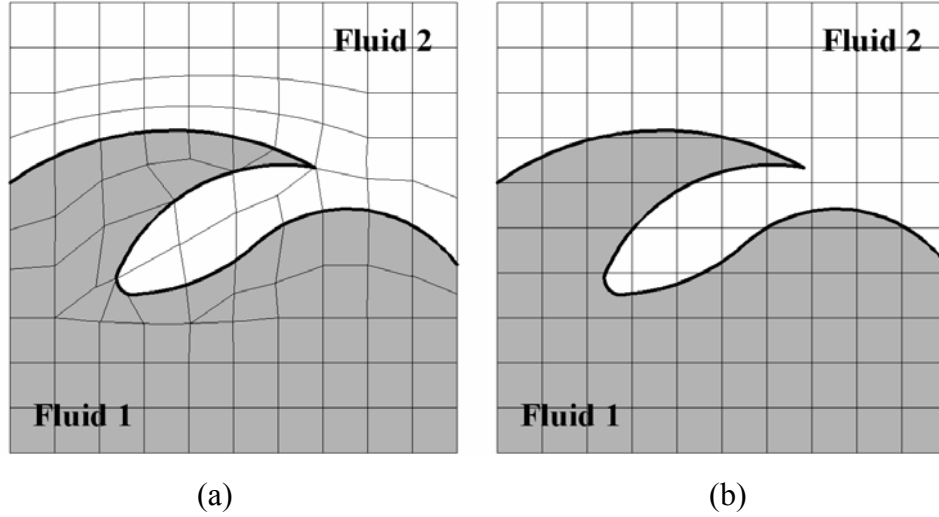


Figure 1.1 (a) surface methods (b) volume methods

Surface methods, which are called interface-tracking method, mark and track the interface with calculation only on one phase based on the satisfaction of two conditions. First, the free surface is a sharp interface between the two fluids and there is no flow across the interface. Second, forces acting on the interface are in equilibrium. These methods only compute the liquid flow and the computational grids vary with the shape and position of the free surface. The differences between surface methods and volume methods can be shown as Figure 1.1. By surface methods the grid fits the interface and moves with it. The free surface is treated as a boundary of the computation domain. The advantage of this approach is that the interface remains sharp as it is across the mesh and the surface tension force is included in the subsequent implement without be copied specially. On the other hand, interface-tracking or moving meshes methods can not be used if the interface changes significantly. There are several interface-tracking (surface) methods which mark and track the interface explicitly, (i) with a set of marker particles or line segments on interface [6], or (ii) height functions [7], (iii) level set method [8], and (iv) surface fitted methods. [5]

In volume methods, the different fluids are marked either by massless particles or by an indicator function which may turn to be volume fraction. The advantage of these methods is their ability to cope with the arbitrary shaped interface and large deformation. One of the main difficulties associated with these methods is the advection of the interface without diffusing, dispersing, or wrinkling it.

The earliest numerical technique designed for simulating free surface flows was the well-known marker and cell (MAC) method [9]. The MAC method uses massless marker particles which spread over the volume occupied by a fluid with a free surface (see Figure 1.2). A cell with no marker particles is considered to be empty. This method can treat complex phenomena like wave breaking. Although the MAC method can tackle arbitrary unstructured grids, there are two problems that arise in further simulation. First, the disadvantage of this method is that the computer storage will increase significantly and time consuming is largely increased in three-dimensional calculations. The other is that it is also difficult to obtain quantitative information on interface orientation. However, some improved versions have been presented, for example by Chen et al. [10]

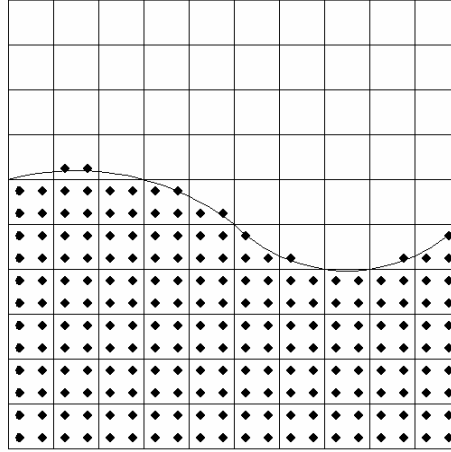


Figure 1.2 Schematic representation of marker and cell mesh layout.

Several volume tracking methods for finite volume and arbitrary meshes have been developed with the aim of maintaining sharp interfaces. The better known methods are Simple Line Interface Calculation (SLIC) method [11], the volume-of-fluid (VOF) method [5] and the method of Youngs [12].

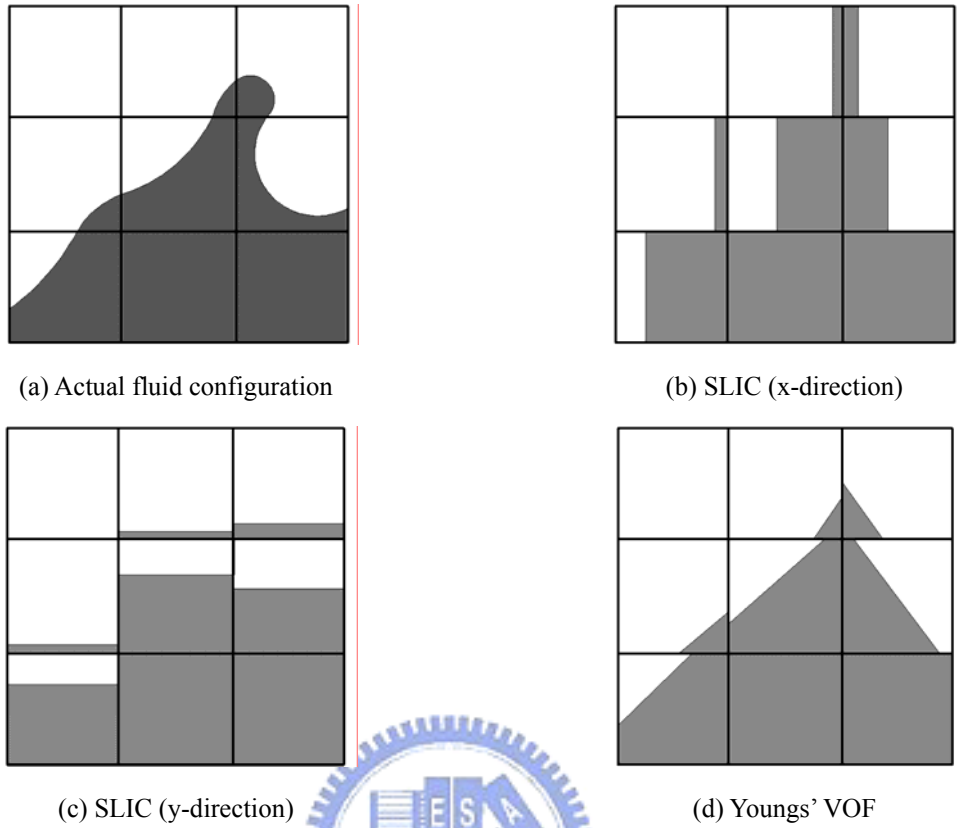


Figure 1.3 Interface reconstructions of (a) actual fluid configuration, (b) SLIC in x-direction, (c) SLIC in y-direction (d) Youngs' VOF.

The SLIC method [11] approximates interfaces as piecewise constant, where interfaces within each cell are reconstructed using straight lines parallel to one of the coordinate directions. It is a direction-split algorithm and during each direction sweep, only cell neighbors in the sweep direction are used to determine the interface reconstruction. (Figure 1.3(b) and 1.3(c)). An extensive review of this type of methods can be found in [13].

Youngs' VOF (Y-VOF) [12] method uses a more accurate interface reconstruction than the SLIC method. Youngs give a useful refinement to the SLIC method with the use of oblique lines to approximate the interface in the cell (Figure 1.3(d)). Unlike the SLIC method, the neighbor cells are used to approximate the slope of the interface in Youngs' VOF. The SLIC method and Youngs' VOF can be classified as line technique and these methods use structured grids and are therefore restricted to such mesh topologies.

The VOF method uses donor-acceptor approximation and is one of the most effective

volume tracking methods in the simulation and prediction of two-fluid system with interfaces where density and viscosity change abruptly. The VOF method became popular in the 80s though the development of this method occurred earlier [9,14]. Its appealing feature is its volume fluxes can be formulated algebraically without reconstructing the interface. The interfaces are represented by the value of the VOF function which is a volume fraction of one of the fluids. Another benefit of using volume fractions is that only a scalar convection equation, which is called indicator equation, need to be solved to propagate the volume fractions through the computational domain. In the calculation of convective fluxes, two of the main errors in numerical modeling of convection-diffusion transport problems are numerical diffusion and numerical dispersion. Numerical diffusion causes smearing of predicted profile, and numerical dispersion results in non-physical phenomenon such as oscillation or over/under shoots produced in the solution.

Because the first-order upwind scheme is too diffusive, differencing schemes of order higher than unity are therefore required. Second-order accuracy can be achieved by linear interpolation from two upwind values, yield so-called linear upwind schemes (LUDS) of Shyy et al. [15]. Third-order accuracy is achieved by a quadratic line through those two upwind values and one downwind, the QUICK scheme of Leonard [16]. These schemes get more accurate results than first-order upwind, but they are not bounded which may give rise to oscillations in the region where there are strong gradients of the variable being solved. There are two major categories to handle these numerical dispersion problems, known as flux-blending and composite flux-limiter methods. The flux-blending method can be divided into two classes. The first class is added an anti-diffusion flux to a first order upwind scheme, for example, Zalesak presented the flux corrected transport (FCT) method [17]. In the second class, a smoothing diffusive flux is introduced into an unbounded higher order schemes. In generally speaking, due to the nature of flux-blending method, the numerical dispersion can be reduced but it will be very expansive computationally and the optimal blending factor can not be obtained easily.

Rudman used the flux corrected transport (FCT) method and developed the FCT-VOF

[18] to enhance the accuracy of simulation. The first order upwind is diffusive and stable. The first order downwind is unstable, but has the advantage of maintain sharp interface. If a suitable combination of upwind and downwind fluxes can be formulated, a volume tracking algorithm can be designed. Hence, this method combines the low order scheme and higher order scheme. Although the FCT-VOF method is non-diffusive in nature, but create unphysical flotsam and jetsam.

As everyone knows, only the first order upwind difference scheme satisfies the sufficient condition of the Convective Boundedness Criteria (CBC) [23]. In order to fit in with the CBC, a higher order difference scheme has to be a non-linear combined framework. In the composite flux-limiter method, the numerical flux at a consider face is adjusted by the flux-limiter function. Normalized Variable (NV) and Normalized Variable Diagram (NVD) which presented by Leonard [19] are important implements for the composite flux-limiter method and simplify the connection between high accuracy and bounedness in high resolution schemes (HRs) [20].

At first, the flux limiter function is presented by Van Leer [21]. Sweby [22] developed the Total Variation Diminishing (TVD) approach for high resolution schemes. Flux limiter functions were introduced to guarantee that values of a conserved property remain within the bounds. The accurate simulation of convection continues to attract many workers due to the many challenges it still offers. The difficulty in devising an effective scheme lies in the conflicting requirements of accuracy, stability and boundedness. There are many high resolution schemes developed in these years, such as SMART of Gaskell and Lau [23], GAMMA of Jasak [24], SUPERBEE of Roe [25], STOIC of Darwish [26], MUSCL and Van Leer of Van Leer [27]

Numerical diffusion, a significant source of error in numerical solution of conservation equations, can be separated into two components, namely cross-stream and stream-wise numerical diffusions. The former, the cross-stream numerical diffusion, occurs in a multi-dimensional flow when the flow direction is perpendicular to the grid lines. The latter, the stream-wise numerical diffusion, happens when the flow direction is parallel to the grid

lines.

In addressing aforementioned issue, many researchers try to improve the accuracy by reducing streamwise and cross-stream numerical diffusion. Hence, the blending strategy that depends on the angle between the flow direction and the grid lines was developed. The best approach is to have a continuous switching function whereby the values of compressive and high resolution schemes are blended together with a blending factor. This general approach has been followed in the derivation of composite schemes and is utilized in the HRIC of Muzaferija [28], STACS of Darwish [29] and CICSAM of Ubbink [30].

1.3 Present study of this thesis

The aim of this study is to develop a robust scheme which is accurate, stable and easy to be implemented on arbitrary unstructured grids. The two-fluid system will be modeled by the volume tracking method. This research is considered to be two-dimensional under unsteady and incompressible conditions with body forces of gravity and surface tension.

In Chapter 2, the conception of conservation laws which are used to construct the governing equations is introduced. The governing equations in two-fluid system are given and the mathematical model of the surface tension term in the momentum equation will be made.

Chapter 3 introduces the numerical method and discretization of the VOF equation. The blending strategy was developed and used in constructing volume tracking approach is described. This is followed by a discussion of the general strategy used for switching between compressive and high resolution schemes.

In Chapter 4, a conservative finite volume discretization scheme is used for the discretization of the velocity field. Then the PISO algorithm of Issa [31] will be introduced to solve the unsteady flow field.

Chapter 5 presents the cases studied and the calculated results. The efficiency of difference schemes will be compared. At first, different high resolution schemes are demonstrated and compared. Then, the different combinations of compressive and high resolution schemes with blending strategy are compared to the well-known HRIC, CICSAM and STACS schemes. The best combination of different differencing schemes will be adopted

in the following cases. Some realistic cases will be simulated, such as column collapse, sloshing and hydraulic bore. Then, these cases will be compared with analytical solution or experiment results.

The main conclusions and discussion of this thesis are given in Chapter 6.



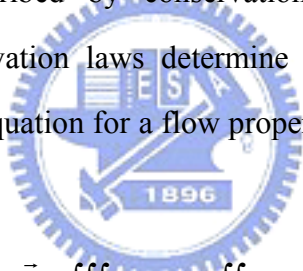
Chapter 2 Mathematical Model

2.1 Introduction

The subject of this chapter is the development of CFD methodology for the flow of two immiscible fluids. Volume tracking methods, describing the flow of the two immiscible fluids by a well defined interface, are introduced to solve two-fluids flow field. In the mathematical model of two-fluid system, the different fluids are modeled as a single continuum with a jump in the fluid properties at the interface. The different value of volume fraction which undergoes a step change will mark the fluids and influence fluid properties, such as viscosity and density. Moreover, surface tension force is important to two-fluid flow field and will go into details in this chapter.

2.2 General transport equation

The fluid flow is described by conservation of mass, momentum and energy mathematically. These conservation laws determine the physical behavior of fluids. The general form of conservation equation for a flow property ϕ to the control volume shown in Figure 2.1, is


$$\frac{\partial}{\partial t} \iiint_{\forall} \phi d\forall + \iint_S F_C \cdot d\vec{S} = \iint_S F_D \cdot d\vec{S} + \iiint_{\forall} Q_v d\forall + \iint_S Q_s \cdot d\vec{S} \quad (2.1)$$

where t is the time, $F_C = \vec{V}\phi$ is the flux over the boundary due to convection, \vec{V} is the fluid velocity, F_D is the flux over the boundary due to diffusion, Q_v is the internal source, Q_s is the source at the boundary, \forall is the control volume and S is the control surface.

Guess's theorem can be applied to equation (2.1):

$$\frac{\partial}{\partial t} \iiint_{\forall} \phi d\forall + \iiint_{\forall} \nabla \cdot F_C d\forall = \iiint_{\forall} \nabla \cdot F_D d\forall + \iiint_{\forall} Q_v d\forall + \iiint_{\forall} \nabla \cdot Q_s d\forall \quad (2.2)$$

The above equation can be reduced to the general conservative differential form when the control volume is contracted to a single point:

$$\frac{\partial \phi}{\partial t} + \nabla \cdot F_C = \nabla \cdot F_D + Q_v + \nabla \cdot Q_s \quad (2.3)$$

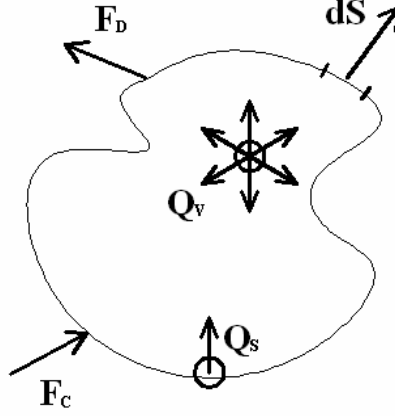


Figure 2.1 General form of the conservation law

2.3 Governing equations

Mass conservation

The transport equation of mass conservation is derived by substituting $\phi = \rho$ with the assumption of no sources as:

$$\frac{\partial \rho}{\partial t} + \nabla \cdot (\rho \vec{V}) = 0 \quad (2.4)$$

Momentum conservation

The transport equation for the conservation of momentum is derived by substituting ϕ by $\rho \vec{V}$. In this study, it is considered to be two-dimensional with the assumption of a laminar Newtonian working fluid under unsteady and incompressible conditions with body force and surface tension force. The momentum equation is

$$\frac{\partial \rho \vec{V}}{\partial t} + \nabla \cdot (\rho \vec{V} \vec{V}) = -\nabla p + -\nabla \cdot (\Gamma \nabla \vec{V}) + \rho g + f_\sigma \quad (2.5)$$

where ρ is the fluid density, \vec{V} is the velocity, p is the pressure, Γ is the diffusion coefficient, g is the gravitational acceleration coefficient which the only external force acting on the fluid and f_σ is the surface tension force.

The VOF equation

As mentioned in first chapter, different fluids are marked by volume fraction in volume tracking methods (see Figure 2.2).

$$\alpha = \frac{\text{Volume of fluid 1}}{\text{Total Volume of Control Volume}} \quad (2.6)$$

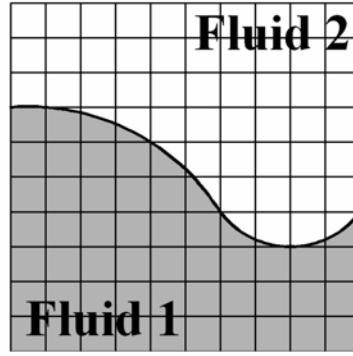


Figure 2.2 Fluids are marked with indicator function

From above equation (2.6), α is the volume fraction defined as

$$\alpha = \begin{cases} 1 & \text{for the cell filled with fluid 1} \\ 0 & \text{for the cell filled with fluid 2} \\ 0 < \alpha < 1 & \text{for the cell at the transitional area} \end{cases} \quad (2.7)$$

Considering the value of the volume fraction, all properties of the effective fluid will be calculated as

$$\rho = \rho_1 \alpha + \rho_2 (1 - \alpha) \quad (2.8)$$

$$\mu = \mu_1 \alpha + \mu_2 (1 - \alpha) \quad (2.9)$$

where the subscripts 1 and 2 denote fluid 1 and fluid 2. The above definition of α implies that it is a step function and the density defined by equation (2.8) is piecewise continuous.

The two-fluid system is propagated as the Lagrangian invariant and thus has a zero material derivative:

$$\frac{D\alpha}{Dt} = \frac{\partial \alpha}{\partial t} + \vec{V} \cdot \nabla \alpha = 0 \quad (2.10)$$

The continuity equation (2.4) can be reformulated as a so-called non-conservative form by substituting equation (2.8) as:

$$\begin{aligned} \frac{\partial \rho}{\partial t} + \nabla \cdot \rho \vec{V} &= 0 \\ \Rightarrow \frac{\partial \rho}{\partial t} + \vec{V} \cdot \nabla \rho + \rho \nabla \cdot \vec{V} &= 0 \\ \Rightarrow \nabla \cdot \vec{V} &= \frac{-1}{\rho} \left(\frac{\partial \rho}{\partial t} + \vec{V} \cdot \nabla \rho \right) = \frac{-1}{\rho} \left(\frac{D\rho}{Dt} \right) \\ &= \frac{-1}{\rho} \frac{D}{Dt} [\alpha(\rho_1 - \rho_2) + \rho_2] \end{aligned}$$

$$= \frac{\rho_2 - \rho_1}{\rho} \left(\frac{D\alpha}{Dt} \right) \quad (2.11)$$

By substituting equation (2.10) into the above equation the continuity equation becomes

$$\nabla \cdot \vec{V} = 0 \quad (2.12)$$

For two-fluid systems with high density ratios of the fluids it is much suitable for numerical solution, because \vec{V} is by definition continuous at the interface. Figure 2.3 shows two fluids with different density in a close domain. The velocity \vec{V} of the fluid of entering and leaving the domain is the same, but the momentum $\rho\vec{V}$ of the fluid entering and leaving the domain is different.

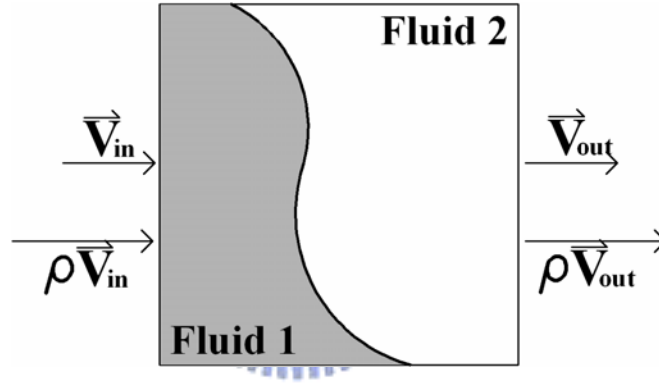


Figure 2.3 Continuity of the velocity field and discontinuity of the momentum

The equation (2.10) can be rearranged into a conservation form with the incompressible condition by recognizing that $\nabla \cdot \alpha \vec{V} = \alpha \cdot \nabla \vec{V} + \vec{V} \cdot \nabla \alpha$ and the equation (2.12) as:

$$\frac{\partial \alpha}{\partial t} + \nabla \cdot \alpha \vec{V} = 0 \quad (2.13)$$

2.4 Surface tension

Surface tension force is considered as an important part in this thesis and will be discussed in many cases in Chapter 5. Brackbill [32] presented a numerical model for the simulation of surface tension. Surface tension always creates a pressure jump at interface between two fluids. The surface tension coefficient σ exists for any pair of fluids and its magnitude is determined by the nature of fluids. For immiscible fluids, the value of σ is

always positive and for miscible fluids, it is negative [33]. Laplace and Young (1805) (see Adamson [34]) show the magnitude of this pressure jump is a function of mean interface curvature.

$$\Delta P = P_i - P_o = \sigma \kappa \quad (2.14)$$

where P_i is the pressure on the concave side of the curved surface, P_o is the pressure on the convex side, σ the surface tension coefficient and κ the mean interface curvature that for $\kappa > 0$ fluid 1 lies on the concave side of the interface and for $\kappa < 0$ it is fluid 2 lies on the concave side (Figure 2.4).

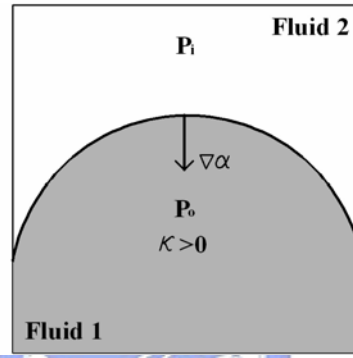


Figure 2.4 Fluid arrangement and the sign of the curvature

The gradient of α which is zero everywhere except at transient area gives the normal vector, which always points from fluid 2 toward fluid 1:

$$\vec{n} = \nabla \alpha \quad (2.15)$$

Thus, the mean interface curvature κ can be rewritten in terms of divergence of the unit normal vector as:

$$\kappa = -\nabla \cdot \left(\frac{\vec{n}}{|\vec{n}|} \right) = -\nabla \cdot \left(\frac{\nabla \alpha}{|\nabla \alpha|} \right) \quad (2.16)$$

Therefore, the surface tension term in the momentum equation can be reformulated by substituting equation (2.13) into equation (2.15):

$$f_\sigma = \nabla P = \Delta P \vec{n} = \sigma \kappa \nabla \alpha = -\sigma \nabla \cdot \left(\frac{\nabla \alpha}{|\nabla \alpha|} \right) \nabla \alpha \quad (2.17)$$

2.5 Boundary Conditions

Inlet: Velocity at inlet is specified.

Outlet: Boundary condition at outlet uses open boundary condition by which the pressure is specified. The distribution of volume fraction is designated in the initial stage. The boundary values are obtained from convective boundary condition [35]

$$\frac{\partial \phi}{\partial t} + \vec{V}_c \cdot \nabla \phi = 0 \quad (2.18)$$

where ϕ represent the transported property and \vec{V}_c is the convective velocity.

Rigid boundary (walls): There are two types boundary conditions applied at walls. The first is the non-slip boundary condition ($u=0, v=0$) for viscous flow. The second is suitable for inviscid flow and slip boundary condition is applied, by which only the normal velocity vanishes at the wall.

2.6 Closure

A mathematical model for the prediction of two-fluid flow has been presented in this chapter. This model simulates the time dependent, incompressible, viscous, two-dimensional two- fluid system which influence by surface tension and gravity. All the differential equations in a conservation form are ready to be discretised in finite volume method in the next chapter.

Chapter 3 Numerical Method for the VOF Equation

3.1 Introduction

For the volume tracking methods, the VOF equation which is the so-called indicator equation, dominates the two-fluid flow field. Thus, this chapter deals with the derivation of differencing schemes which can prevent the smearing of a step profile by removing numerical diffusion, and uses the finite volume method to discretize the VOF equation. To enhance the efficiency and accuracy, the blending strategy will be introduced. The composite schemes which obey the blending strategy will be reviewed, such as the HRIC scheme of Muzaferija [28], STACS scheme of Darwish [29] and CICSAM scheme of Ubbink [30].

3.2 The approximation for the face value of α

The distribution of volume fraction is governed by the equation (2.13):

$$\frac{\partial \alpha}{\partial t} + \nabla \cdot \alpha \vec{V} = 0 \quad (2.13)$$

in which the first term on the left-hand-side is an unsteady term and the second term on the left-hand-side is the convection term. The computation of convective fluxes is a complex topic and there are many former researchers devoted to this issue. In the following contents, a simple and efficient treatment will be deduced.

The face value α_f can be estimated as a function of neighbor cells. Figure 3.1 shows a control volume and its neighbor cells which determined by flow direction on the control surface. The subscripts U, D and A denote upwind cell, donor cell and acceptor cell.

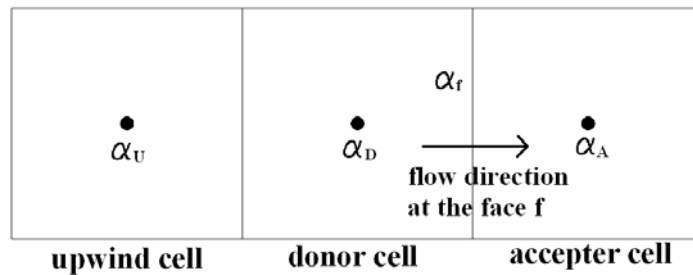


Figure 3.1 the relationship of a control volume and its neighbor cells

For the unstructured grid calculations, only two neighboring cell values can be obtained

directly for a consider face. To discretize the VOF equation, as will be seen in section 3.5, the value of α at each cell face need to be estimated by some approximations and then the value of upwind cell α_U will be obtained. The most convenient way to estimate the face value α_f is either the upwind difference scheme or the central difference scheme. These two schemes can be combined as:

$$\begin{aligned}\alpha_f &= \alpha^{UD} + \gamma(\alpha^{CD} - \alpha^{UD}) \\ &= \alpha^D + \gamma\left(\frac{\alpha^A + \alpha^D}{2} - \alpha^D\right) \\ \Rightarrow \alpha_f &= \alpha_D + \gamma\left(\frac{\alpha_A - \alpha_D}{2}\right)\end{aligned}\tag{3.1}$$

The second term of the right-hand-side stands for an anti-diffusion correction to the upwind differencing. This approximation becomes central differencing for $\gamma = 1$, which may cause oscillations in the region of large gradients. To ensure boundedness of solution γ must be limited. The families of schemes based on the Total Variation Diminishing (TVD) [16] flux limiters are examples of this approach. Furthermore, these schemes are implemented in the context of the normalized variables formulation (NVF) which is proposed by Leonard [16] for the development of normalized variables diagram (NVD) schemes originally. Sweby [22] presented the limiter γ as a function of the ratio of two consecutive gradients r :

$$r = \frac{\alpha_D - \alpha_U}{\alpha_A - \alpha_D}\tag{3.2}$$

The volume fraction value can be normalized as:

$$\tilde{\alpha} = \frac{\alpha - \alpha_U}{\alpha_A - \alpha_U}\tag{3.3}$$

The normalized variable can be used to give expressions for $\tilde{\alpha}_D$ and $\tilde{\alpha}_f$:

$$\tilde{\alpha}_D = \frac{\alpha_D - \alpha_U}{\alpha_A - \alpha_U}\tag{3.4}$$

$$\tilde{\alpha}_f = \frac{\alpha_f - \alpha_U}{\alpha_A - \alpha_U} \quad (3.5)$$

With the normalization $\tilde{\alpha}_U = 0$ and $\tilde{\alpha}_A = 1$.

Introducing normalized variables into equation (3.1) leads to

$$\tilde{\alpha}_f = \tilde{\alpha}_D + \gamma(r) \left(\frac{1 - \tilde{\alpha}_D}{2} \right) \quad (3.6)$$

where

$$r = \frac{\tilde{\alpha}_D}{1 - \tilde{\alpha}_D} \quad (3.7)$$

It is seen from the above equation, $\tilde{\alpha}_f$ is simply a function of $\tilde{\alpha}_D$.

3.3 Linear difference schemes

Figure 3.2 shows the Normalized Variable Diagram (NVD) for a number of linear difference schemes. In the Figure the normalized face value is plotted as a linear function of the normalized donor cell value.

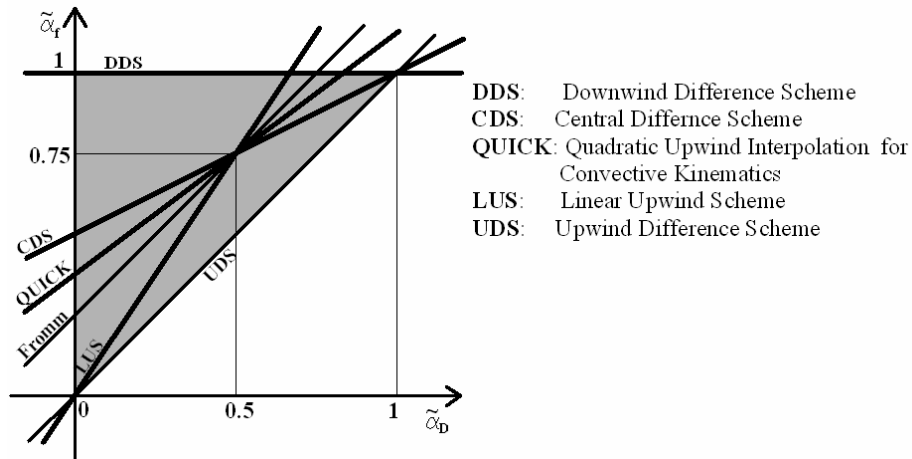


Figure 3.2 Normalized Variable Diagram (NVD).

UDS (Upwind Difference Scheme) is unconditionally stable and always produces a bounded solution, but has high numerical diffusion and loses accuracy. DDS (Downwind Difference Scheme) is a first-order scheme that introduces negative numerical diffusion. CDS (Central Difference Scheme), LUS (Linear Upwind Scheme), Fromm's scheme and QUICK (Quadratic Upwind Interpolation for Convective Kinematics) scheme are second-order

accuracy schemes. The shortcomings of high order schemes are the causes of solution oscillations in sharp gradient regions. In the above diagram, the line of high order schemes would pass the point (0.5, 0.75). As given in equation (3.6), the different scheme at face $\tilde{\alpha}_f$ can be written as the combination of the UDS and an anti-diffusive term. Different schemes can be represented by specifying a specific flux limiter γ which is a function of the gradient ratio r . A list of the linear difference schemes is given in the following table. Their relationships are also plotted in Figure 3.3.

	NVD	Flux limiter function
UDS	$\tilde{\alpha}_f = \tilde{\alpha}_D$	$\gamma(r) = 0$
DDS	$\tilde{\alpha}_f = 1$	$\gamma(r) = 2$
CDS	$\tilde{\phi}_f = \frac{1}{2}(1 + \tilde{\alpha}_D)$	$\gamma(r) = 1$
QUICK	$\tilde{\alpha}_f = \frac{3}{4}\tilde{\alpha}_D + \frac{3}{8}$	$\gamma(r) = \frac{1}{4}r + \frac{3}{4}$
CUS	$\tilde{\alpha}_f = \frac{5}{6}\tilde{\alpha}_D + \frac{1}{3}$	$\gamma(r) = \frac{1}{3}r + \frac{2}{3}$
Fromm	$\tilde{\alpha}_f = \tilde{\alpha}_D + \frac{1}{4}$	$\gamma(r) = \frac{1}{2}(r + 1)$
LUS	$\tilde{\alpha}_f = \frac{3}{2}\tilde{\alpha}_D$	$\gamma(r) = r$

Table 3.1 The normalized variable (NV) and flux limiter function of linear schemes.

Similarly, linear difference schemes can be plotted in TVD diagram (see Figure 3.3).

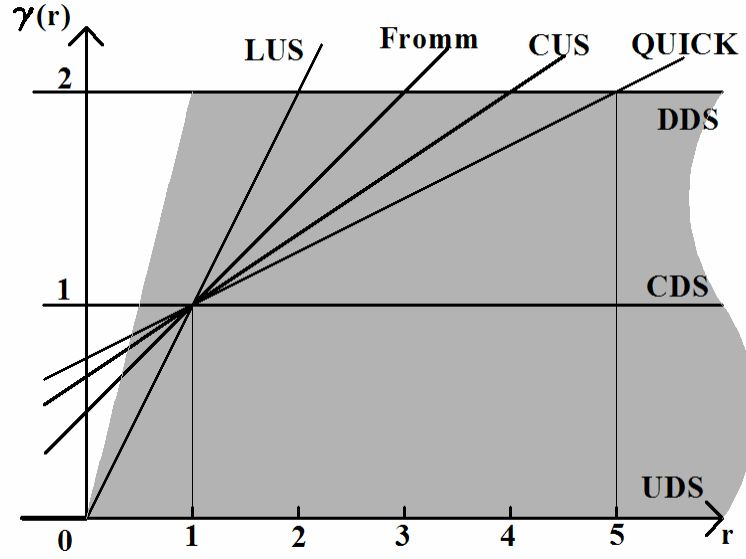


Figure 3.3 Relationship between γ and r for linear difference schemes.

3.4 Non-linear difference schemes

There are many high-order linear approaches introduced in section 3.1. However these the high-order schemes do not satisfied the Convective Boundedness Criterion (CBC) which was proposed by Gaskell and Lau [23]. The boundedness criterion of CBC can be shown in the NVD (see the shadow area of Figure (3.2)) :

$$\begin{cases} \tilde{\alpha}_f = \tilde{\alpha}_D & \text{for } \tilde{\alpha}_D < 0 \text{ or } \tilde{\alpha}_D > 1 \\ \tilde{\alpha}_D \leq \tilde{\alpha}_f \leq 1 & \text{for } 0 \leq \tilde{\alpha}_D \leq 1 \end{cases} \quad (3.8)$$

To satisfy the CBC, a high-order scheme has to be a non-linear framework. Hence, high resolution schemes (HRS) [20] are developed for solving this problem which have the following properties: (i) solutions are free from oscillations or wiggles, (ii) high accuracy is obtained around shocks and discontinuities and (iii) CBC is satisfied. Non-linear approaches get a flux-limiter function to ensure a bounded value. The schemes of SMART and STOIC are classified as NVD category.

Sweby [22] has shown that the following constraint on the limiter guarantees that the scheme satisfies the TVD condition.

$$0 \leq \left(\frac{\gamma_f(r)}{r}, \gamma_f(r) \right) \leq 2 \quad (3.9)$$

Figure 3.4 shows TVD constraints in NVD and TVD diagram. The hatched region is known as the second-order regime. Therefore, high resolution schemes which pass through the

shadow area of Figure 3.2 satisfy CBC, but not fit in TVD constraints completely. It is apparent that the TVD schemes are more constrained than the NVD schemes. The MUSCL, SUPERBEE, OSHER and Van Leer schemes are developed based on the TVD theory.

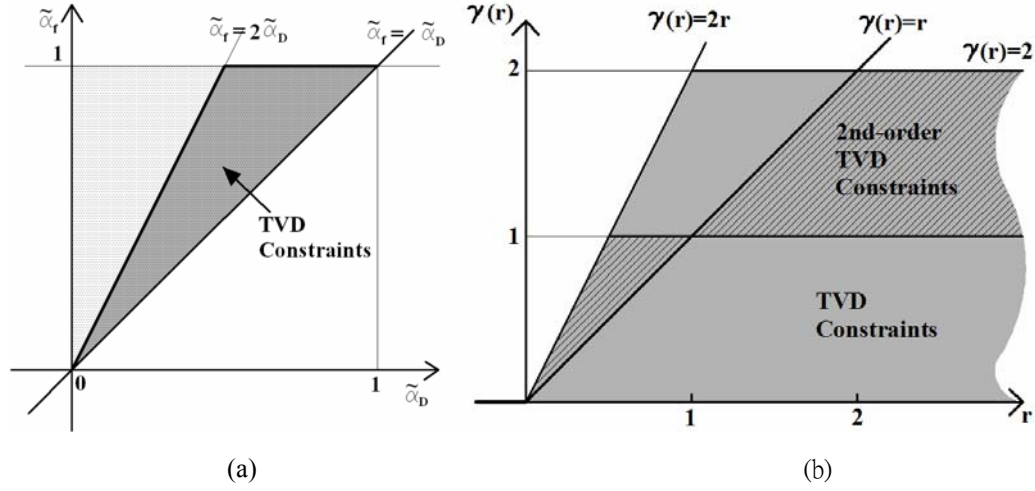


Figure 3.4 TVD Constraints in (a) NVD and (b) TVD diagram.

The following table lists the NVD equation and flux limiter equation in TVD of non-linear high resolution schemes.

	NVD	Flux limiter equation
SMART	$\tilde{\alpha}_D \geq 1 \text{ or } \tilde{\alpha}_D \leq 0, \tilde{\alpha}_f = \tilde{\alpha}_D$ $\frac{1}{6} \geq \tilde{\alpha}_D > 0, \quad \tilde{\alpha}_f = 3\tilde{\alpha}_D$ $\frac{5}{6} \geq \tilde{\alpha}_D > \frac{1}{6}, \quad \tilde{\alpha}_f = \frac{3}{4}\tilde{\alpha}_D + \frac{3}{8}$ $1 > \tilde{\alpha}_D > \frac{5}{6}, \quad \tilde{\alpha}_f = 1$	$\gamma(r) = \max\{0, \min(2, \frac{1}{4}r + \frac{3}{4}, 4r)\}$
MUSCL	$\tilde{\alpha}_D \geq 1 \text{ or } \tilde{\alpha}_D \leq 0, \tilde{\alpha}_f = \tilde{\alpha}_D$ $\frac{1}{4} \geq \tilde{\alpha}_D > 0, \quad \tilde{\alpha}_f = 2\tilde{\alpha}_D$ $\frac{3}{4} \geq \tilde{\alpha}_D > \frac{1}{4}, \quad \tilde{\alpha}_f = \tilde{\alpha}_D + \frac{1}{4}$ $1 > \tilde{\alpha}_D > \frac{3}{4}, \quad \tilde{\alpha}_f = 1$	$\gamma(r) = \max\{0, \min(2, \frac{1}{2}r + \frac{1}{2}, 2r)\}$

SUPERBEE	$\tilde{\alpha}_D \geq 1 \text{ or } \tilde{\alpha}_D \leq 0, \tilde{\alpha}_f = \tilde{\alpha}_D$ $\frac{1}{3} \geq \tilde{\alpha}_D > 0, \quad \tilde{\alpha}_f = 2\tilde{\alpha}_D$ $\frac{1}{2} \geq \tilde{\alpha}_D > \frac{1}{3}, \quad \tilde{\alpha}_f = \frac{1}{2}(\tilde{\alpha}_D + 1)$ $\frac{2}{3} \geq \tilde{\alpha}_D > \frac{1}{2}, \quad \tilde{\alpha}_f = \frac{3}{2}\tilde{\alpha}_D$ $1 > \tilde{\alpha}_D > \frac{2}{3}, \quad \tilde{\alpha}_f = 1$	$\gamma(r) = \max\{0, \min(r, 2), \min(2r, 1)\}$
STOIC	$\tilde{\alpha}_D \geq 1 \text{ or } \tilde{\alpha}_D \leq 0, \tilde{\alpha}_f = \tilde{\alpha}_D$ $\frac{1}{5} \geq \tilde{\alpha}_D > 0, \quad \tilde{\alpha}_f = 3\tilde{\alpha}_D$ $\frac{1}{2} \geq \tilde{\alpha}_D > \frac{1}{5}, \quad \tilde{\alpha}_f = \frac{1}{2}(\tilde{\alpha}_D + 1)$ $\frac{5}{6} \geq \tilde{\alpha}_D > \frac{1}{2}, \quad \tilde{\alpha}_f = \frac{3}{4}\tilde{\alpha}_D + \frac{3}{8}$ $1 > \tilde{\alpha}_D > \frac{5}{6}, \quad \tilde{\alpha}_f = 1$	$\gamma(r) = \max\{0, \min[2, 4r, \max(1, \frac{1}{4}r + \frac{3}{4})]\}$
OSHER	$\tilde{\alpha}_D \geq 1 \text{ or } \tilde{\alpha}_D \leq 0, \tilde{\alpha}_f = \tilde{\alpha}_D$ $\frac{2}{3} \geq \tilde{\alpha}_D > 0, \quad \tilde{\alpha}_f = \frac{3}{2}\tilde{\alpha}_D$ $1 > \tilde{\alpha}_D > \frac{2}{3}, \quad \tilde{\alpha}_f = 1$	$\gamma(r) = \max\{0, \min(r, 2)\}$
BDS	$\tilde{\alpha}_D \geq 1 \text{ or } \tilde{\alpha}_D \leq 0, \tilde{\alpha}_f = \tilde{\alpha}_D$ $\frac{1}{2} \geq \tilde{\alpha}_D > 0, \quad \tilde{\alpha}_f = 2\tilde{\alpha}_D$ $1 > \tilde{\alpha}_D > \frac{1}{2}, \quad \tilde{\alpha}_f = 1$	$\gamma(r) = \max\{0, \min(2r, 2)\}$
Van Leer	$\tilde{\alpha}_D \geq 1 \text{ or } \tilde{\alpha}_D \leq 0, \tilde{\alpha}_f = \tilde{\alpha}_D$ $1 > \tilde{\alpha}_D > 0, \quad \tilde{\alpha}_f = 2\tilde{\alpha}_D - \tilde{\alpha}_D^2$	$\gamma(r) = \frac{r + r }{r + 1}$
CHARM	$\tilde{\alpha}_D \geq 1 \text{ or } \tilde{\alpha}_D \leq 0, \tilde{\alpha}_f = \tilde{\alpha}_D$ $1 \geq \tilde{\alpha}_D > 0,$ $\tilde{\alpha}_f = \tilde{\alpha}_D(\tilde{\alpha}_D^2 - 2.5\tilde{\alpha}_D + 2.5)$	$\gamma(r) = \frac{r(r+3)}{(r+1)^2}, \quad r > 0$ $\gamma(r) = 0, \quad r \leq 0$

Table 3.2 The NVD equation and flux limiter function of non-linear difference schemes.

Figure 3.5 to 3.11 show the NVD and TVD diagrams of a number of high resolution schemes.

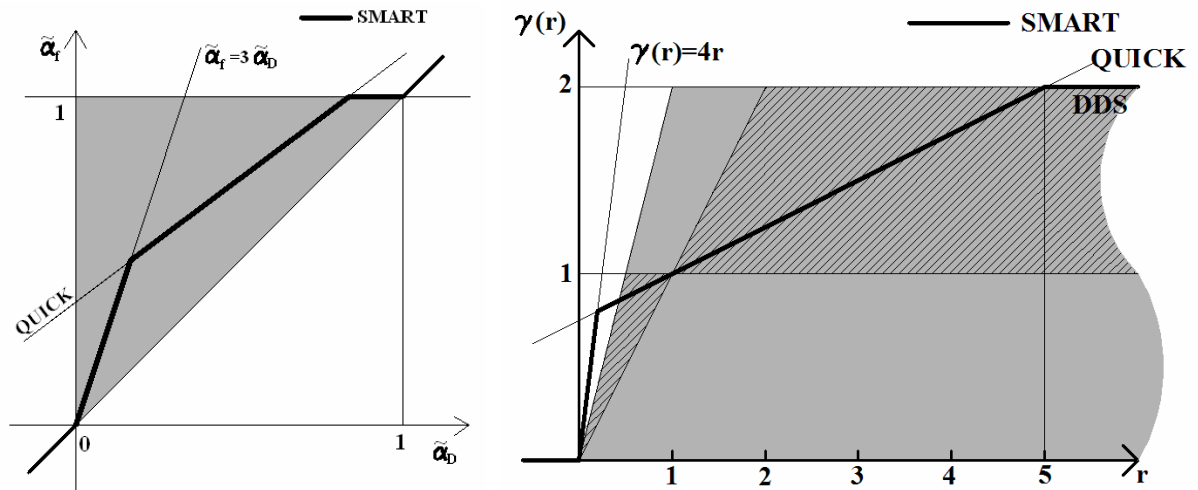


Figure 3.5 SMART

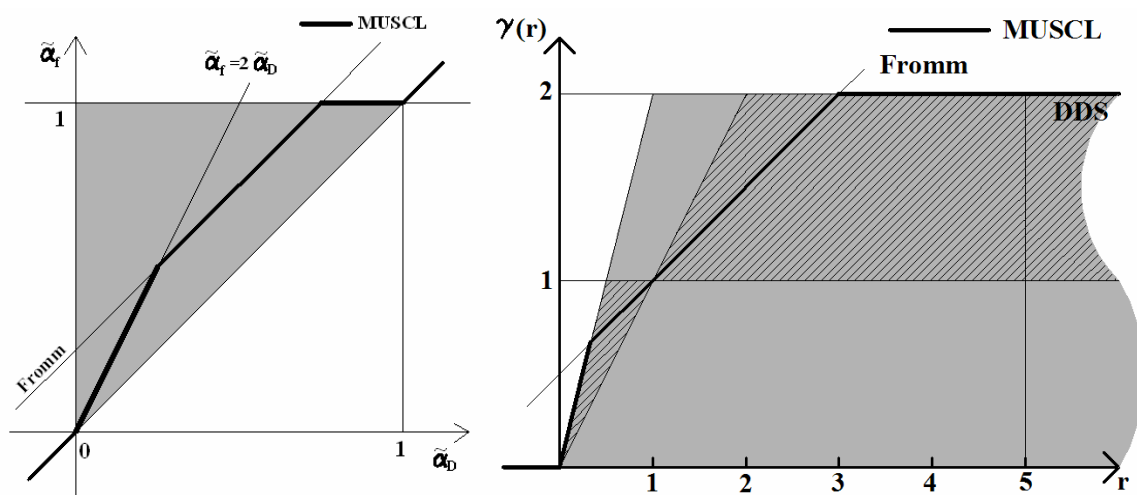


Figure 3.6 MUSCL

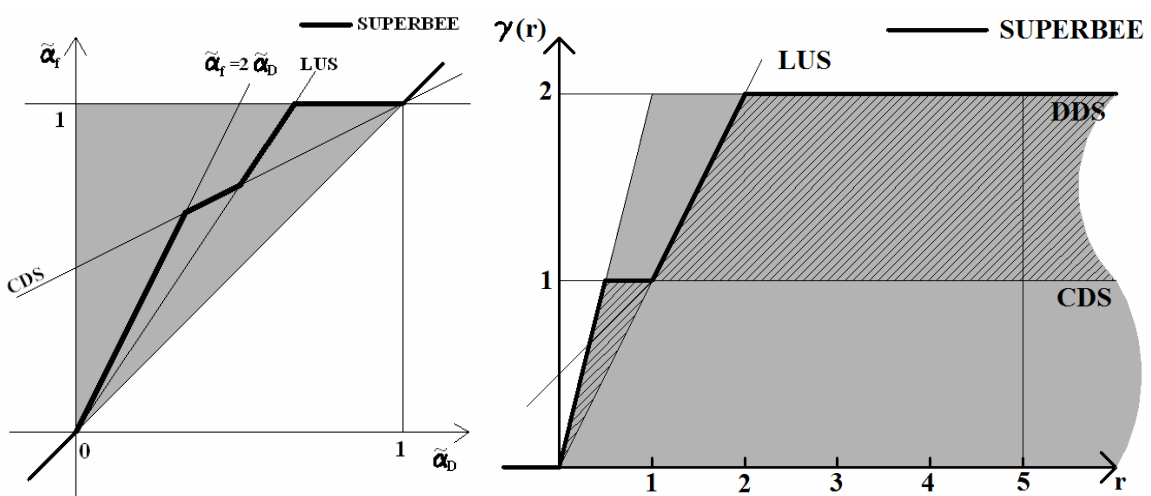


Figure 3.7 SUPERBEE

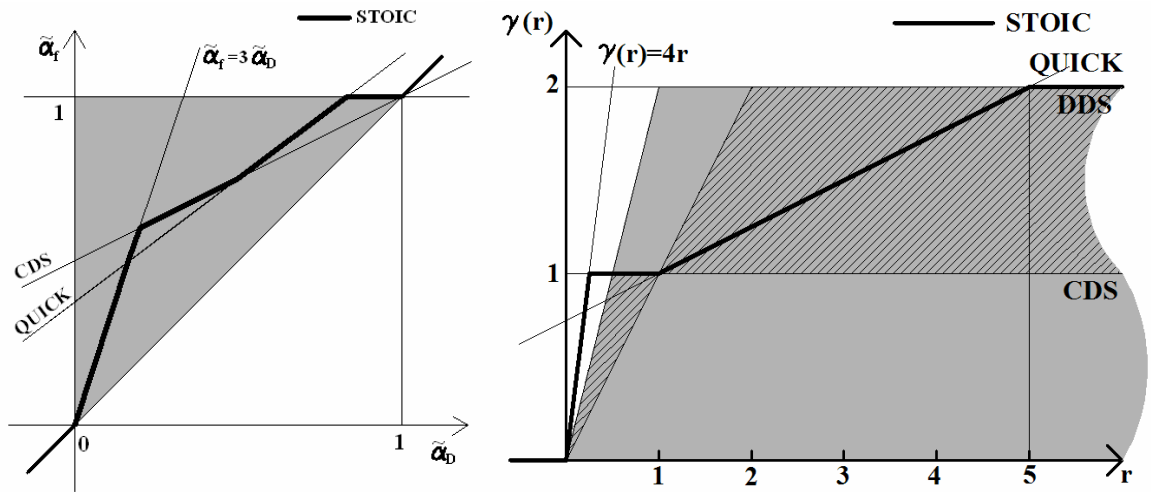


Figure 3.8 STOIC

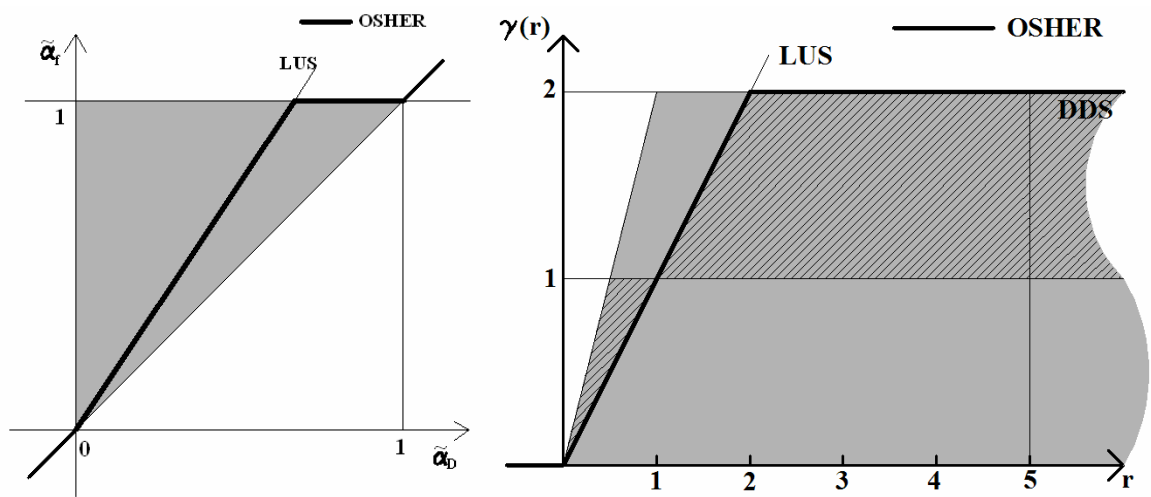


Figure 3.9 OSHER

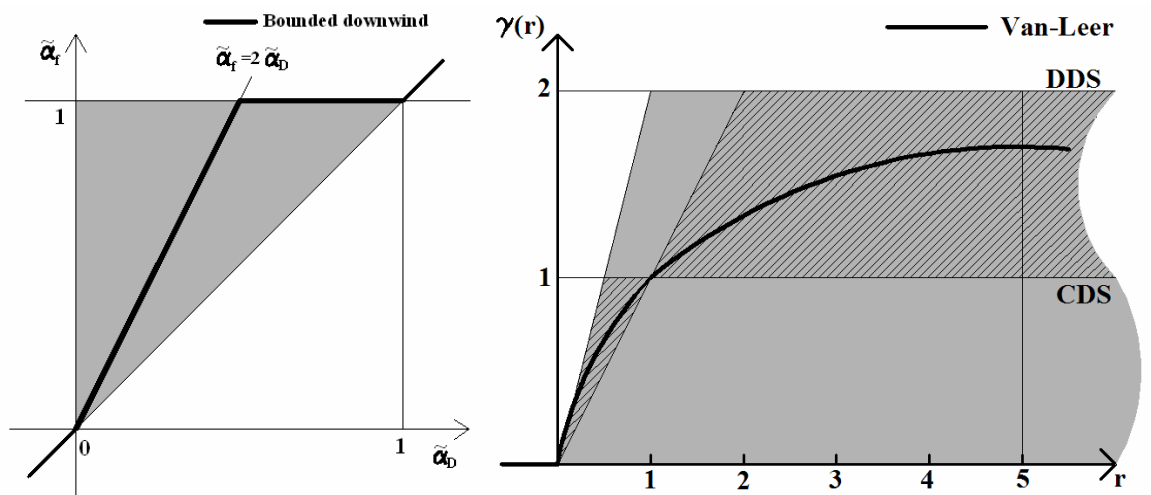


Figure 3.10 BDS

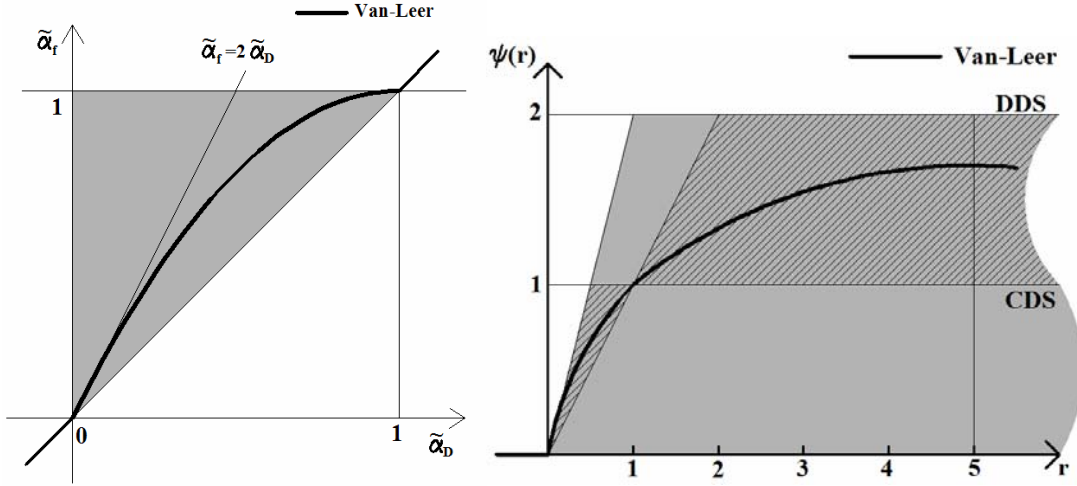


Figure 3.11 Van Leer

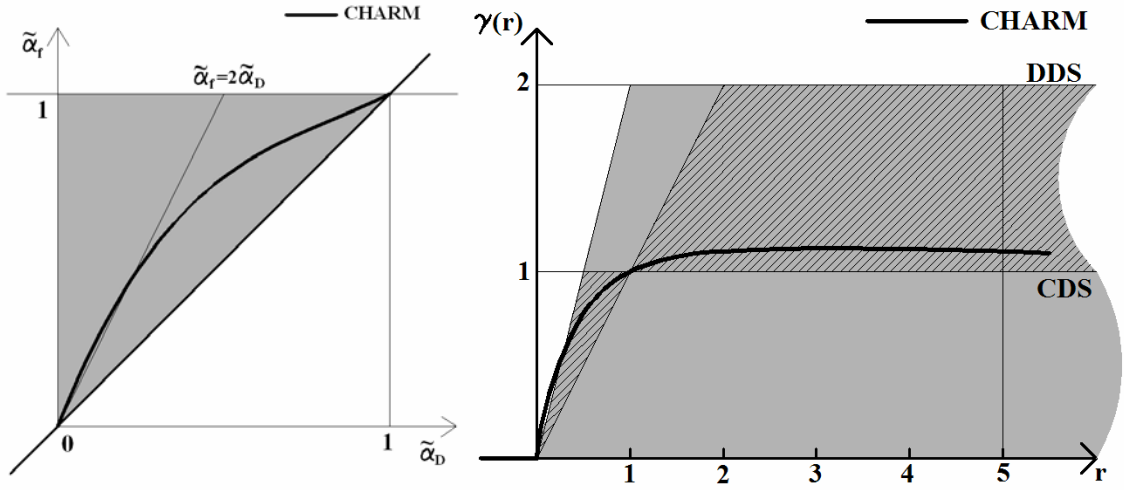


Figure 3.12 CHARM

3.5 The normalized variables for unstructured grids

For the unstructured grids, the upwind value α_U is required for variable normalization, but is not readily available. A estimation of α_U can be obtained with a pseudo-upwind node U located at a distance of negative $\bar{\delta}_{DA}$ away from donor node D (see Figure 3.13). Thus,

$$\alpha_U = \alpha_A - 2\nabla \alpha_D \cdot \bar{\delta}_{DA} \quad (3.10)$$

The above approximation is necessary to be bounded as:

$$\alpha_U = \min\{\max\{\alpha_U, 0\}, 1\} \quad (3.11)$$

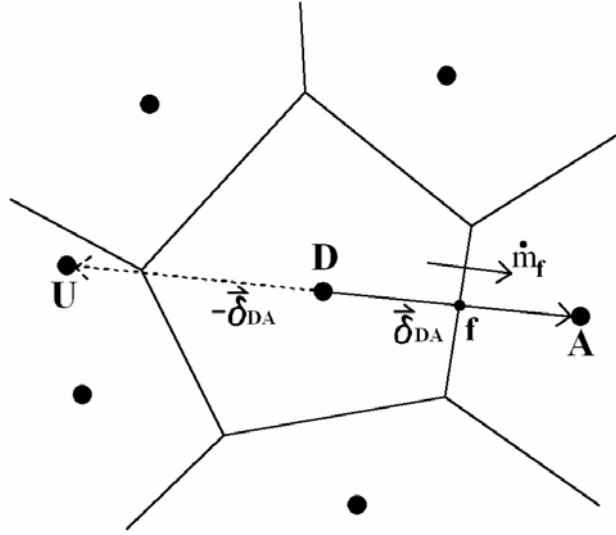


Figure 3.13. The prediction of upwind value for an arbitrary cell arrangement

3.6 Discretization of the indicator equation

Finite volume method is a popular method in CFD and will be applied in this study. This method uses the integral form of the conservation equations. The solution domain is divided into a finite number of control volumes, and the conservation equations are applied to each control volumes. The finite volume method is suitable for arbitrary geometries and can accommodate any type of grid. The finite volume approach is perhaps the simplest to understand and to program. All terms that need be approximated have physical meaning which is why it is popular with engineers.

The finite volume discretization of the equation (2.13) is performed by taking integration of the indicator equation over a control volume :

$$\iiint_{\forall} \frac{\partial \alpha}{\partial t} d\forall + \iiint_{\forall} \nabla \cdot \alpha \vec{V} d\forall = 0 \quad (3.12)$$

and then use the Gauss's divergence theory :

$$\iiint_{\forall} \frac{\partial \alpha}{\partial t} d\forall + \iint_S \alpha \vec{V} \cdot d\vec{S} = 0 \quad (3.13)$$

The first term at the left-hand-side is an unsteady term and can be discretized by:

$$\iiint_{\forall} \frac{\partial \alpha}{\partial t} d\forall \approx \frac{\Delta \forall}{\Delta t} (\alpha_D^n - \alpha_D^o) \quad (3.14)$$

where ΔV is the volume of the cell and the superscript n and o denoting new-time level and old-time level.

The second term at left hand side of equation (3.14) is the convection term and can be approximated as

$$\iint_S (\vec{V}\alpha) \cdot d\vec{S} \approx \sum_f (\vec{V}\alpha^o)_f \cdot \vec{S}_f \quad (3.15)$$

where the subscript f denoting that the properties on the surface of a control volume.

For the discretization, the first-order implicit scheme is computationally robust, stable and efficient, but suffers from numerical diffusion. On the other hand, the first-order explicit scheme is stable only for limited time steps. In the presenting work, we will adopt the second-order Crank-Nicolson scheme with large time steps.

In the equation (3.15), the value α_f is approximated by

$$\alpha_f = \frac{1}{2}(\alpha_f^n + \alpha_f^o) \quad (3.16)$$

Substituting above equation and using the approximation given in equation (3.1) in which the anti-diffusion term is treated as a fully explicit manner, the discretization of indicator equation can be presented as:

$$A_P \alpha_P^n = \sum_{nb} A_{nb} \alpha_{nb}^n + S_\alpha \quad (3.17)$$

where

$$A_P = \sum_{nb} A_{nb} + \frac{\Delta V}{\Delta t} \quad (3.18)$$

$$A_{nb} = \frac{1}{2} \max(-\dot{F}_v, 0) \quad (3.19)$$

$$S_\alpha = \sum_{nb} \left[\frac{1}{2} \max(-\dot{F}_v, 0) (\alpha_{nb}^o - \alpha_P^o) - \frac{\gamma(r)}{2} (\phi_A - \phi_D) \dot{F}_v \right] \quad (3.20)$$

where \dot{F}_v is the volume flux at each face, the subscript P denote the primary node and nb the neighbor node..

3.7 Blending strategy

To further enhance accuracy and reduce numerical diffusion and dispersion, composite schemes with blending strategy is introduced. There is a weighting factor based on the angle between interface and direction of motion. If the cell has started to be filled with fluid from the upwind side of the interface and the interface is parallel to the cell face, then only fluid present at the downwind cell should be convected through the cell face. In this case a compressive scheme should be used (see Figure 3.14(a)). However, if the interface is perpendicular to the cell face, a HR scheme would be appropriate (see Figure 3.14(b)).

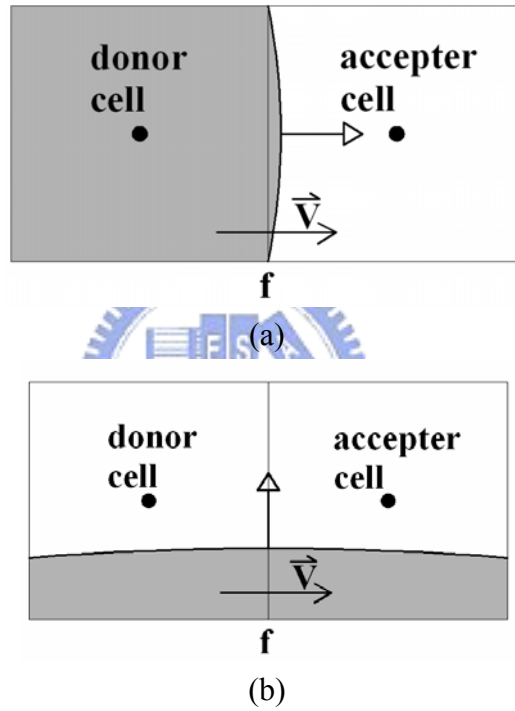


Figure 3.14 (a) the interface is parallel to the flow direction and the compressive scheme will be used

(b) the interface is perpendicular to the flow direction and high resolution schemes are appropriate.

The above-mentioned situations represent extreme cases in which the interface is either parallel or perpendicular to the control volume face. In general, the angle between the interface and control volume face is between these two cases. The normalized face value can be written as

$$\tilde{\alpha}_f = \tilde{\alpha}_{f(\text{compressive})} f(\theta_f) + \tilde{\alpha}_{f(\text{HR})} (1 - f(\theta_f)) \quad (3.21)$$

$$\text{where } \theta_f = \cos^{-1} \left| \frac{\nabla \alpha_f \cdot \vec{d}}{\|\nabla \alpha_f\| \|\vec{d}\|} \right|, \quad 0^\circ \leq \theta_f \leq 90^\circ$$

In the equation (3.21), $f(\theta_f)$ is a blending function between zero and one.

The following will introduce the HRIC, CICSAM and STACS schemes.

HRIC

The high-resolution volume tracking scheme (HRIC) [23] is base on a blending of the bounded downwind (BD in table 3.2) and upwind differencing schemes. The blending factor $f(\theta_f)$ is given by

$$f(\theta_f) = \sqrt{\cos(\theta_f)} \quad (3.22)$$

The normalized form of HRIC is:

$$\tilde{\alpha}_{f(HRIC)} = \begin{cases} \tilde{\alpha}_{f(BD)} f(\theta_f) + \tilde{\alpha}_{f(UDS)} (1 - f(\theta_f)), & Co_f < 0.3 \\ \left\{ \begin{aligned} &\tilde{\alpha}_{f(BD)} f(\theta_f) + \tilde{\alpha}_{f(UDS)} (1 - f(\theta_f)) + \\ &\left[\tilde{\alpha}_{f(BD)} f(\theta_f) + \tilde{\alpha}_{f(UDS)} (1 - f(\theta_f)) - \tilde{\alpha}_{f(UDS)} \right] \frac{0.7 - Co_f}{0.7 - 0.3} \end{aligned} \right\}, & 0.3 < Co_f < 0.7 \\ \tilde{\alpha}_{f(UDS)}, & Co_f > 0.7 \end{cases} \quad (3.23)$$

CICSAM

The Compressive Interface Capturing Scheme for Arbitrary Meshes (CICSAM) [25] scheme is also based on the blending strategy. The HYPER-C scheme and the ULTIMATE-QUICKEST (UQ) scheme are utilized when the cell face is perpendicular to the interface and the UQ employed when the face and the interface are parallel.

The HYPER-C scheme is

$$\tilde{\alpha}_f = \begin{cases} \tilde{\alpha}_D, & \tilde{\alpha}_D \geq 1 \text{ or } \tilde{\alpha}_D \leq 0 \\ \min \left(1, \frac{\tilde{\alpha}_D}{Co} \right), & 0 < \tilde{\alpha}_D < 1 \end{cases} \quad (3.24)$$

The ULTIMATE-QUICKEST scheme is

$$\tilde{\alpha}_f = \begin{cases} \tilde{\alpha}_D, & \tilde{\alpha}_D \geq 1 \text{ or } \tilde{\alpha}_D \leq 0 \\ \min \left\{ \frac{8Co\tilde{\alpha}_D + (1-Co)(6\tilde{\alpha}_D + 3)}{8}, \min \left\{ 1, \frac{\tilde{\alpha}_D}{Co} \right\} \right\}, & 1 > \tilde{\alpha}_D > 0 \end{cases} \quad (3.25)$$

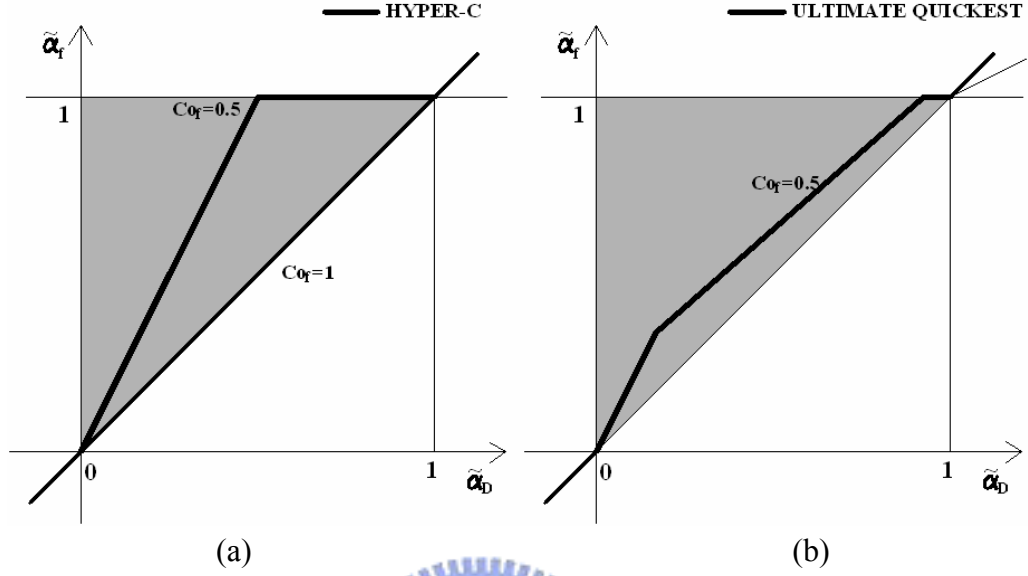


Figure 3.15 The NVD of (a) HYPER-C and (b) UQ at Co_f equal 0.5

Therefore, the CICSAM scheme can be written mathematically as

$$\tilde{\alpha}_{f(CICSAM)} = \tilde{\alpha}_{f(HYPER-C)} f(\theta_f) + \tilde{\alpha}_{f(UQ)} (1 - f(\theta_f)) \quad (3.26)$$

where the blending factor $f(\theta_f)$ is

$$f(\theta_f) = \min \left[\frac{\cos(2\theta_f) + 1}{2}, 1 \right] \quad (3.27)$$

STACS

The Switching Technique for Advection and Capturing of Surfaces (STACS) [24] scheme selects downwind differencing as compressive scheme and modified STOIC as high resolution scheme.

The $\tilde{\alpha}_{f(modified \text{ STOIC})}$ is obtained from

$$\tilde{\alpha}_{f(\text{modified STOIC})} = \begin{cases} \tilde{\alpha}_D, & \tilde{\alpha}_D \geq 1 \text{ or } \tilde{\alpha}_D \leq 0 \\ \frac{1}{2}(\tilde{\alpha}_D + 1), & \frac{1}{2} \geq \tilde{\alpha}_D > 0 \\ \frac{3}{4}\tilde{\alpha}_D + \frac{3}{8}, & \frac{5}{6} \geq \tilde{\alpha}_D > \frac{1}{2} \\ 1, & 1 > \tilde{\alpha}_D > \frac{5}{6} \end{cases} \quad (3.28)$$

The blending between the two schemes is preformed using

$$f(\theta_f) = [\cos^4(\theta_f)] \quad (3.29)$$

The normalized variables relationship for the STACS scheme is given by

$$\tilde{\alpha}_{f(STACS)} = \tilde{\alpha}_{f(DD)}f(\theta_f) + \tilde{\alpha}_{f(\text{modified STOIC})}(1 - f(\theta_f)) \quad (3.30)$$

The following Figures 3.16(a), 3.16(b) and 3.16(c) show the relationship between compressive schemes and high resolution schemes given by equations (3.22), (3.27) and (3.28) for the above composite schemes. In Chapter 5, these different blending factors will be compared in test cases.



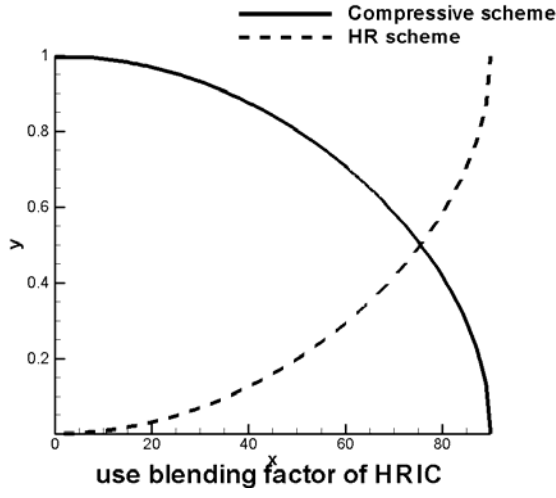


Figure 3.16a

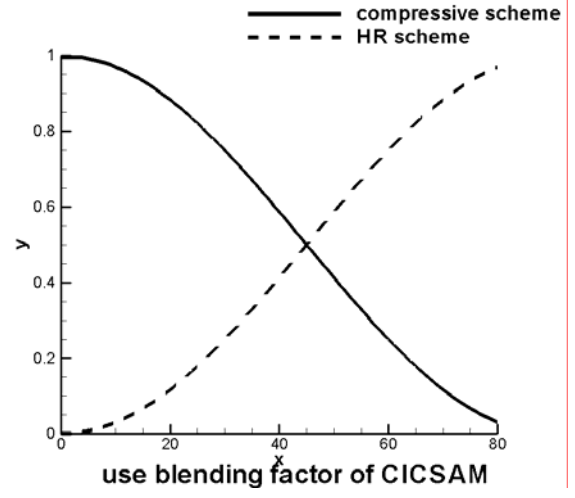


Figure 3.16b

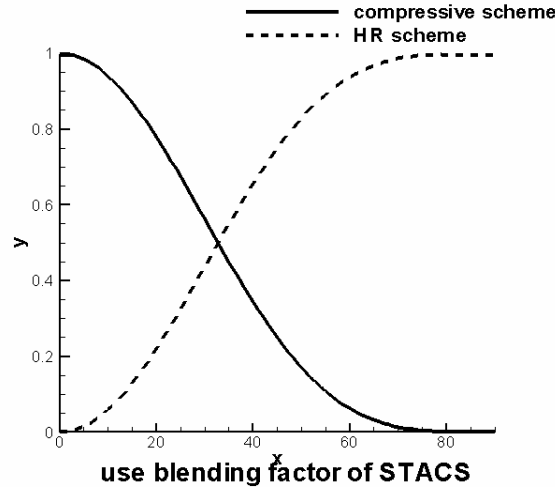


Figure 3.16c

Figure 3.16a, 3.16b and 3.16c show the relationship between two schemes for HRIC, CICSAM and STACS.

The x-axis stand for θ_f and y-axis means the value of $f(\theta_f)$.

Chapter 4 Numerical Method for the Velocity Field

4.1 Introduction

This chapter uses finite volume method to discretize momentum equation and pressure equation. All details of each term will be described. In this study, PISO algorithm is adopted to solve unsteady flow field.

4.2 Discretization

Take volume integral of the the momentum equation (2.5) to yield :

$$\iiint_{\forall} \rho \frac{\partial \phi}{\partial t} d\forall + \iiint_{\forall} \nabla \cdot (\rho \vec{V} \phi) d\forall = \iiint_{\forall} \nabla \cdot (\Gamma \nabla \phi) d\forall - \iiint_{\forall} \nabla P d\forall + \iiint_{\forall} \rho \vec{g} d\forall + \iiint_{\forall} \sigma \kappa \nabla \alpha d\forall \quad (4.1)$$

where ϕ designates each velocity component. The volume integral of the convection, diffusion and pressure terms can be transform into surface integral by divergence theory as

$$\iiint_{\forall} \rho \frac{\partial \phi}{\partial t} d\forall + \iint_S \rho \vec{V} \phi \cdot d\vec{S} = \iint_S \Gamma \nabla \phi \cdot d\vec{S} - \iint_S P d\vec{S} + \iiint_{\forall} \rho \vec{g} d\forall + \iiint_{\forall} \sigma \kappa \nabla \alpha d\forall \quad (4.2)$$

In the following the unsteady equation is treated with the use of fully implicit scheme, which is unconditionally stable in the linear analysis and allows larger time steps for unsteady calculation.

Unsteady term

The volume integral of the unsteady term can be discretized as

$$\iiint_{\forall} \rho \frac{\partial \phi}{\partial t} d\forall \approx \frac{\rho_p^o \Delta \forall}{\Delta t} (\phi_p^n - \phi_p^o) \quad (4.3)$$

The old time level term would be absorbed into the source term.

Convection fluxes

The surface integral for the convection term can be approximated by

$$\iint_S (\rho \vec{V} \phi) \cdot d\vec{S} \approx \sum_f (\rho \vec{V} \phi)_f \cdot \vec{S}_f = \sum_f F_f^c \quad (4.4)$$

Then,

$$F_f^c = \dot{m}_f \cdot \phi_f \quad (4.5)$$

where \dot{m}_f is the mass flux through the consider face.

As mentioned in the chapter 3, the convective flux is calculated as:

$$\phi_f = \phi_D + \gamma(r) \left(\frac{\phi_A - \phi_D}{2} \right) \quad (4.6)$$

where the subscript D denotes the donor node and A the acceptor node.

The convective fluxes at donor node and acceptor node can be calculated as:

$$\begin{cases} \phi_D = \phi_P, & \phi_A = \phi_{nb} & \text{for } \dot{m}_f > 0 \\ \phi_D = \phi_{nb}, & \phi_A = \phi_P & \text{for } \dot{m}_f < 0 \end{cases} \quad (4.7)$$

In the above the subscript P stands for the primary node, nb the neighbor node (see Figure 4.1)

In the momentum calculation the Van Leer scheme is adopted, which is given by

$$\gamma(r) = \frac{r + |r|}{r + 1} \quad (4.8)$$

In equation (4.6), the first term on the right-hand-side is treated implicit by while and the second term is moved into the source term.

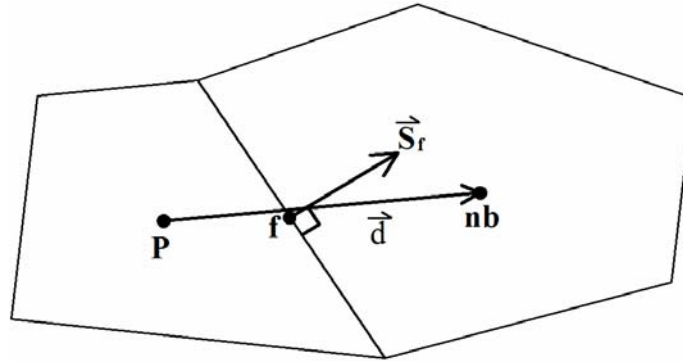


Figure 4.1 Illustration of the primary cell P and the neighbor cell nb with a consider face f.

Diffusion fluxes

The surface integral of the diffusion term is approximated by

$$\sum_f F_f^D = \sum_f (\mu_f^o \nabla \phi_f) \cdot \vec{S}_f \quad (4.9)$$

Let $\vec{S}_f = \vec{d} + (\vec{S}_f - \vec{d})$, when \vec{d} is a vector pointing in the direction from primary node to the neighbor node (Figure 4.1) defined by :

$$\vec{d} = \frac{|\vec{S}_f|^2}{\vec{\delta}_{Pnb} \cdot \vec{S}_f} \vec{\delta}_{Pnb} \quad (4.10)$$

The diffusion flux can then be expressed as:

$$F_f^D = \frac{\mu_f^o |\vec{S}_f|^2}{\vec{\delta}_{Pnb} \cdot \vec{S}_f} (\phi_{nb}^n - \phi_p^n) + \mu_f^o \nabla \phi_f^o \cdot (\vec{S}_f - \vec{d}) \quad (4.11)$$

in which the second term at the right-hand-side is also treated explicitly and is moved into the source term.

Pressure term

The surface integral is approximated as

$$\iint_s P d\vec{s} = \sum_f P_f^o \vec{S}_f = \nabla P^o \Delta \forall \quad (4.12)$$

Gravitational acceleration term

The gravitational acceleration term can be approximated as

$$\iiint_{\forall} \rho \vec{g} d\forall = \vec{g} \rho^o \Delta \forall \quad (4.13)$$

Surface tension term

The surface tension term in the equation (3.2) can be discretized as:

$$\iiint_{\forall} \sigma \kappa \nabla \alpha d\forall = \sigma \kappa_p (\nabla \alpha)_p \Delta \forall \quad (4.14)$$

As mentioned in the section 2.4, a smooth κ_p exists in the transitional region where $(\nabla \alpha)_p \neq 0$.

The gradient $(\nabla \alpha)_p$ is described as:

$$(\nabla \alpha)_p = \frac{1}{\Delta \forall} \sum_f \vec{S}_f \alpha_f \quad (4.15)$$

where α_f is the face value obtained via the interpolation from the two neighboring node values.

The curvature value which defined by equation (2.16) can be calculated by :

$$\kappa_P = - \left[\nabla \cdot \left(\frac{\nabla \alpha}{|\nabla \alpha|} \right) \right]_P = \frac{-1}{\Delta \nabla} \sum_f \bar{S}_f \cdot \left[\frac{(\nabla \alpha)_f}{|\nabla \alpha|_f} \right] \quad (4.16)$$

The face value $(\nabla \alpha)_f$ is calculated by interpolating from the neighboring node values.

Arrangement of the difference transport equation

The discretized momentum transport equation was approximated can be arranged as

$$A_P \phi_P^n = \sum_{nb} A_{nb} \phi_{nb}^n + S - \nabla P^o \Delta \nabla \quad (4.17)$$

in which

$$A_P = \sum_{nb} A_{nb} + \rho_P^o \frac{\Delta \nabla}{\Delta t}$$

$$A_{nb} = \frac{\mu_f^o |\bar{S}_f|^2}{\bar{\delta}_{Pnb} \cdot \bar{S}_f} + \max(-\dot{m}_f, 0)$$

$$S = \sum_f \left\{ -\dot{m}_f \frac{\gamma(r)}{2} (\phi_A - \phi_D) + \mu_f^o \nabla \phi_f^o (\bar{S}_f - \bar{d}) \right\}$$

$$+ \rho_P^o \frac{\Delta \nabla}{\Delta t} \phi^o + \bar{g} \rho_P^o \Delta \nabla + \sigma \kappa (\nabla \alpha_P^o) \Delta \nabla$$

where the source term S includes old-time level unsteady term, the anti-diffusion term, the cross diffusion term, the gravitational term and the surface tension term.

4.3 Pressure-velocity coupling with PISO

A non-iterative method named PISO which stands for Pressure-Implicit with Splitting of Operators proposed by Issa [23] for unsteady incompressible flow is used in the present study. This breakthrough of PISO is attributed to the few more correctors at each time step while SIMPLE has only one corrector proceeded at each iteration step. PISO involve one predictor step and two corrector steps. It is described in the following.

Predictor step

The predictor step is to solve the momentum equation using the prevailing pressure field.

$$A_P \vec{V}_P^* = \sum_{nb} A_{nb} \vec{V}_{nb}^* + (S - \nabla P_P^o \Delta \nabla) \quad (4.18)$$

The above equation solves the velocity field but the conservation of volume flux has not

been satisfied yet. For the purpose of satisfying the continuity equation (2.12), the velocity at face needs to be calculated. The above equation can be rewritten as:

$$\vec{V}_P^* = \overline{H}_P^* - \left(\frac{\Delta \nabla}{A_P} \right)_P \nabla P_P^o \quad (4.19)$$

$$\text{where } \overline{H}_P^* = \frac{\sum_{nb} A_{nb} \vec{V}_{nb}^* + S}{A_P}$$

Similarly, the relationship between velocity and pressure on the control surface can be deduced as:

$$\vec{V}_f^* = \overline{H}_f^* - \left(\frac{\Delta \nabla}{A_P} \right)_f \nabla P_f^o \quad (4.20)$$

where

$$\overline{H}_f^* = \overline{\vec{V}}_f^* + \left(\frac{\Delta \nabla}{A_P} \right)_f \overline{\nabla P_f^o} \quad (4.21)$$

In the equation (4.19), the superscript “ $\overline{}$ ” stands for the value interpolated from the primary cell P and the neighbor cell C with a weighting factor w_f .

$$\overline{\nabla P_f^o} = w_f \nabla P_{nb}^o + (1 - w_f) \nabla P_P^o \quad (4.22)$$

$$\overline{\vec{V}}_f^* = w_f \vec{V}_{nb}^* + (1 - w_f) \vec{V}_P^* \quad (4.23)$$

Substituting equation (4.21) into equation (4.20) to obtain:

$$\vec{V}_f^* = \left[\overline{\vec{V}}_f^* + \left(\frac{\Delta \nabla}{A_P} \right)_f \overline{\nabla P_f^o} \right] - \left(\frac{\Delta \nabla}{A_P} \right)_f \nabla P_f^o \quad (4.24)$$

where $\left(\frac{\Delta \nabla}{A_P} \right)_f$ is an average value of primary cell and neighbor cell.

$$\left(\frac{\Delta \nabla}{A_P} \right)_f = \frac{1}{2} \left[\left(\frac{\Delta \nabla}{A_P} \right)_P + \left(\frac{\Delta \nabla}{A_P} \right)_{nb} \right] \quad (4.25)$$

The volume flux at face can be calculate by :

$$\begin{aligned}
\dot{V}_f^* &= \vec{V}_f^* \cdot \vec{S}_f = \overline{\vec{V}}_f^* \cdot \vec{S}_f - \left(\frac{\Delta \nabla}{A_p} \right)_f (\nabla P_f^* - \overline{\nabla P_f^o}) \cdot \vec{S}_f \\
&\approx \overline{\vec{V}}_f^* \cdot \vec{S}_f - \left(\frac{\Delta \nabla}{A_p} \right)_f (\nabla P_f^* - \overline{\nabla P_f^o}) \cdot \vec{d}
\end{aligned} \tag{4.26}$$

First corrector step

After the predictor step a velocity field denoted $*$ is obtained. In this corrector step both the velocity and pressure fields are adjusted such that the continuity equation is satisfied. The corrected velocity is denoted by \vec{V}^{**} and the corrected pressure by P^* . They satisfy the following momentum equation.

$$A_p \vec{V}_p^{**} = \sum_{nb} A_{nb} \vec{V}_{nb}^* + (S - \nabla P_p^* \Delta \nabla) \tag{4.27}$$

Dividing the equation by A_p yields:

$$\vec{V}_p^{**} = \overline{H}_p^* - \left(\frac{\Delta \nabla}{A_p} \right)_p \nabla P_p^* \tag{4.28}$$

Substituting equation(4.19) from this equation yields a velocity correction equation.

$$\vec{V}_p' = - \left(\frac{\Delta \nabla}{A_p} \right)_p \nabla P_p' \tag{4.29}$$

where $V' \equiv V^{**} - V^*$, $P' \equiv P^* - P^o$.

The velocity correction at cell face can be written in a similar manner.

$$\vec{V}_f' = - \left(\frac{\Delta \nabla}{A_p} \right)_f \nabla P_f' \tag{4.31}$$

The volume flow rate corrector can be obtained from the velocity correction by

$$\dot{V}_f' = \vec{V}_f' \cdot \vec{S}_f = \left[- \left(\frac{\Delta \nabla}{A_p} \right)_f \nabla P_f' \right] \cdot \vec{S}_f \tag{4.30}$$

which can be further rearranged into the following form:

$$\begin{aligned}
\dot{v}'_f &= -\left(\frac{\Delta \nabla}{A_p}\right)_f \nabla P'_f \cdot [\bar{d} + (\bar{S}_f - \bar{d})] \\
&= -\left[\left(\frac{\Delta \nabla}{A_p}\right)_f \frac{|\bar{S}_f|^2}{\bar{\delta}_{Pnb} \cdot \bar{S}_f} (\nabla P'_f \cdot \bar{\delta}_{Pnb}) + \left(\frac{\Delta \nabla}{A_p}\right)_f \nabla P'_f \cdot (\bar{S}_f - \bar{d})\right] \\
\text{where } \bar{d} &= \frac{|\bar{S}_f|^2}{\bar{\delta}_{nb} \cdot \bar{S}_f} \bar{\delta}_{nb}.
\end{aligned} \tag{4.31}$$

Replacing the term $\nabla P'_f \cdot \bar{\delta}_{Pnb}$ by $P'_{nb} - P'_p$ yields:

$$\dot{v}'_f = -\left[\left(\frac{\Delta \nabla}{A_p}\right)_f \frac{|\bar{S}_f|^2}{\bar{\delta}_{Pnb} \cdot \bar{S}_f} (P'_{nb} - P'_p) + \left(\frac{\Delta \nabla}{A_p}\right)_f \nabla P'_f \cdot (\bar{S}_f - \bar{d})\right] \tag{4.32}$$

Hence, the corrected velocity can be presented as:

$$\dot{v}^{**}_f = \dot{v}^*_f - \left[\left(\frac{\Delta \nabla}{A_p}\right)_f \frac{|\bar{S}_f|^2}{\bar{\delta}_{Pnb} \cdot \bar{S}_f} (P'_{nb} - P'_p) + \left(\frac{\Delta \nabla}{A_p}\right)_f \nabla P'_f \cdot (\bar{S}_f - \bar{d})\right] \tag{4.33}$$

The discretization of the continuity equation leads to:

$$\sum_f \dot{v}^{**}_f = \sum_f \dot{v}^*_f + \sum_f \dot{v}'_f = 0 \tag{4.34}$$

Substituting equation (4.33) into above equation, a pressure correction equation is obtained :

$$A_p^p P'_p = \sum_f A_{nb}^p - \sum_f \dot{v}^*_f + S_{p1} + S_{p2} \tag{4.35}$$

where

$$A_p^p = \sum_f A_{nb}^p$$

$$A_{nb}^p = \left(\frac{\Delta \nabla}{A_p}\right)_f \frac{|\bar{S}_f|^2}{\bar{\delta}_{nb} \cdot \bar{S}_f}$$

$$S_{p1} = -\sum_f \dot{v}^*_f$$

$$S_{p2} = \sum_f \left(\frac{\Delta \nabla}{A_p}\right)_f \nabla P'_f \cdot (\bar{S}_f - \bar{d})$$

Second corrector step

In the second corrector step the velocity and pressure fields are further adjusted \vec{V}^{***}

and P^{**} as :

$$A_p \vec{V}_p^{***} = \sum_f A_{nb} \vec{V}_{nb}^{**} + (S - \nabla P_p^{**} \Delta \nabla) \quad (4.36)$$

Substituting equation (4.28) for this equation, a second velocity correction is obtained as :

$$\vec{V}_p'' = \left(\frac{\sum_f A_{nb} \vec{V}_{nb}'}{A_p} \right)_f - \left(\frac{\Delta \nabla}{A_p} \right)_f \nabla P_f'' \quad (4.37)$$

where $V'' \equiv V^{***} - V^{**}$, $V' \equiv V^{**} - V^*$, $P'' \equiv P^{**} - P^*$.

The corrected volume flux at a consider face is

$$\dot{V}_f'' = \dot{V}_f^{***} - \dot{V}_f^{**} \quad (4.38)$$

Similarly, the volume flow rate corrector is

$$\dot{V}_f'' = \left[\left(\frac{\sum_f A_{nb} \vec{V}_{nb}'}{A_p} \right)_f - \left(\frac{\Delta \nabla}{A_p} \right)_f \nabla P_f'' \right] \cdot \vec{S}_f \quad (4.39)$$

In the first correction step $\sum_f \dot{V}_f^{**}$ is obtained and equal to zero. Enforcing the velocity \vec{V}^{***}

to satisfy the continuity equation yields:

$$\sum_f \dot{V}_f^{***} = \sum_f \cancel{\dot{V}_f^{**}} + \sum_f \dot{V}_f'' = 0 \quad (4.40)$$

Substituting equation (4.39) into (4.40), the second corrector step can be arranged as:

$$A_p^P = \sum_f A_{nb}^P P_{nb}' + S_{P1}^2 + S_{P2}^2 \quad (4.41)$$

where

$$\begin{aligned}
A_p^P &= \sum_f A_{nb}^P \\
A_{nb}^P &= \left(\frac{\Delta \forall}{A_p} \right)_f \frac{|\vec{S}_f|^2}{\vec{\delta}_{Pnb} \cdot \vec{S}_f} \\
S_{p1}^2 &= - \left(\frac{\sum_f A_{nb} \vec{V}_{nb}'}{A_p} \right)_f \cdot \vec{S}_f \\
S_{p2}^2 &= \sum_f \left(\frac{\Delta \forall}{A_p} \right)_f \nabla P_f'' \cdot (\vec{S}_f - \vec{d})
\end{aligned}$$

Although more corrector steps are needed completed satisfy for the conservation law, two corrector steps are sufficient to have the accuracy of solution within temporal truncation error.

The source term of each algebraic pressure correction equation has been divided into two parts. The first part is accounting for the orthogonality of structured grids, whereas the second one is due to the non-orthogonality of unstructured grids.

4.4 Solution procedure for the two-fluid system

All equations have been discretized and the coupling velocity and pressure has been addressed. It is now to describe the solution procedure of the two-fluid system.

The solution procedure for the two-fluid system is:

1. Initialize all variables at initial time t_0
2. Solve the VOF equation for volume fraction α by using the old time level volumetric fluxes.
3. Update the coefficients of the momentum equations. Use the new α values to obtain an estimate for new viscosity and density.
4. Solve the momentum equation and continue with PISO algorithm.
5. If the final time step has not been reached, advance to the next time step and return to step 2.

Chapter 5 Results and Discussion

5.1 Introduction

A CFD methodology for the volume tracking methods was introduced in the previous chapter. In this chapter, the methodology will be tested against analytical solution and experimental data. The test cases selected are:

- ♦ Uniform density flow calculation free from gravity and surface tension force. The velocity field is specified without solving momentum equation. First, linear schemes and non-linear schemes are tested. Furthermore, different composite schemes are tested and compared with well-known schemes which are based on blending strategy. In the numerical results, the combination of SUPERBEE as compressive scheme and MUSCL as high resolution scheme is selected and is adopted in the following cases.
- ♦ Surface tension forces apply to a square bubble. In this case, gravity is neglected.
- ♦ The simulation of droplet splashing demonstrates the merging of two independent regions
- ♦ An air bubble in water is another air/water computational example.
- ♦ Inviscid and viscous, low amplitude sloshing.
- ♦ Rayleigh-Taylor instability. This case is density-driven and only influenced by gravity.
- ♦ Column collapse with and without a small obstacle
- ♦ A hydraulic bore.

5.2 The VOF schemes test in an oblique velocity field

Two different hollow shapes are convected in an oblique velocity field and Figure 5.1 presents the initial condition of these two shapes. The following describe the information about these two shapes as:

1. A hollow square (Figure 5.1(a)) aligned with the coordinate axes of an outer side length 0.8 and inner side length 0.4.
2. A hollow circle (Figure 5.1(b)) with an outer diameter of length 0.4 and inner diameter of 0.8. Because the volume fraction of each cell can not be obtained easily, there is a special

treatment for the initial setting. In the transition region, the physical surface intersects the cell faces in two points. An approximated surface can be obtained by connecting these two points with a straight line. This line and cell faces build an approximated area (see the hitched area in Figure 5.2). Thus, the portion of an approximated area of a consider cell is the volume fraction value.

The computational domain is a 4×4 square, subdivided into 100×100 grids. All shapes are initially at (0.8, 0.8) with their exact positions centered at (2.8, 1.8) after 1.0 seconds. Three different time steps, $\Delta t = 0.00333$, 0.00667 and 0.01, yield Courant number of 0.25, 0.5, 0.75 which will be denoted by low, medium and high, over the uniform grid systems. Contours are display for $0.05 \leq \alpha \leq 0.95$ with 10 levels.

For the purpose of comparison the solution errors, the solution error defined as [36]:

$$E = \frac{\sum_{i=1}^{all \ cell} |\alpha_i^n \Delta \nabla_i - \alpha_i^a \Delta \nabla_i|}{\sum_{i=1}^{all \ cell} \alpha_i^o \Delta \nabla_u} \quad (5.1)$$

where α^n is the calculated solution after n time steps, α^a the analytical solution, and α^o the initial condition.



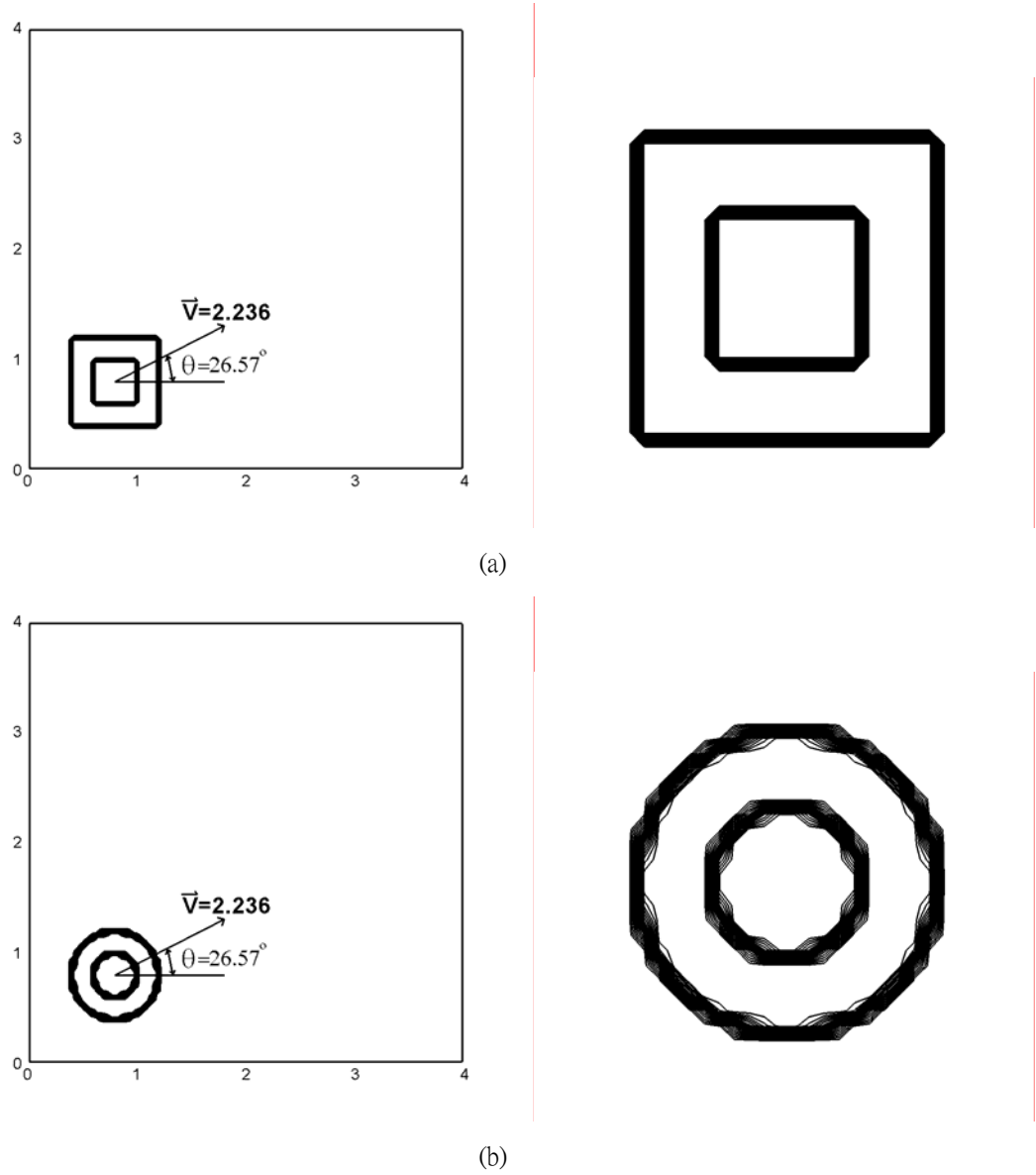


Figure 5.1 The flow field domain and initial condition of (a) hollow square, (b) hollow circle

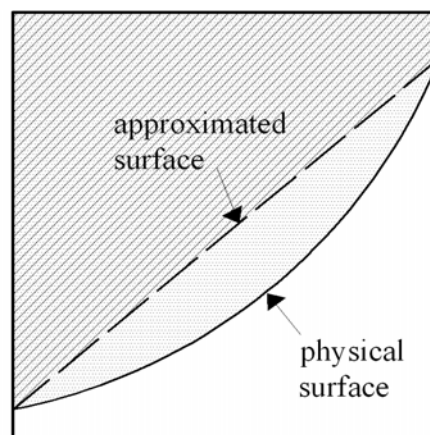


Figure 5.2 Method for catching the value of volume fraction.

The comparison of different schemes

There are many linear and non-linear schemes are considered for solving indicator equation. Linear schemes are upwind difference scheme, central difference scheme, downwind difference scheme and cubic upwind scheme (CUS in Table 3.1). These linear schemes are revised and satisfy the convective boundedness criteria (CBC). In other words, the normalized volume fraction value at a consider face $\tilde{\alpha}_f$ tracks the upwind difference line in NVD while the donor cell value $\tilde{\alpha}_D$ less than zero or greater than unity. Some famous non-linear schemes are chosen in the test and these schemes (see Figure 5.3 and 5.4) are Bounded Downwind scheme (BD), SMART, MUSCL, OSHER, Van Leer, CHARM and SUPERBEE. The NVD equation and flux limiter function of these non-linear schemes are detailed in Table 3.2.

Among these schemes, upwind difference scheme is a diffusive scheme in each case. Downwind difference scheme produces highly numerical dispersion and compress shapes, especially at high Courant number (CN=0.75). In hollow circle, downwind difference scheme transforms the original shape into a polygon. Bounded downwind (BD) scheme and SUPERBEE are more accurate but compress shapes in hollow circle case (see Figure 5.4 (c)). These two schemes are taken as compressive schemes in composite scheme tests. Cubic upwind difference scheme, MUSCL, STOIC and Van Leer are treated as high resolution scheme in the blending strategy when the flow direction perpendicular to interface.


Scheme	Upwind	Central Difference	Downwind	Bounded Downwind
Error	1.25E+00	7.59E-01	6.49E-01	3.52E-01
	Min: 0.000	Min:-0.040	Min:-0.464	Min:-0.013
	Max: 0.472	Max:0.989	Max:1.467	Max:0.949
				
Scheme	Cubic Upwind	SMART	MUSCL	STOIC
Error	5.97E-01	6.50E-01	5.93E-01	6.40E-01
	Min:-0.030	Min:-0.021	Min:-0.005	Min:-0.022
	Max:1.002	Max:0.933	Max:0.844	Max:0.961
				
Scheme	OSHER	Van Leer	CHARM	SUPERBEE
Error	7.37E-01	6.87E-01	7.47E-01	4.47E-01
	Min: 0.000	Min: 0.000	Min: -0.003	Min:-0.009
	Max:0.751	Max: 0.783	Max: 0.798	Max0.915:
				

Figure 5.3 (a) Comparison of different schemes with grids 100*100 and Courant number=0.75 ($\Delta t=0.01$)

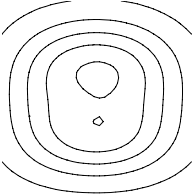
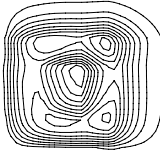
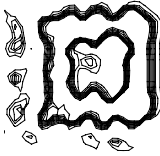
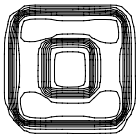


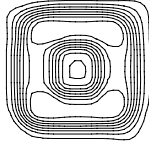
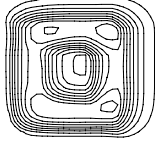
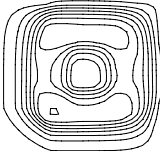
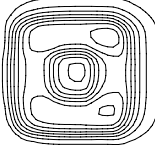
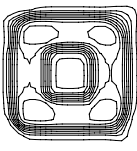
Scheme	Upwind	Central Difference	Downwind	Bounded Downwind
Error	1.25E+00	7.23E-01	4.39E-01	3.51E-01
	Min:0.000	Min:-0.028	Min:-0.444	Min:-0.007
	Max:0.471	Max:0.999	Max:1.344	Max:0.926
				
Scheme	Cubic Upwind	SMART	MUSCL	STOIC
Error	5.45E-01	6.11E-01	5.81E-01	5.95E-01
	Min:-0.017	Min:-0.002	Min:0.000	Min:-0.004
	Max:0.980	Max:0.873	Max:0.842	Max:0.899
				
Scheme	OSHER	Van Leer	CHARM	SUPERBEE
Error	7.55E-01	6.76E-01	7.24E-01	4.40E-01
	Min:0.000	Min:0.000	Min:0.000	Min:0.000
	Max:0.751	Max:0.774	Max:0.787	Max:0.901
				

Figure 5.3(b) Comparison of different schemes with grids 100*100 and Courant number=0.50 ($\Delta t=0.00667$)

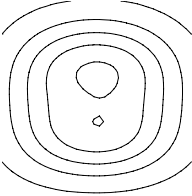

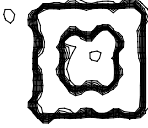
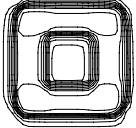
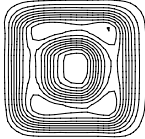
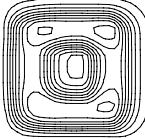
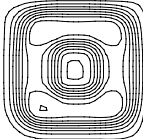
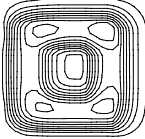
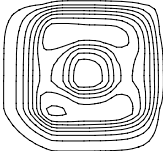
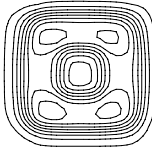
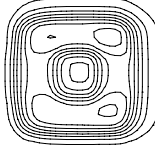
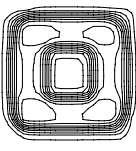
Scheme	Upwind	Central Difference	Downwind	Bounded Downwind
Error	1.25E+00	6.90E-01	2.03E-01	3.40E-01
	Min:0.000	Min:-0.010	Min:-0.206	Min:-0.002
	Max:0.471	Max:0.954	Max:1.190	Max:0.943
				
Scheme	Cubic Upwind	SMART	MUSCL	STOIC
Error	5.15E-01	5.72E-01	5.80E-01	5.46E-01
	Min:-0.013	Min:0.000	Min:0.000	Min:0.000
	Max:0.952	Max:0.874	Max:0.851	Max:0.891
				
Scheme	OSHER	Van Leer	CHARM	SUPERBEE
Error	7.69E-01	6.74E-01	7.04E-01	4.27E-01
	Min:0.000	Min:0.000	Min:0.000	Min:0.000
	Max:0.761	Max:0.782	Max:0.783	Max:0.914
				

Figure 5.3(c) Comparison of different schemes with grids 100*100 and Courant number=0.25 ($\Delta t=0.00333$)

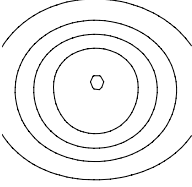
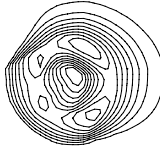
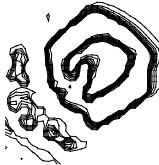
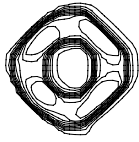

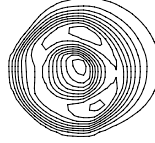
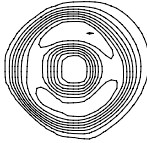
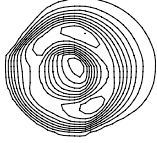
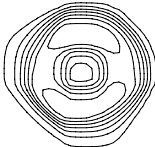
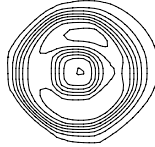
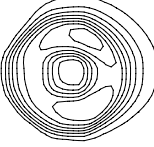
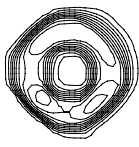
Scheme	Upwind	Central Difference	Downwind	Bounded Downwind
Error	1.23E+00	7.01E-01	7.11E-01	2.25E-01
	Min:0.000	Min:-0.060	Min:-0.537	Min:-0.062
	Max:0.452	Max:0.944	Max:1.454	Max:1.039
				
Scheme	Cubic Upwind	SMART	MUSCL	STOIC
Error	5.39E-01	5.85E-01	5.18E-01	5.70E-01
	Min:-0.045	Min:-0.026	Min:-0.006	Min:-0.03
	Max:0.983	Max:0.912	Max:0.852	Max:0.952
				
Scheme	OSHER	Van Leer	CHARM	SUPERBEE
Error	6.57E-01	6.23E-01	6.85E-01	3.17E-01
	Min:0.000	Min:0.000	Min:-0.007	Min:-0.024
	Max:0.728	Max:0.780	Max:0.796	Max:0.990
				

Figure 5.4(a) Comparison of different schemes with grids 100*100 and Courant number=0.75 ($\Delta t=0.01$)

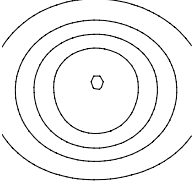
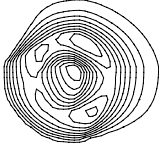

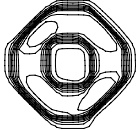
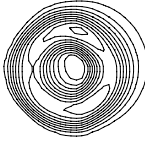
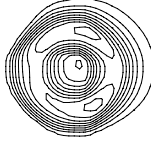
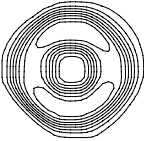

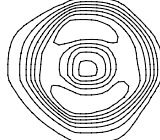


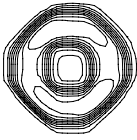
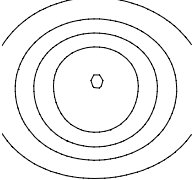
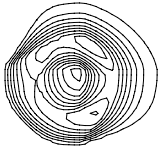

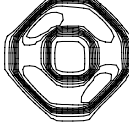
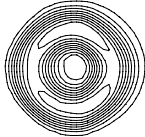
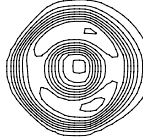
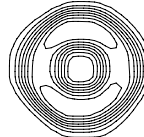
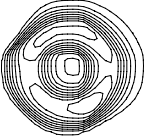
Scheme	Upwind	Central Difference	Downwind	Bounded Downwind
Error	1.23E+00	6.46E-01	5.45E-01	2.47E-01
	Min:0.000	Min:-0.034	Min:-0.380	Min:-0.037
	Max:0.452	Max:0.936	Max:1.371	Max:1.020
				
Scheme	Cubic Upwind	SMART	MUSCL	STOIC
Error	4.67E-01	5.31E-01	4.99E-01	5.08E-01
	Min:-0.022	Min:-0.005	Min:-0.002	Min:-0.010
	Max:0.969	Max:0.873	Max:0.823	Max:0.905
				
Scheme	OSHER	Van Leer	CHARM	SUPERBEE
Error	6.81E-01	6.07E-01	6.59E-01	3.22E-01
	Min:0.000	Min:0.000	Min:0.000	Min:-0.014
	Max:0.730	Max:0.761	Max:0.783	Max:0.948
				

Figure 5.4(b) Comparison of different schemes with grids 100*100 and Courant number=0.50 ($\Delta t=0.00667$)

Scheme	Upwind	Central Difference	Downwind	Bounded Downwind
Error	1.23E+00	6.03E-01	3.29E-01	2.36E-01
	Min:0.000	Min:-0.012	Min:-0.211	Min:-0.016
	Max:0.452	Max:0.909	Max:1.202	Max:0.997
				

Scheme	Cubic Upwind	SMART	MUSCL	STOIC
Error	4.22E-01	4.85E-01	4.95E-01	4.50E-01
	Min:-0.014	Min:0.000	Min:0.000	Min:0.000
	Max:0.943	Max:0.869	Max:0.832	Max:0.913
				

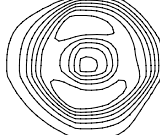
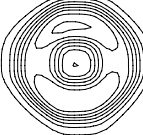

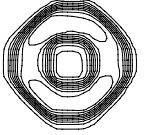
Scheme	OSHER	Van Leer	CHARM	SUPERBEE
Error	6.98E-01	6.03E-01	6.34E-01	3.12E-01
	Min:0.000	Min:0.000	Min:0.000	Min:-0.006
	Max:0.733	Max:0.760	Max:0.753	Max:0.942
				

Figure 5.4(c) Comparison of different schemes with grids 100*100 and Courant number=0.25 ($\Delta t=0.00333$)

The comparison of composite schemes

As mentioned in the section 3.6, the blending strategy and composite schemes are introduced. When the normal vector of interface is parallel to the flow direction, compressive scheme is used. On the other hand, in the case of the normal vector of interface is perpendicular to the flow direction, it is proper to adopt high resolution scheme. There are three well-known composite schemes, HRIC scheme of Muzafferija [28], CICSAM scheme of Ubbink [30] and STACS of Darwish [29]. The following Figure 5.5 and 5.7 show the hollow square and hollow circle using HRIC, CICSAM and STACS schemes.

HRIC scheme is base on a blending of the Bounded Downwind Scheme and Upwind Differencing Scheme. Because bounded downwind is compressive and introduces negative numerical diffusion, the original shapes hollow circle and hollow square are compressed. CICSAM scheme is based on the blending the HYPER-C scheme and the ULTIMATE-QUICKEST (UQ) scheme. Similarly, Upwind Different Scheme plays an important role and numerical diffusion is produced at high Courant number. STACS scheme has strong oscillation which caused by Downwind Difference Scheme. These well-known schemes all well performed in the case of hollow square especially at lower Courant number.

Figure 5.6 and Figure 5.8 illustrate the numerical of composite schemes. The former takes as compressive scheme and the later treats high resolution scheme. In the above mentioned, it is clear that Bounded Downwind Scheme and SUPERBEE scheme is more compressive. The combinations of SUPERBEE or Bounded Downwind scheme, which are taken as compressive schemes, with other high resolution schemes (STOIC, MUSCL, Van Leer and cubic upwind difference scheme (CUS)) are tested. Because Bounded Downwind Scheme introduces too much numerical dispersion and compress shapes strongly, SUPERBEE scheme is the better choice. The SUPERBEE/Cubic Upwind scheme introduces lower error but violets the boundedness criteria and cause divergence in the computation process. In the hollow circle test, the SUPEREE/Van Leer and SUPERBEE/STOIC scheme introduce numerical diffusion in the flow direction. By the comparison of numerical results, the blending of SUPERBEE and MUSCL is a proper choice.

The results are performed well at lower Courant number but cost too much computational resource. On the other hand, Numerical diffusion or dispersion will increase with Courant number. In conclusion, to derive reasonable and acceptable numerical simulations, the Courant number has to be limited under a proper value. In the following, the Courant number in each case are described in detail.



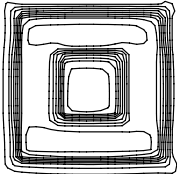
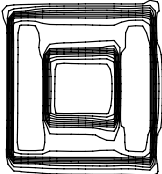
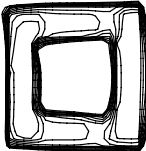
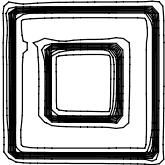
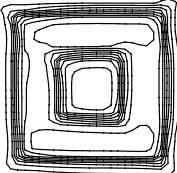
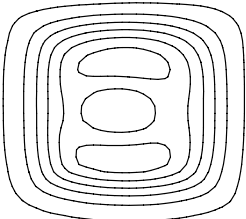
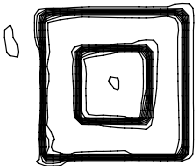
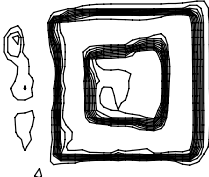
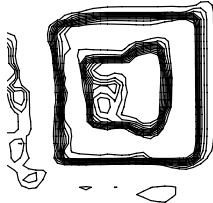
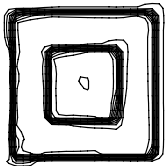
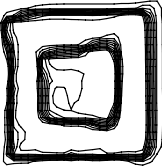
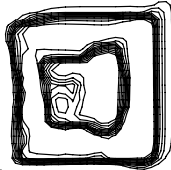
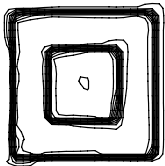
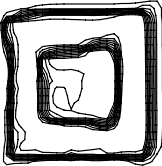
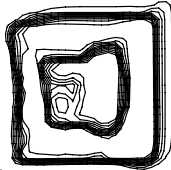
Scheme\Co.	0.25	0.5	0.75
HRIC	Error:3.72E-01 Min:0.000 Max:0.904	Error:1.92E-01 Min:-0.056 Max:1.051	Error:2.43E-01 Min:-0.018 Max:1.024
			
	Error:1.22E-01 Min:0.000 Max:0.990	Error:3.899E-01 Min:0.000 Max:0.887	Error:1.00E+00 Min:0.000 Max:0.603
CICSAM			
	Error:1.14E-01 Min:-0.147 Max:1.092	Error:2.567E-01 Min:-0.245 Max:1.237	Error:4.26E-01 Min:-0.379 Max:1.324
			
STACS			
	Error:1.14E-01 Min:-0.147 Max:1.092	Error:2.567E-01 Min:-0.245 Max:1.237	Error:4.26E-01 Min:-0.379 Max:1.324
			

Figure 5.5 Comparison of HRIC, CICSAM and STACS with grids 100*100.

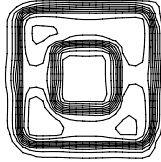
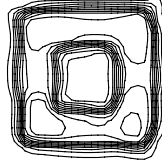
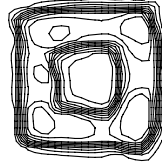
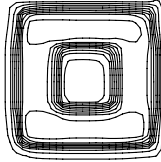
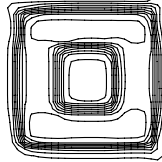
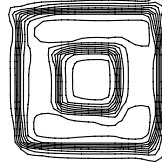
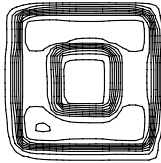
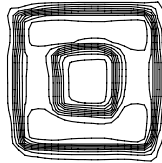
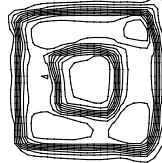
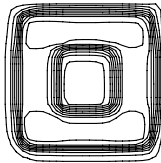
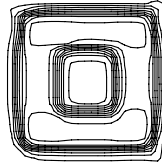
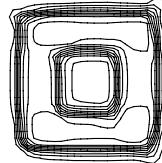
Scheme\Co.	0.25	0.5	0.75
Bounded Downwind / Cubic Upwind	Error:2.92E-01 Min:-0.001 Max:1.000 	Error:3.09E-01 Min:-0.011 Max:1.007 	Error:3.33E-01 Min:-0.028 Max:1.042 
Bounded Downwind / Van Leer	Error:3.60E-01 Min:0.000 Max:0.924 	Error:3.72E-01 Min:0.000 Max:0.903 	Error:3.85E-01 Min:-0.001 Max:0.897 
Bounded Downwind / STOIC	Error:3.35E-01 Min:0.000 Max:0.951 	Error:3.53E-01 Min:0.000 Max:0.934 	Error:3.66E-01 Min:-0.060 Max:1.047 
Bounded Downwind / MUSCL	Error:3.50E-01 Min:-0.002 Max:0.936 	Error:3.62E-01 Min:0.00 Max:0.916 	Error:3.72E-01 Min:-0.004 Max:0.913 

Figure 5.6 (continue) Comparison of different composite schemes with grids: 100*100.

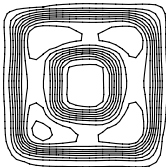
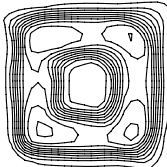
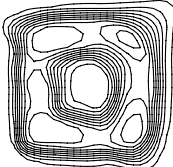
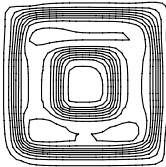
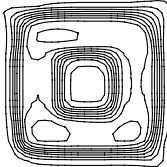
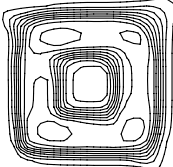
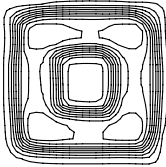
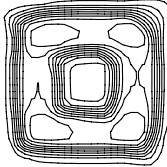
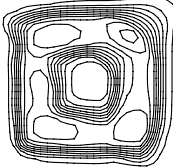
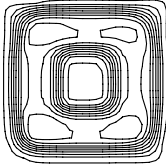
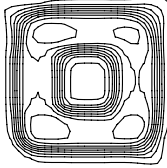
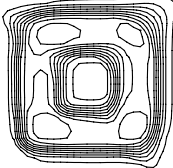
Scheme \ Co.	0.25	0.5	0.75
SUPERBEE / Cubic Upwind	Error:4.06E-01 Min: 0.000 Max:0.966 	Error:4.17E-01 Min:-0.005 Max:0.961 	Error:4.36E-01 Min:-0.026 Max:1.003 
SUPERBEE / Van Leer	Error:4.52E-01 Min:0.000 Max:0.891 	Error:4.61E-01 Min:0.000 Max:0.876 	Error:4.72E-01 Min:0.000 Max:0.868 
SUPERBEE / STOIC	Error:4.27E-01 Min:0.000 Max:0.916 	Error:4.43E-01 Min:-0.004 Max:0.922 	Error:4.57E-01 Min:-0.018 Max:0.987 
SUPERBEE / MUSCL	Error:4.43E-01 Min:0.000 Max:0.904 	Error:4.53E-01 Min:0.000 Max:0.892 	Error:4.61E-01 Min:-0.003 Max:0.894 

Figure 5.6 Comparison of different composite schemes with grids: 100*100

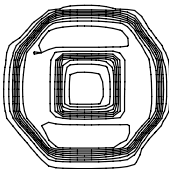
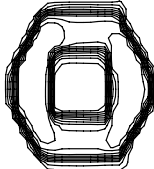
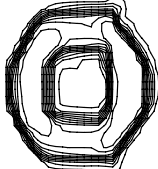
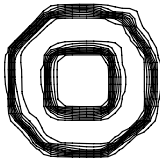
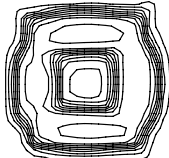
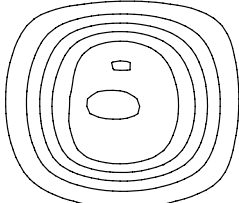
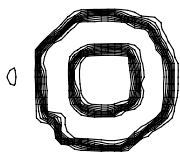
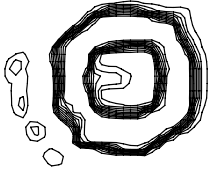
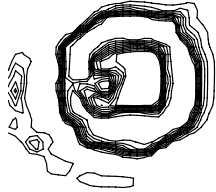
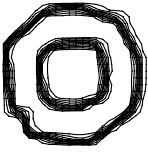
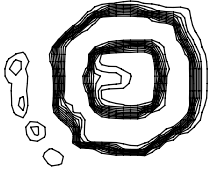
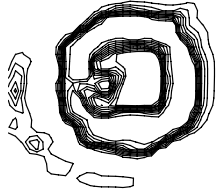
Scheme \ Co.	0.25	0.5	0.75
HRIC	Error:3.25E-01 Min:0.000 Max:0.898	Error:2.39E-01 Min:-0.096 Max:1.021	Error:2.276E-01 Min:-0.080 Max:1.088
			
	Error:1.26E-01 Min:-0.003 Max:1.002	Error:3.96E-01 Min:0.000 Max:0.876	Error:9.99E-01 Min:0.000 Max:0.553
CICSAM			
	Error:1.50E-01 Min:-0.152 Max:1.110	Error:2.667E-01 Min:-0.228 Max:1.169	Error:4.13E-01 Min:-0.334 Max:1.259
			
STACS			

Figure 5.7 Comparison of HRIC, CICSAM and STACS with grids: 100*100

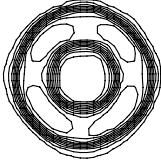
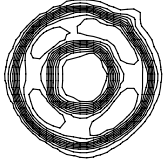
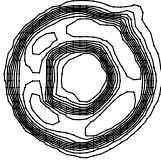
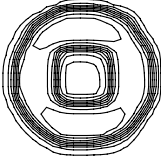
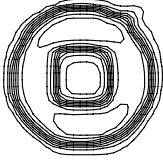
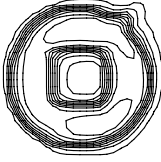
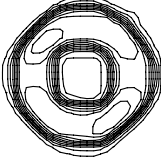
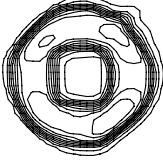
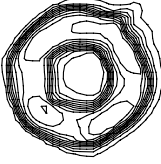
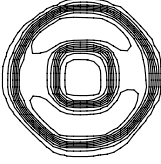
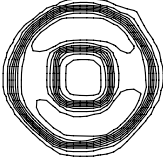
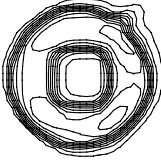
Scheme \ Co.	0.25	0.5	0.75
Bounded Downwind / Cubic Upwind	Error:1.66E-01 Min:-0.024 Max:1.016 	Error:1.95E-01 Min:-0.028 Max:1.023 	Error:2.46E-01 Min:-0.074 Max:1.041 
Bounded Downwind / Van Leer	Error:3.11E-01 Min:0.000 Max:0.907 	Error:3.25E-01 Min:0.000 Max:0.898 	Error:2.67E-01 Min:-0.002 Max:0.903 
Bounded Downwind / STOIC	Error:2.26E-01 Min:-0.003 Max:0.977 	Error:2.49E-01 Min:-0.009 Max:0.994 	Error:2.76E-01 Min:-0.060 Max:1.047 
Bounded Downwind / MUSCL	Error:2.70E-01 Min:-0.002 Max:0.936 	Error:2.82E-01 Min:-0.006 Max:0.942 	Error:2.87E-01 Min:-0.012 Max:0.972 

Figure 5.8 (continue) Comparison of different composite schemes with grids: 100*100

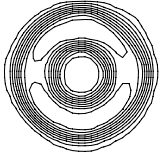
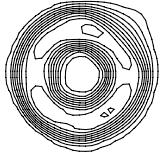
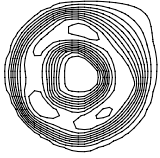
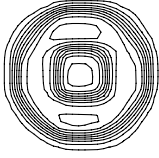


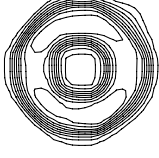
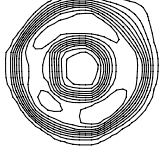
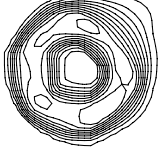
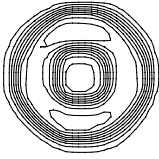
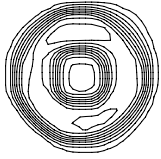
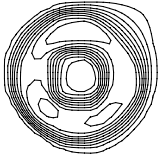
Scheme \ Co.	0.25	0.5	0.75
SUPERBEE / Cubic Upwind	Error:3.23E-01 Min:-0.009 Max:0.948 	Error:3.41E-01 Min:-0.021 Max:0.981 	Error:3.27E-01 Min:-0.041 Max:1.004 
SUPERBEE / Van Leer	Error:4.13E-01 Min:0.000 Max:0.872 	Error:4.26E-01 Min:0.000 Max:0.866 	Error:4.44E-01 Min:-0.001 Max:0.868 
SUPERBEE / STOIC	Error:3.36E-01 Min:-0.001 Max:0.920 	Error:3.64E-01 Min:-0.004 Max:0.922 	Error:3.97E-01 Min:-0.032 Max:0.992 
SUPERBEE / MUSCL	Error:3.81E-01 Min:0.000 Max:0.887 	Error:3.91E-01 Min:-0.004 Max:0.876 	Error:4.03E-01 Min:-0.007 Max:0.893 

Figure 5.8 Comparison of different composite schemes with grids: 100*100.

5.3 Surface tension

Surface tension operates at the interface and produces a force especially at sharp curvature. A numerical test illustrating this phenomenon is to apply it to an initially square bubble [32] and the surface tension force will make it change into circle. The computational domain is 1*1 and on a 30*30 uniform grids with $\Delta x = \Delta y = 0.033\text{cm}$. The time step size Δt is 0.001. A square bubble with density $\rho_1=1$, viscosity $\mu_1=1$ and surface tension $\sigma=1$ is dipped in the outer fluid which has the density $\rho_2=0.8$ and viscosity $\mu_2=0.5$.

The time evolution of the changes is shown in Figure 5.9. The relationship between grids units and vector magnitude is 1.5. To see the interface clearly, contour line sets in α equal to 0.5. The largest velocity vectors occur at the corners of the square initially. High surface tension forces produces at these positions which the curvature is maximum. The velocities pull inward on the diagonal direction and pull outward at other parts of surface. To continue, the interface overshoots the stable shape (see Figure 5.9 at $t=0.3\text{s}$) and the velocities pull outward at each original corners. This bubble does a period motion and the amplitude of oscillation will decrease as time goes by. Finally, the bubble will achieve to a stable stage.

The velocity field surrounding the interface has a low amplitude, even in the steady-state. Lafaurie et al. [37] refer to these velocities as inevitable parasite currents and presented a dimensional analysis of the viscous and surface forces reveal that:

$$K = \frac{\bar{V}_{\max} \mu}{\sigma} \quad (5.2)$$

Where K has no physical meaning, but is useful for predicting the behavior of the parasite currents. Figure 5.10 illustrates different ratio of viscosity and surface tension. The upper left panel shows the final result in the Figure 5.9. The ratio $\mu_1/\sigma=1$ holds in the case and parasite currents are visible around the interface. The next panel uses the ratio $\mu_1/\sigma=10^{-1}$ which the viscosity of fluid 1 is ten times higher surface tension coefficient. The velocity vectors are ten times size of the original vectors. The lower left panel presents the ratio $\mu_1/\sigma=10$. The velocity vectors for this case almost vanish. The last panel shows the results obtained with both the surface tension coefficient and viscosity 10 times than the original values, resulting

in ratio of $\mu/\sigma=1$. The magnitude of the velocity vectors are the same with the first panel.

Hence, these parasite currents increase with decreasing viscosity and increasing surface tension.

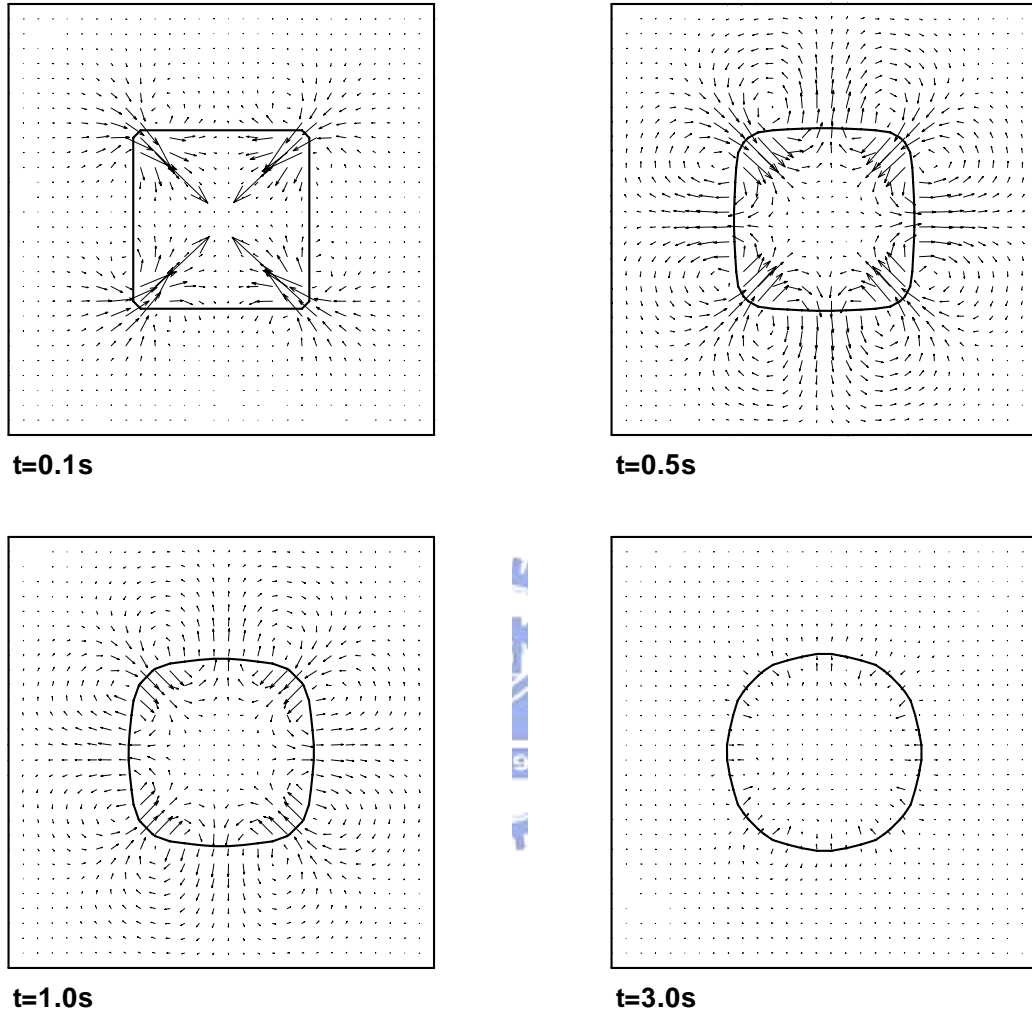
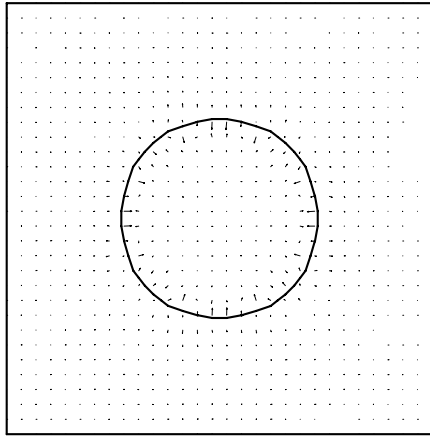
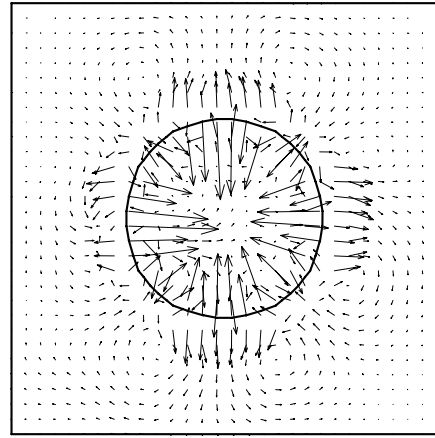


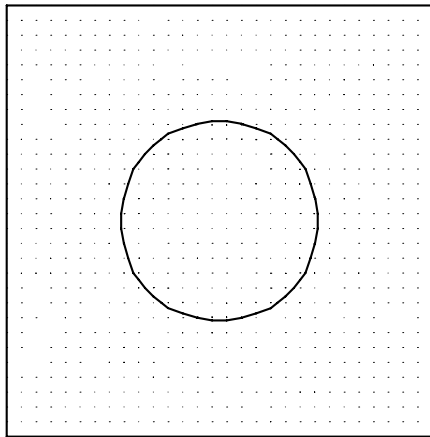
Figure 5.9 Time evolution of the shape changes of a square subjected to surface tension forces.



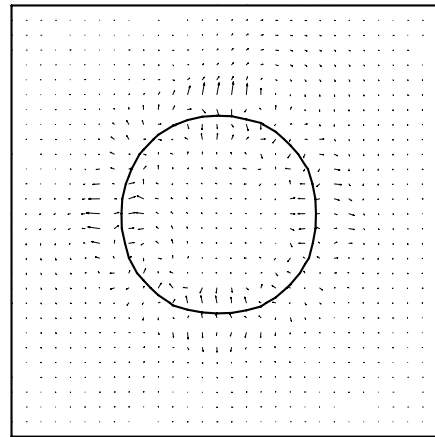
$$\mu_1=1, \sigma=1, \rho_1/\sigma=1$$



$$\mu_1=1, \sigma=10, \rho_1/\sigma=10^{-1}$$



$$\mu_1=1, \sigma=10^{-1}, \rho_1/\sigma=10$$



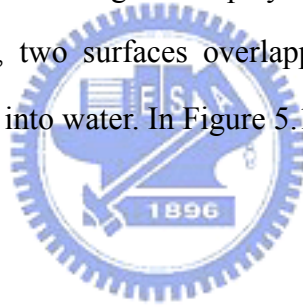
$$\mu_1=10, \sigma=10, \rho_1/\sigma=1$$

Figure 5.10 Parasite currents for different viscosity of fluid 1 and surface tension coefficient.

5.4 Drop splash

A water droplet falling through air onto water surface is considered by Puckett et al.[38] The computational domain is $0.007\text{m} \times 0.014\text{m}$ with grids of 64×128 . The viscosity of air is $1.77625 \times 10^{-5} \text{ kg/m s}$ and the density is 1.225 kg/m^3 . For water the viscosity is $1.1377 \times 10^{-3} \text{ kg/m s}$ and the density is 999.2 kg/m^3 . The center of water droplet is at $(0.0035, 0.0106)\text{m}$ and the diameter is 0.0089m . Gravity is considered here ($g=9.8 \text{ m/s}^2$) and surface tension is neglect. Figure 5.11 shows the numerical simulation by Puckett et al.

This example demonstrates the merging of two independent regions. Because the droplet is fairly close to the water surface some air bubbles are trapped in the water after splash. Water waves is results from the splash moving toward the walls. Figure 5.12 shows our numerical results. Both lines and contours are shown. Contours are displayed for $0.4 \leq \alpha \leq 0.6$ with a step size 0.02 and the colored regions display for α greater than 0.4. In the third panel ($t=0.00980\text{s}$) of Figure 5.12, two surfaces overlapped. There are too much residual air bubbles after the droplet fallen into water. In Figure 5.13 shows a much reasonable results.



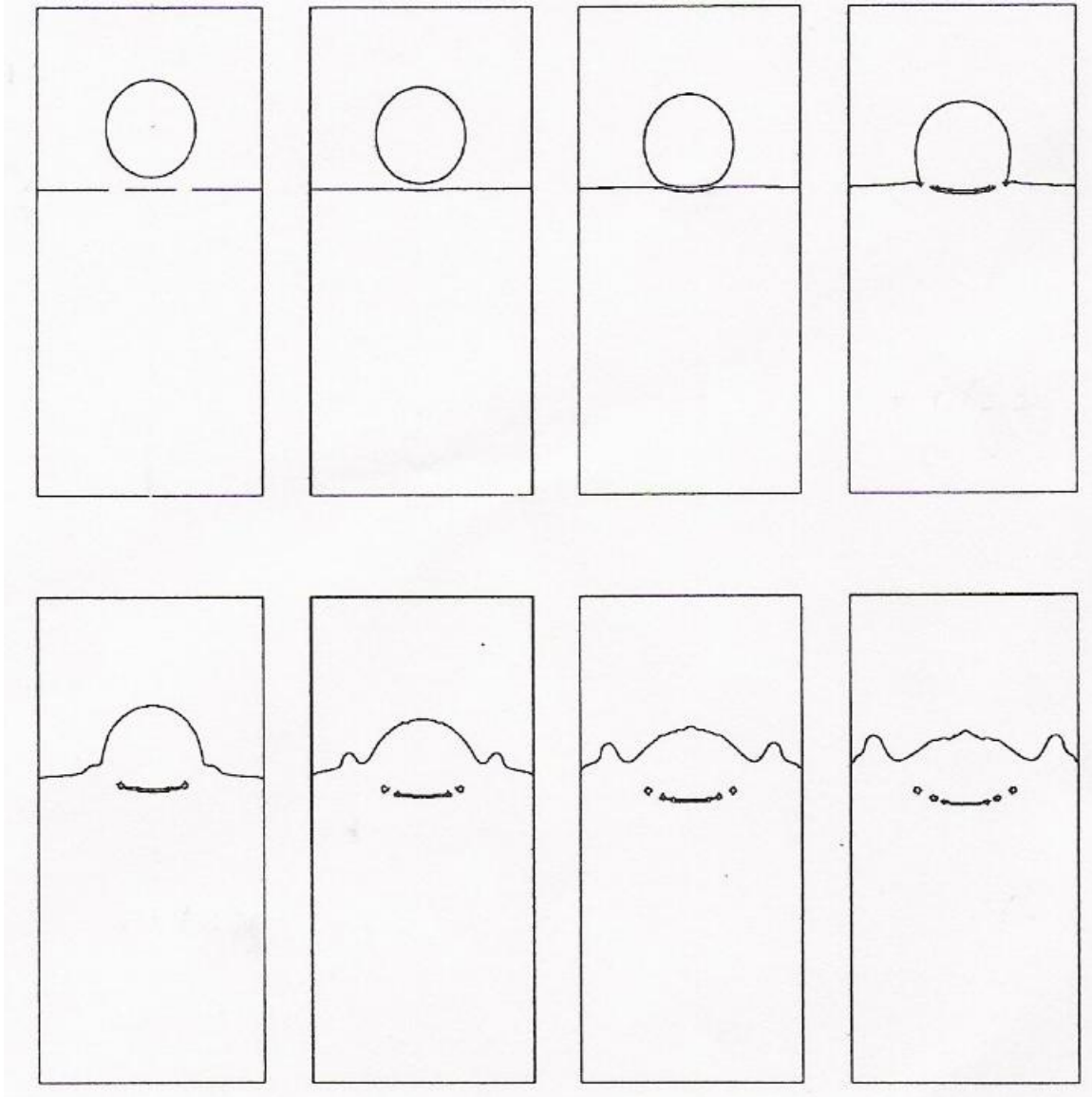


Figure 5.11 the water droplet falling air onto surface at times $t=0.0s, 0.00677s, 0.00980s, 0.01220s, 0.01485s, 0.01781s, 0.01995s, 0.02146s$.(by Puckett et al. [38])

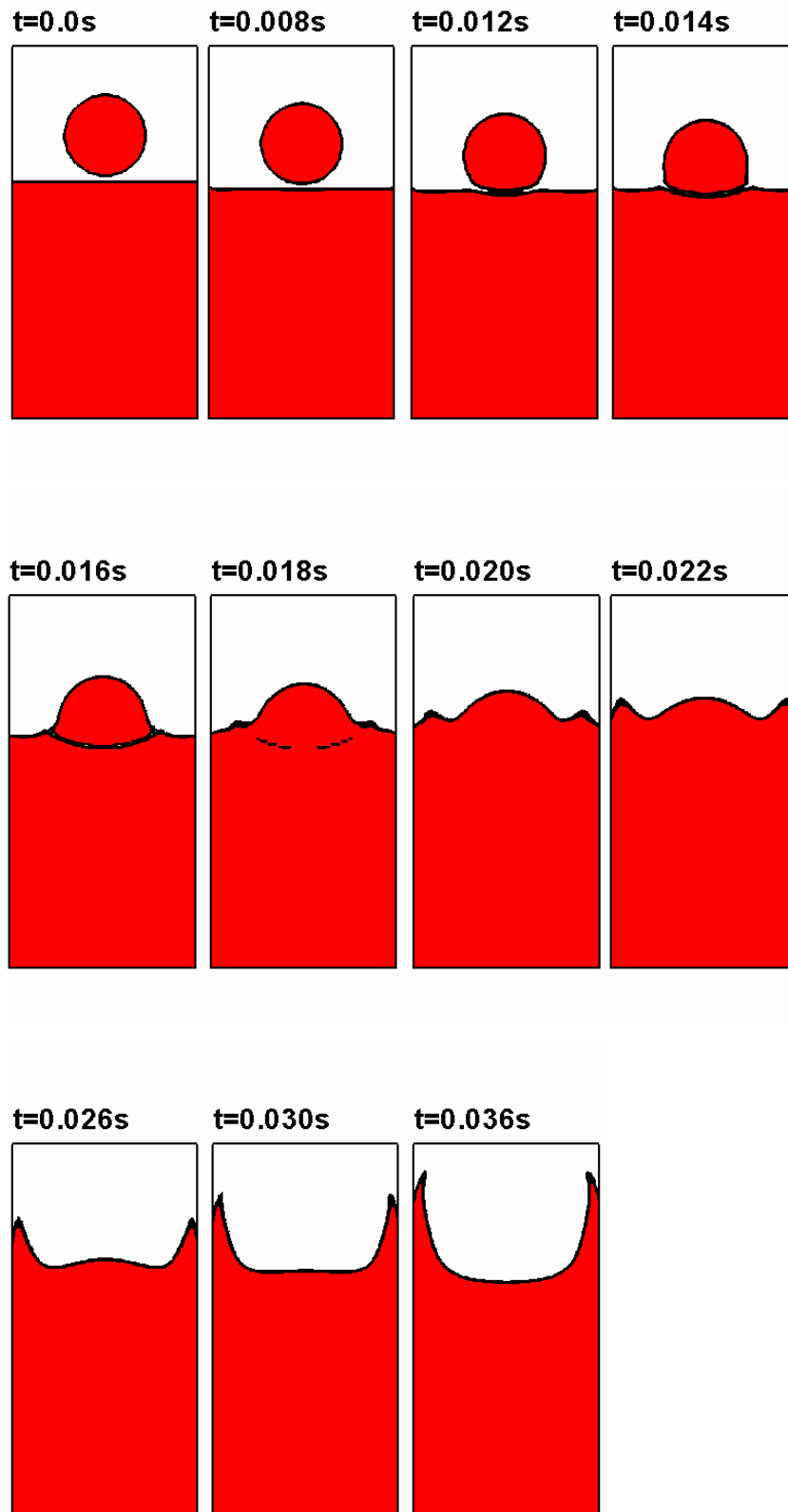


Figure 5.12 Water droplet falling through air onto water surface. The time step size is 0.00005 and computational domain is $0.007 \times 0.014 (64 \times 128)$. The maximum Courant number during computation is 0.24

5.5 Bubble

A simple example referred by Puckett [38] is another air/water computation with the same computational domain, contour settings and resolution as the previous example. In this case, the initial condition is an air bubble which size is the same with the droplet in the last example. Figure 5.13 shows time evolution of the numerical results. The air bubble will rise through water as time goes by. At first, the air bubble is compressed as an ellipse. The lower edge of the bubble accelerates more quickly than the upper edge. As the bubble continues to rise the center of bubble is stretched until the bubble breaks. Then, the sides of bubble stretched and the lower parts of each bubble form a new small air bubble. Finally, the upper two bubbles attach and become two strips which are rising. The lower two bubbles are still breaking.

Figure 5.14 illustrates motion of bubble with surface tension and this case has no related experiment and numerical studies. It is apparent that the air bubble rises faster than the case without surface tension force. At first, the air bubble is compressed by vertical forces and transforms into an elliptic. Then, this elliptic bubble is influenced by the reacting forces and returns to a circle until attaches the upper boundary. The air bubble is divided into two small parts and then they will pull back by surface tension force.

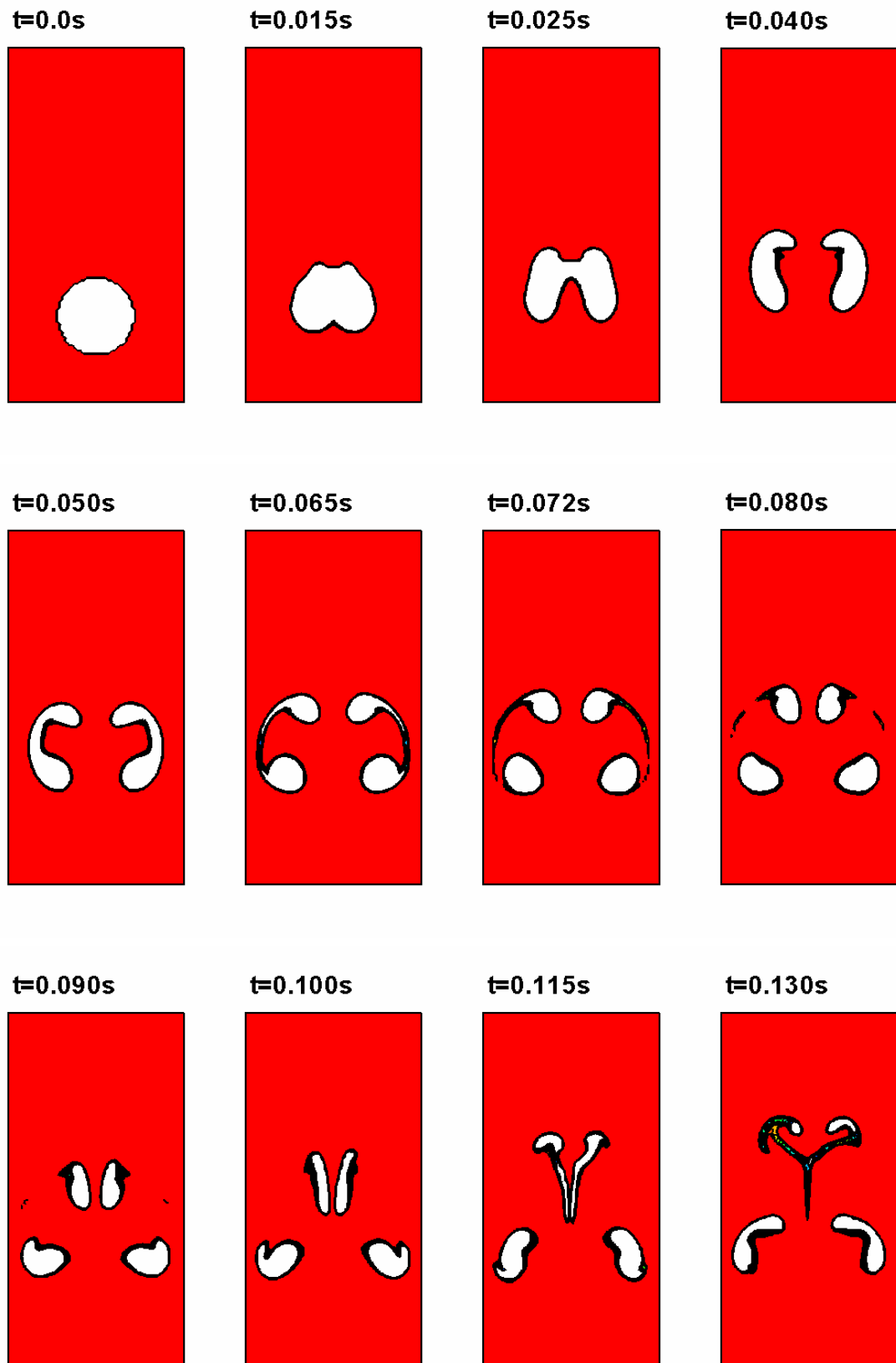


Figure 5.13 Time evolution of an air bubble rising through water without surface tension.

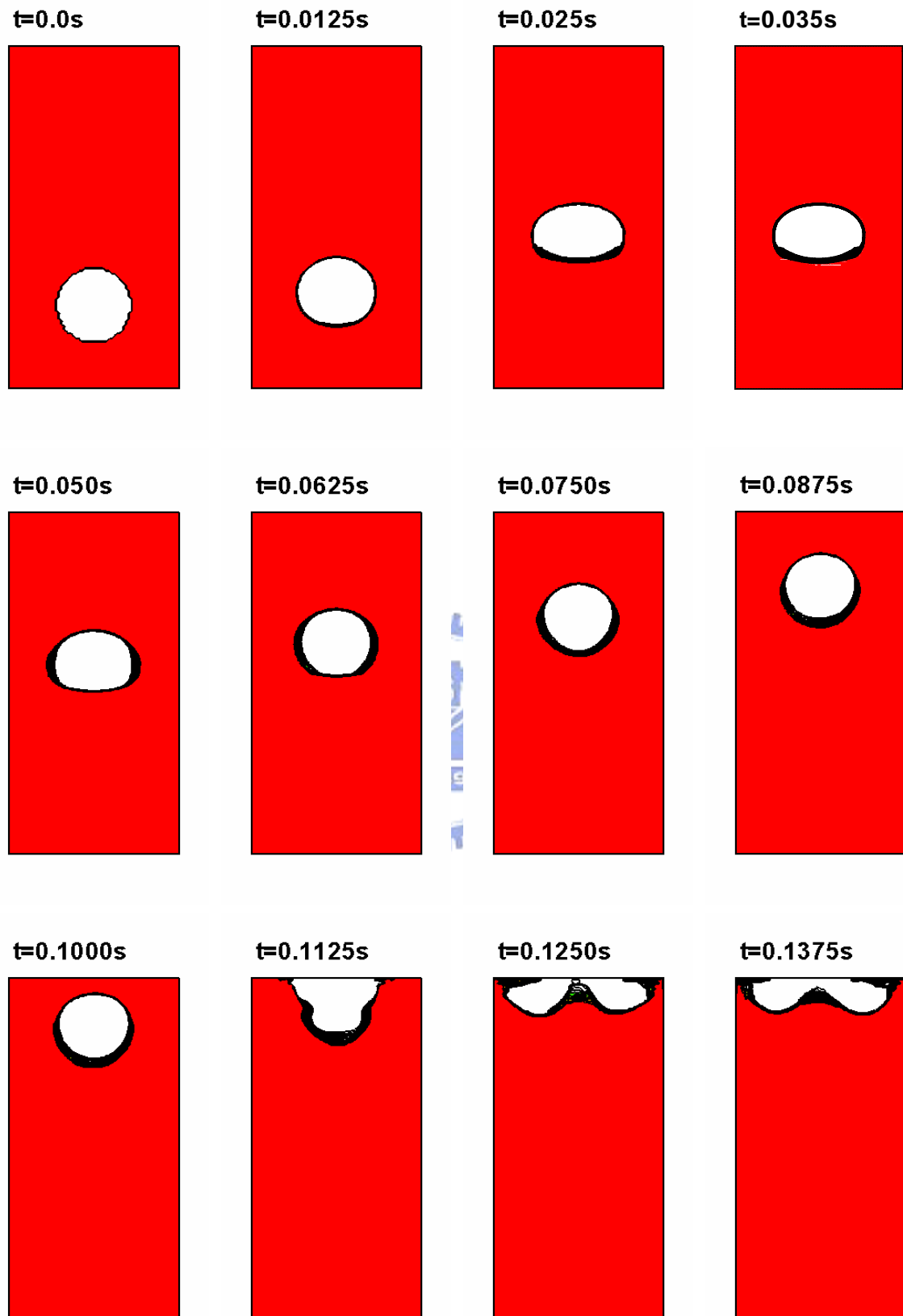


Figure 5.14 Time evolution of an air bubble rising through water with surface tension.

5.6 Sloshing

The sloshing of a liquid wave with a low amplitude under the influence of gravity are tested by Raad et al. [39] and Ubbink [30]. Initially, the quiescent fluid has an average depth of 0.05m, and its surface is defined by half of a cosine wave with an amplitude of 0.005m. The computational domain has a base width of 0.1m and a height of 0.065m. Its bottom and sides are treated as slip boundaries and at top the open boundary condition is applies. The viscosity of both fluid is taken as zero and the densities are defined as $\rho_1=1000$ and $\rho_2=1$. Figure 5.15 shows the physical model of this example.

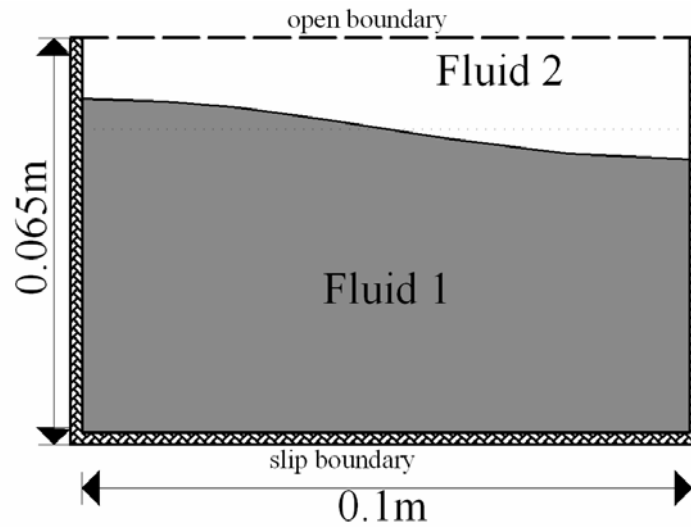


Figure 5.15 The physical model of sloshing.

Raad et al. presented the numerical result by using Mark and Cell (MAC) method for an effective uniform mesh resolution of 80 cells in horizontal and 52 cells in vertical. For the study of Ubbink, CICSAM scheme is adopted, and a uniform mesh with 160 cells in horizontal and 104 cells in vertical. The sloshing case is useful for evaluating the CFD methodology with respect to two different phenomena present in the numerical prediction of interfacial flow, namely [30]:

- The numerical dissipation introduced by the discretization and
- The ability to conservatively transfer potential energy into kinetic energy and vice versa.

The fluid begins to slosh under the influence of a constant gravity 9.8m/s^2 in the downward vertical direction. The theoretical period of sloshing is [39]:

$$P = 2\pi\sqrt{gk \tanh(kh)} = 0.3739 \quad (5.3)$$

where k is the wave number and h is the average fluid depth.

The time evolutions of sloshing are shown in Figure 5.16 and the contour is $0.4 \leq \alpha \leq 0.6$ with 11 levels. The whole system is rest initially. After a quarter of period, the sloshing goes into a horizontal level and the potential energy transfers into kinetic energy. After a half of period, all the potential has transferred into kinetic energy and the kinetic energy starts transfer back into potential energy. The wave backs to its original position after one period. Figure 5.17 shows the wave position for the first ten periods.

Raad et al. [39] used two norms, the temporal error and the root mean square (RMS) spatial error for assessing accuracy. The temporal error is defined as:

$$100 \frac{(t_c - t_t)}{t_t} \quad (5.4)$$

where t_c and t_t represent the calculated and theoretical time respectively. The calculated time is taken as the time when the interface reaches its highest point against the left boundary, and the theoretical time is the period of sloshing multiplied by the amount of periods.

The RMS spatial error is defined as:

$$\frac{100}{a\sqrt{M}} \left[\sum_{m=1}^M (y_c - y_t)^2 \right]^{\frac{1}{2}} \quad (5.4)$$

where m is the cell counter in the horizontal direction, M the number of cells in horizontal direction, a the wave amplitude, y_c the predicted interface height and y_t the theoretical height.

In this study, the sloshing are tested in two kind of mesh configuration (160*104 and 80*52).

The following table shows the temporal error and spatial error compared with the studies of Raad et al. and Ubbink.

Theoretical time	Temporal error(%)				Spatial error(%)			
	Raad et al.	CICSAM (by Ubbink)	SUPERBEE +MUSCL 160*104	SUPERBEE +MUSCL 80*52	Raad et al.	CICSAM (by Ubbink)	SUPERBEE +MUSCL 160*104	SUPERBEE +MUSCL 80*52
2P	-0.44	0.0	0.147	1.343	2.0	1.9	0.104	0.524
4P	-0.39	-0.75	0.106	0.310	2.8	2.0	0.077	0.576
6P	-0.29	0.04	0.271	0.450	3.5	3.7	0.240	0.404
8P	*	*	0.310	0.452	*	*	0.678	0.690
10P	*	*	0.307	0.441	*	*	0.895	0.916

Table 5.1 Comparison of temporal and spatial errors

Figure 5.18 shows the amplitude of sloshing of the viscous flow. The boundary conditions at bottom and sides are treated as non-slip boundaries. The viscosity of fluid 1 is 0.01 and fluid 2 is 0.001. The decay of sloshing amplitude in the coarse mesh (80*52) is slower than finer mesh (160*104).



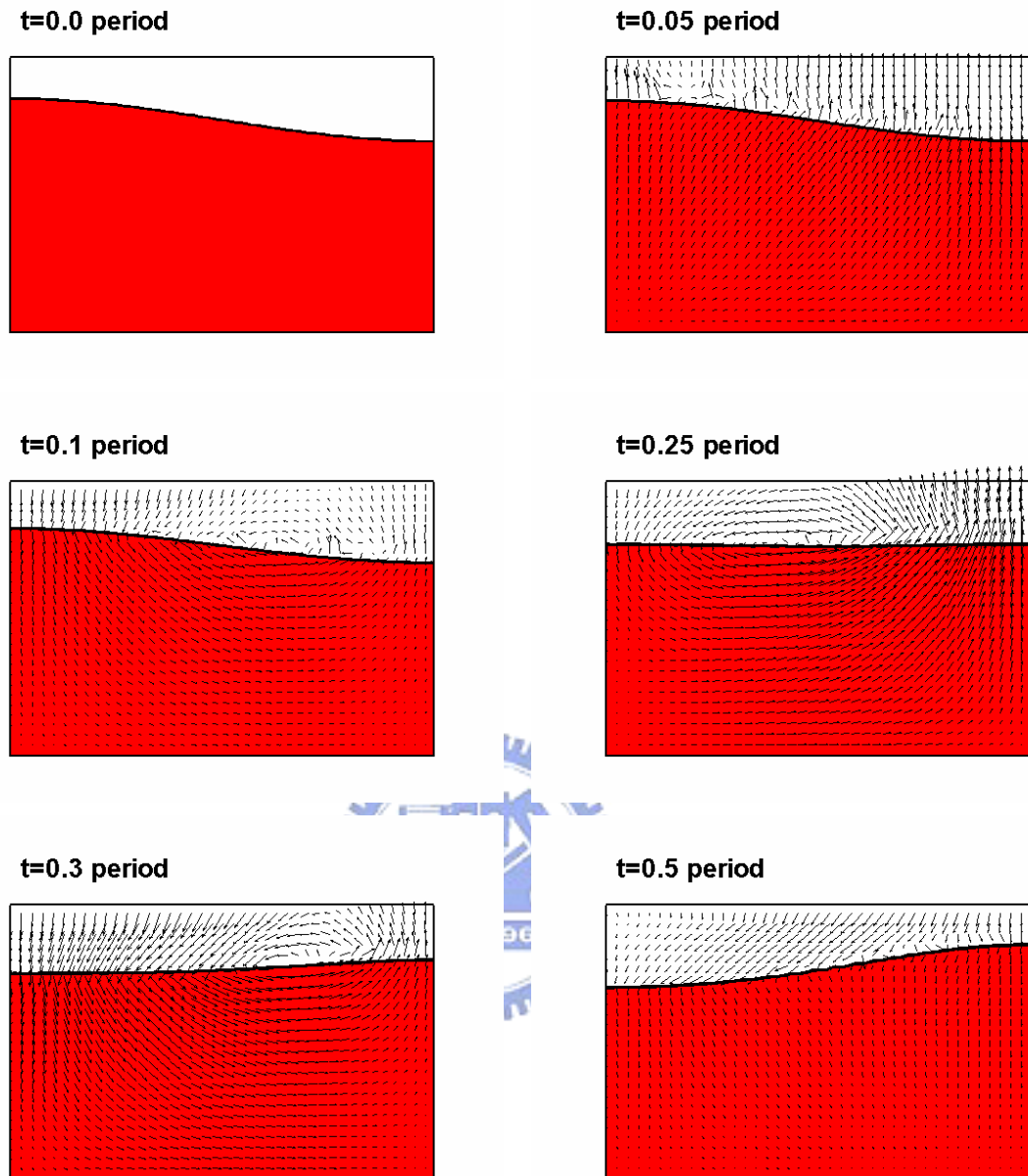


Figure 5.16 Time evolution of the wave position and velocity vectors for the first period of sloshing of an inviscid flow field which influenced by gravity. The computational grids are 160*104. The maximum Courant number during the computation: 0.03 (continue)

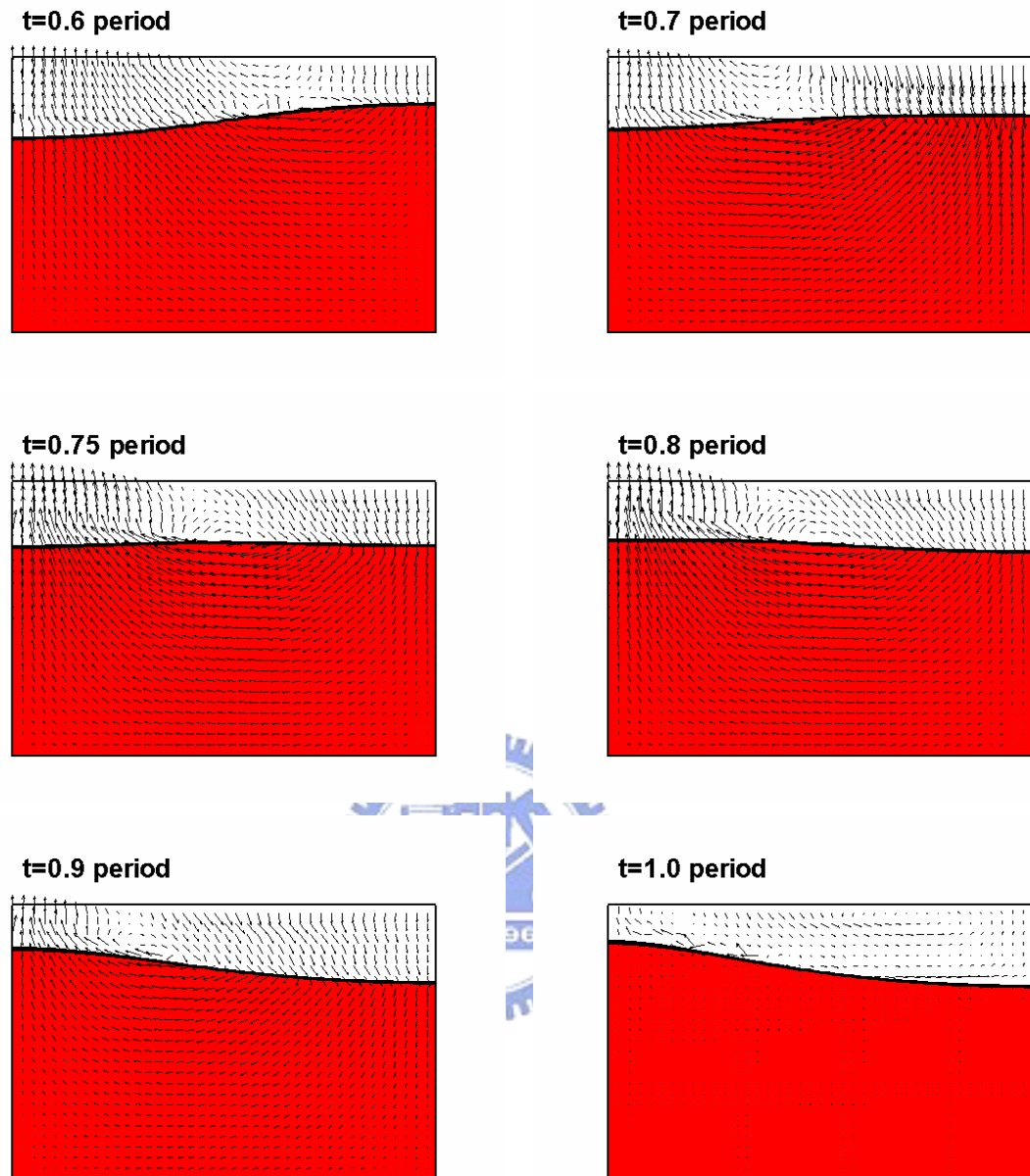


Figure 5.16 Time evolution of the wave position and velocity vectors for the first period of sloshing of an inviscid flow field which influenced by gravity. The computational grids are 160×104 . The maximum Courant number during the computation: 0.03

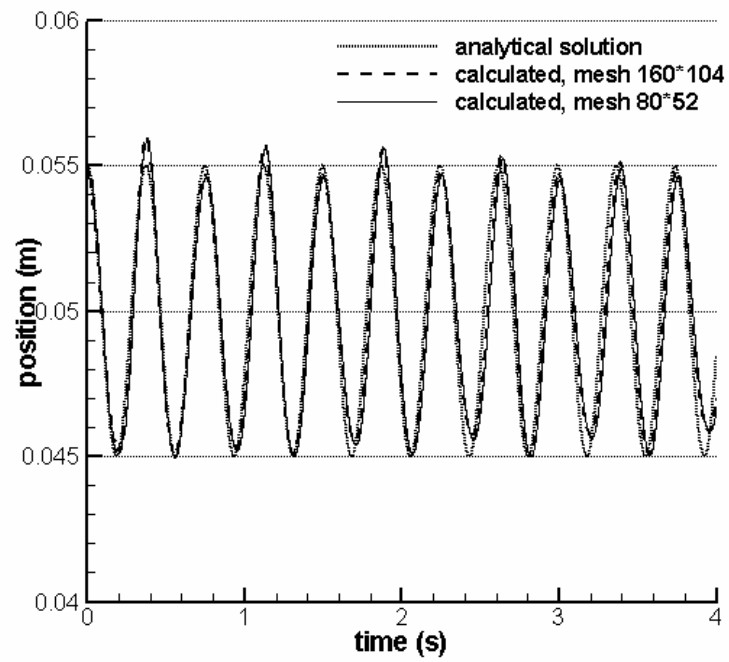


Figure 5.17 Position of the interface at the left boundary against the time (inviscid flow).

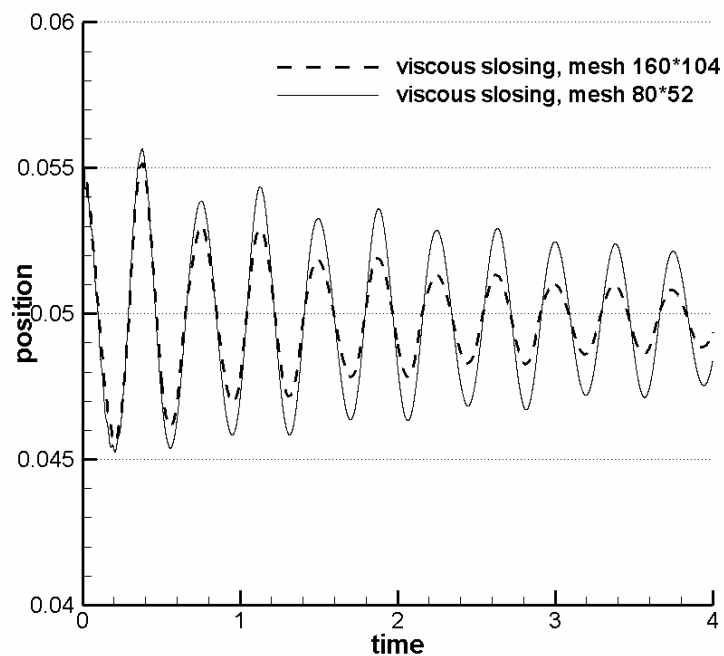


Figure 5.18 Position of the interface at the left boundary against the time (viscous flow).

The amplitude of sloshing will decrease with the time goes by.

5.7 Rayleigh-Taylor instability

Rayleigh-Taylor instability [18] is a good example to test the effect of VOF and momentum transport. Initially the velocity field is rest and this example is density-driven. Gravity dominates the whole flow field. Figure 5.19(a) shows the physical model of this example. The computational domain is 1.0×3.0 . Initially the top one-third of the domain is filled with fluid of density $\rho_1=1.2$ ($\alpha=1.0$) and the lower two-third is filled with fluid of density $\rho_2=1.0$ ($\alpha=0.0$). All boundaries are walls and use non-slip boundary condition. The Froude number ($Fr = U / \sqrt{gL}$) is 0.5 and Reynold number ($Re = \rho UL / \mu$) is 500. The interface between two fluids is defined by half of a cosine wave with amplitude of 0.02m. In this study, there are two types of grid arrangements will be tested. The first is uniform grids with 64 cells in horizontal and 192 cell in vertical (see Figure 5.19(b)). The second is non-uniform grids with 80 cells in horizontal and 284 cells in vertical (see Figure 5.19(c)).

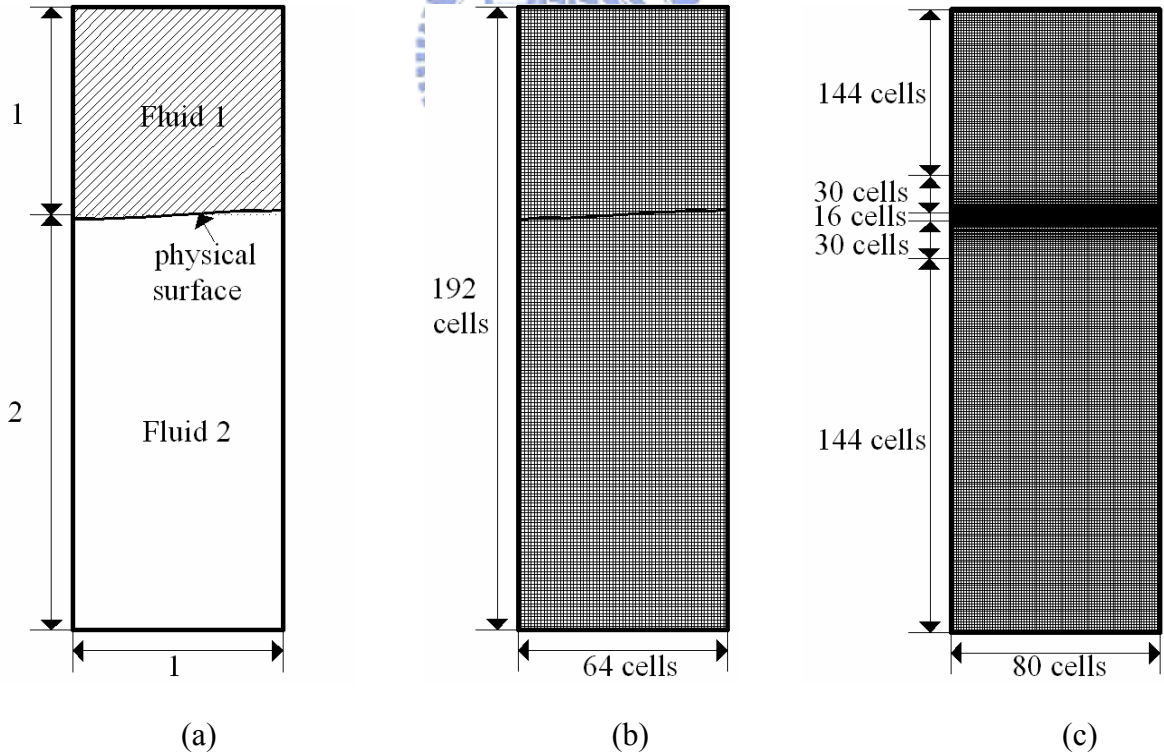
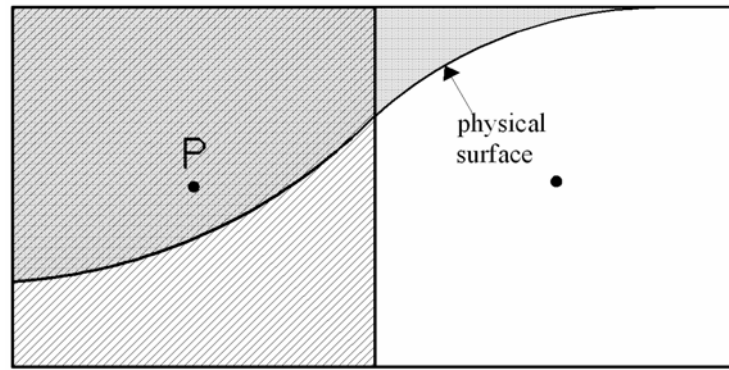


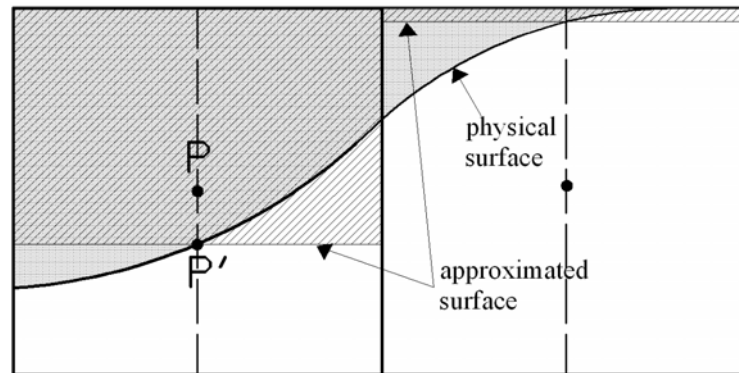
Figure 5.19(a) The physical model of Rayleigh-Taylor instability. (b) The arrangement of uniform grids (64*192). (c) The arrangement of non-uniform grids (80*284)

Because this example is unstable and could be influenced by perturbation easily, different settings of initial condition are adopted. The following details five kinds of initial settings:

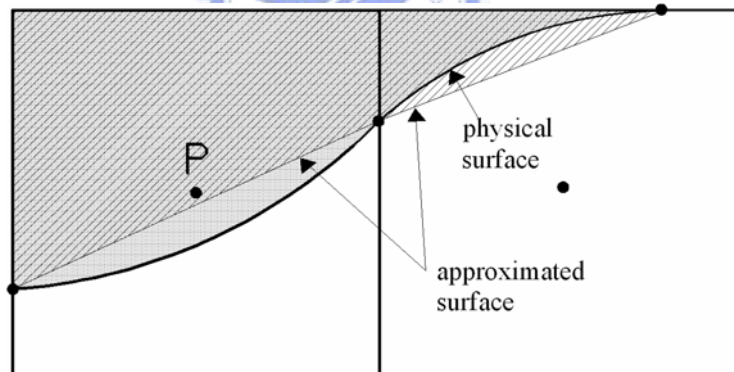
- ♦ 1st: The volume fraction value at each cell center α_p is determined by the height of cell center position directly, i.e. if the cell center is higher than the physical surface, α_p is equal to unity (see Figure 5.20(a)).
- ♦ 2nd: Extend a vertical line which pass through the cell center P, an approximated point P' can be obtained by the line intersecting the physical surface. An approximated surface can be obtained and introduces an area (see the hatched area in Figure 5.20(b)). Then, the α_p can be approximated.
- ♦ 3rd: In the interface region, interface intersects two points at cell faces and connects these two points by a straight line, a trigonometry or a quadrilateral will be obtained. Hence, α_p can be determined by the portion of the approximated area (see the hatched area in Figure 5.20(c))
- ♦ 4th: The second kind of initial condition is adopted for $x < 0.5$ and the third kind of initial condition is used for $x > 0.5$.
- ♦ 5th: The second kind of initial condition is used for $x > 0.5$ and the third kind is chose for $x < 0.5$ for the fifth kind of initial condition.



(a)



(b)



(c)

Figure 5.20 (a) The first kind of initial condition. (b) The second kind of initial condition (c) The third kind of initial condition.

The time evolutions are shown in Figure 5.21 to 5.30. As time goes by, the leftist and rightist point at interface are nearly fixed. It is surprising that the results of each initial condition are not very different.

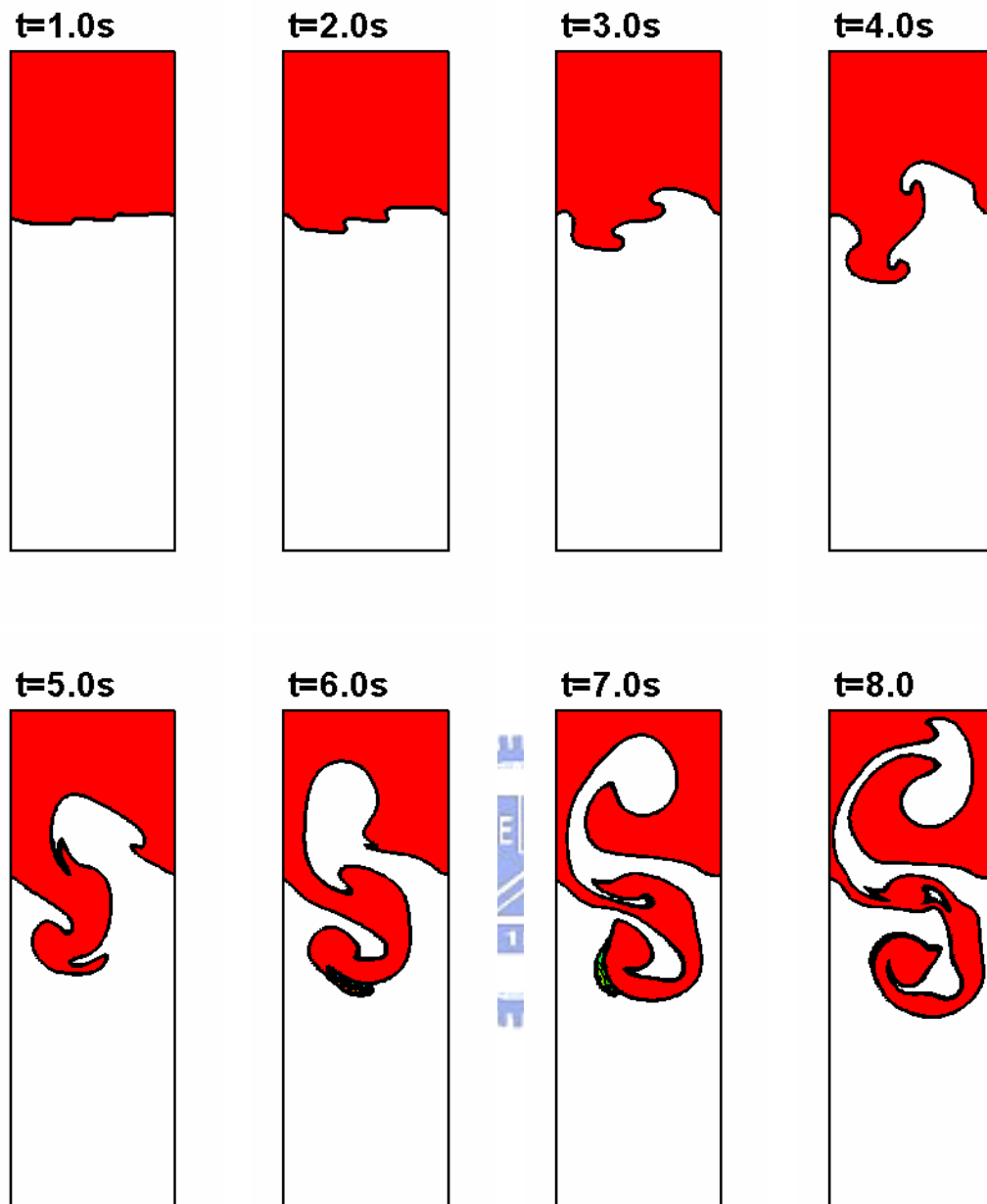


Figure 5.21 The numerical results of Rayleigh-Taylor instability adopting 1st kind of initial condition with uniform grids 64×192 .

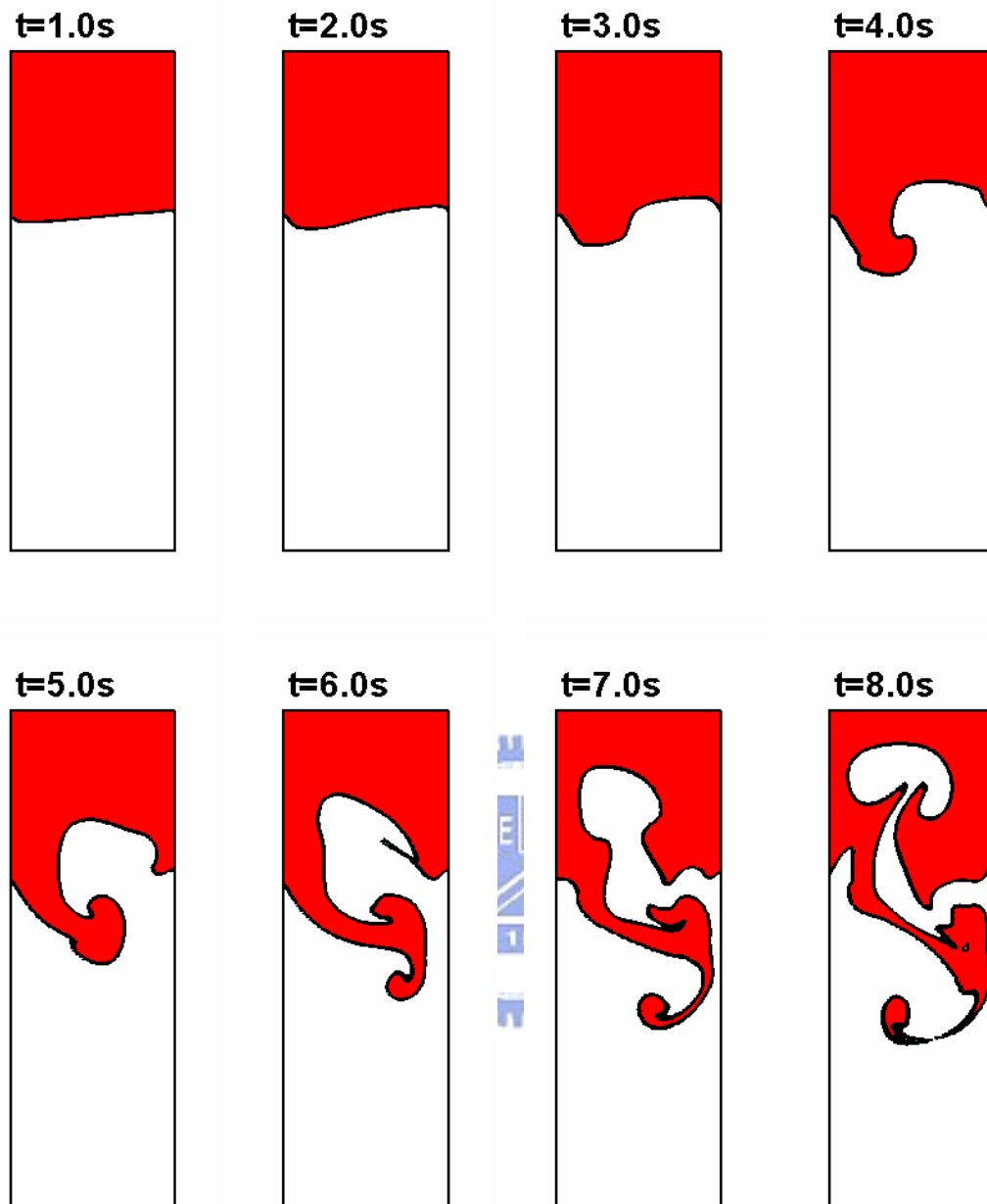


Figure 5.22 The numerical results of Rayleigh-Taylor instability adopting 1st kind of initial condition with non-uniform grids 80*284.

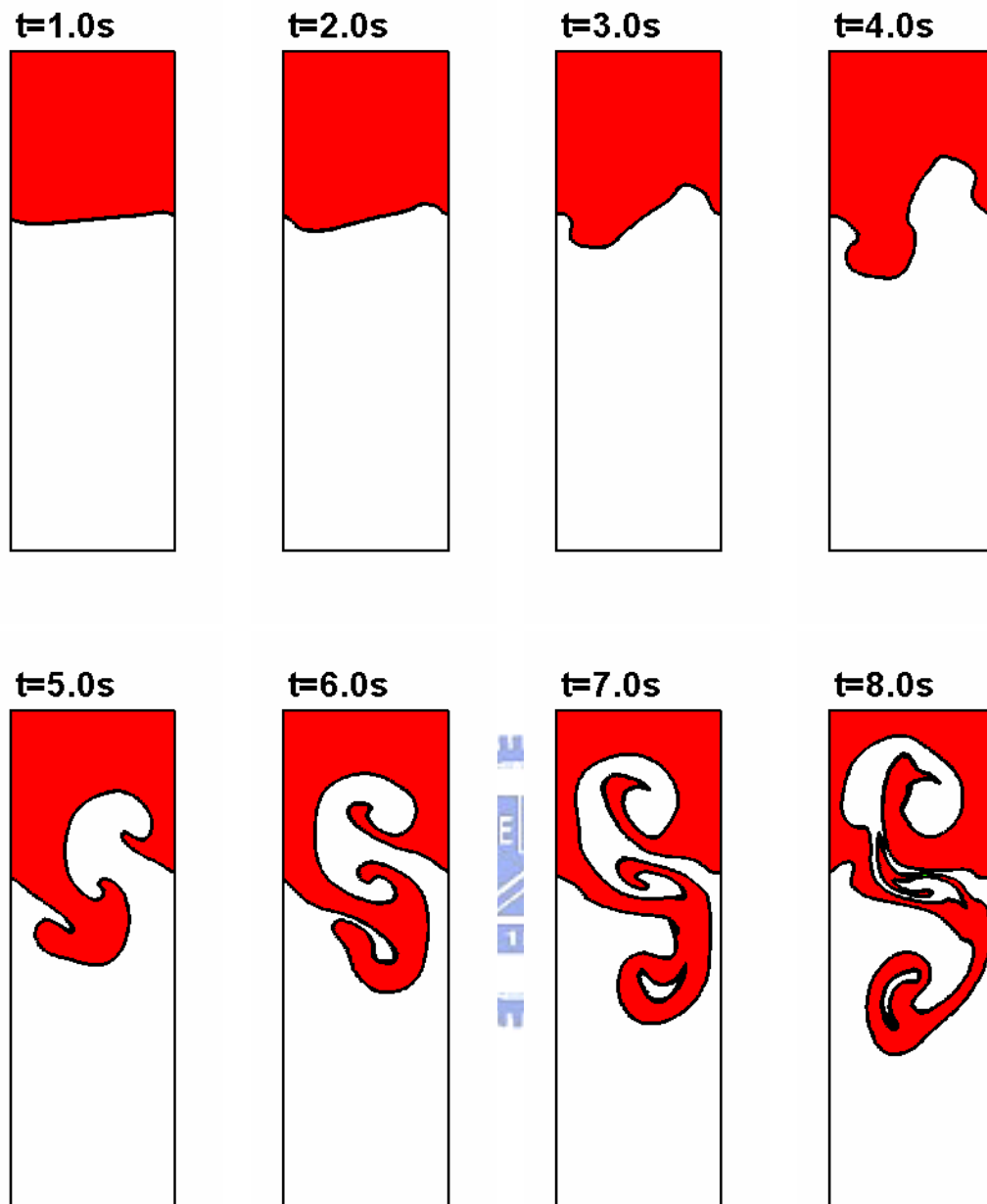


Figure 5.23 The numerical results of Rayleigh-Taylor instability adopting 2nd kind of initial condition with uniform grids 64×192 .

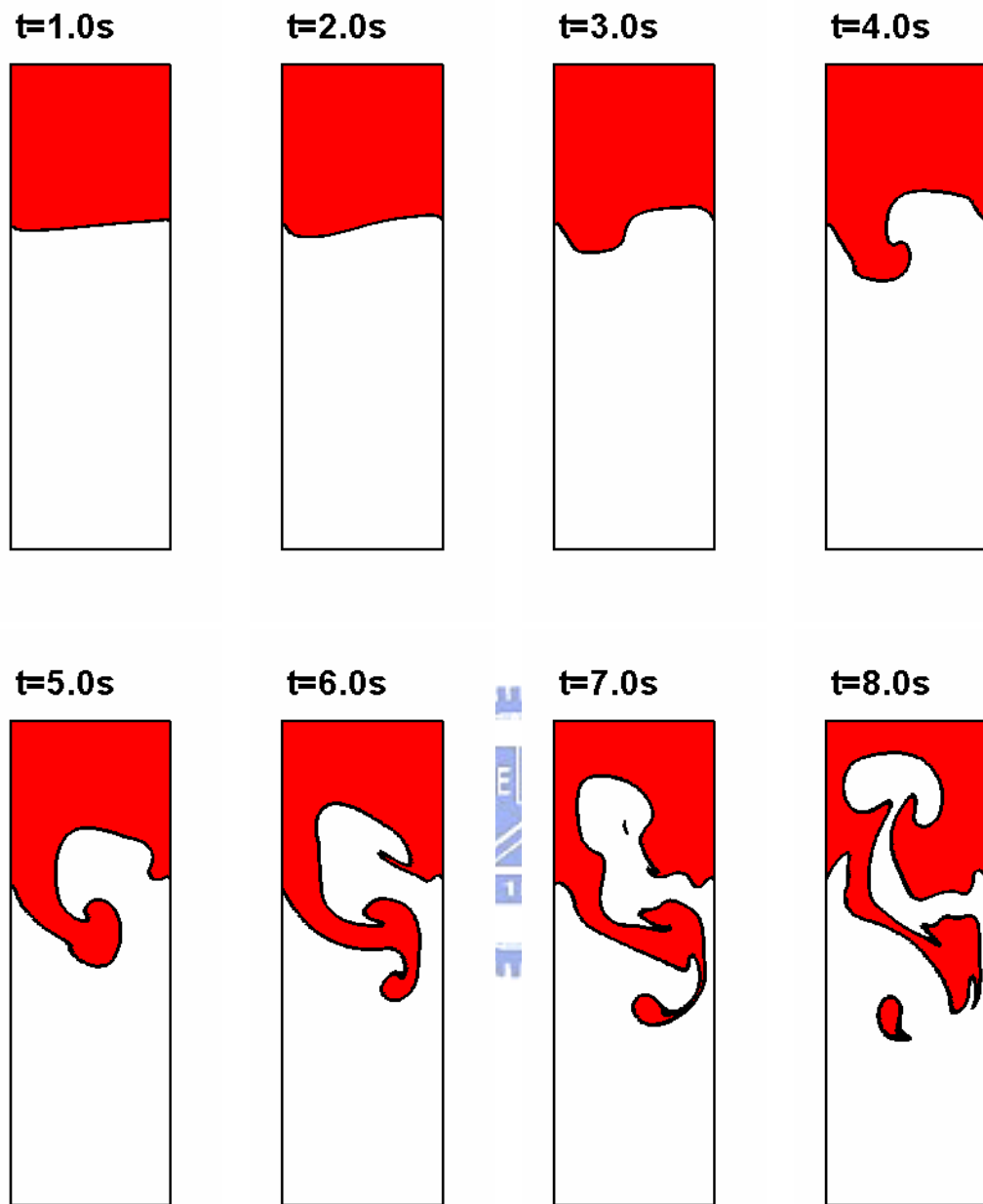


Figure 5.24 The numerical results of Rayleigh-Taylor instability adopting 2nd kind of initial condition with non-uniform grids 80*284.

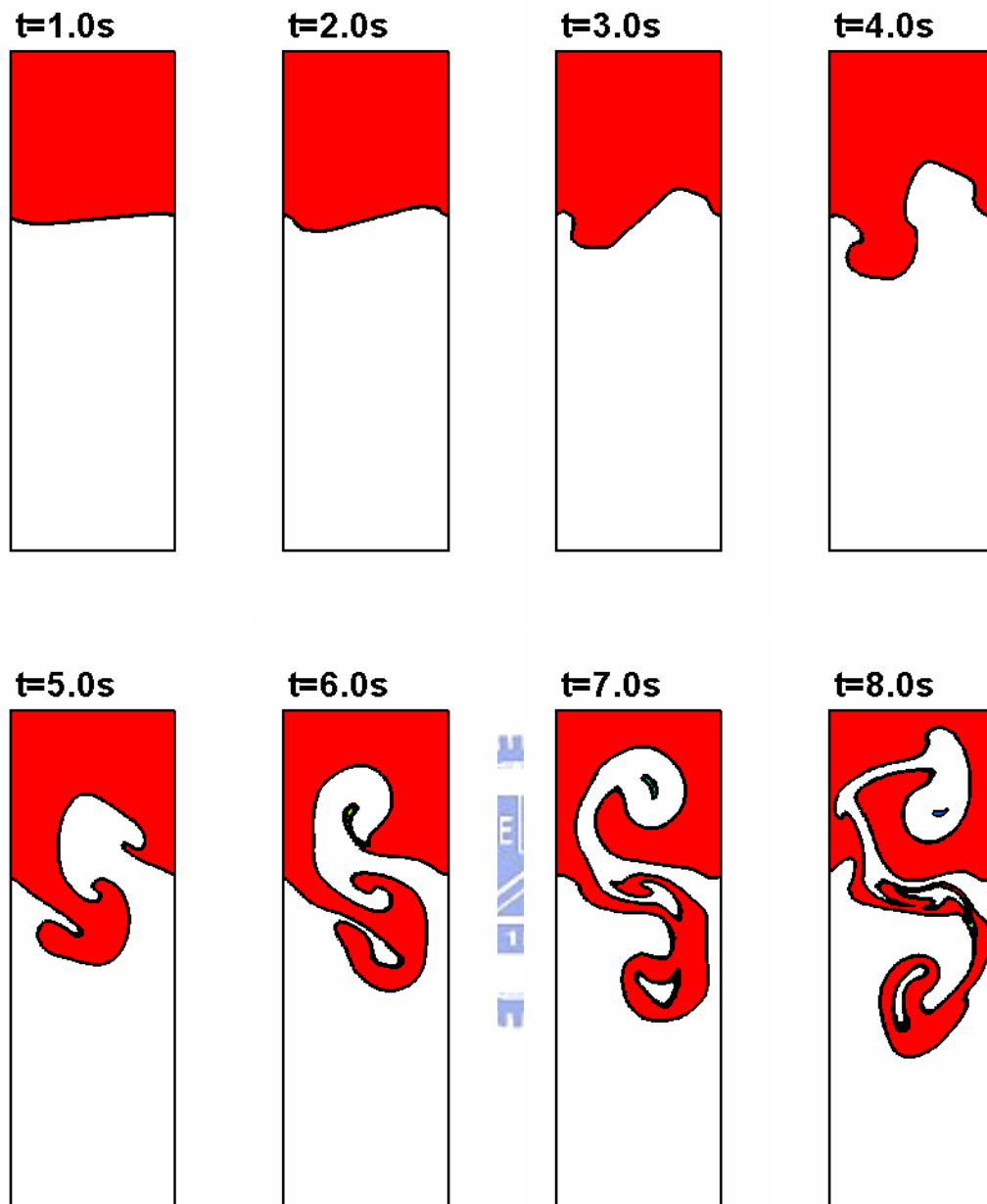


Figure 5.25 The numerical results of Rayleigh-Taylor instability adopt 3rd initial condition with uniform grids 64×192 .

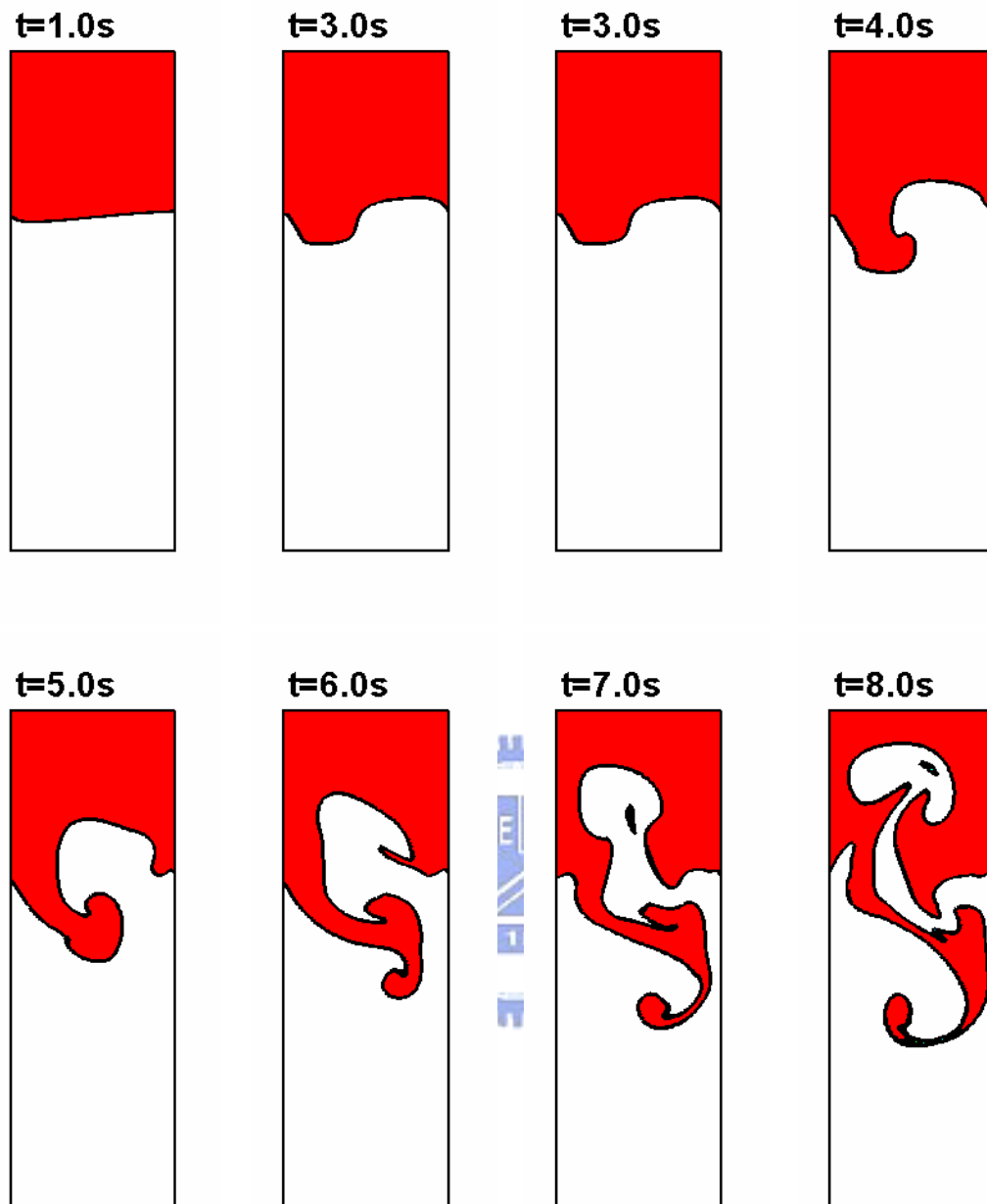


Figure 5.26 The numerical results of Rayleigh-Taylor instability adopting 3rd kind of initial condition with non-uniform grids 80*284.

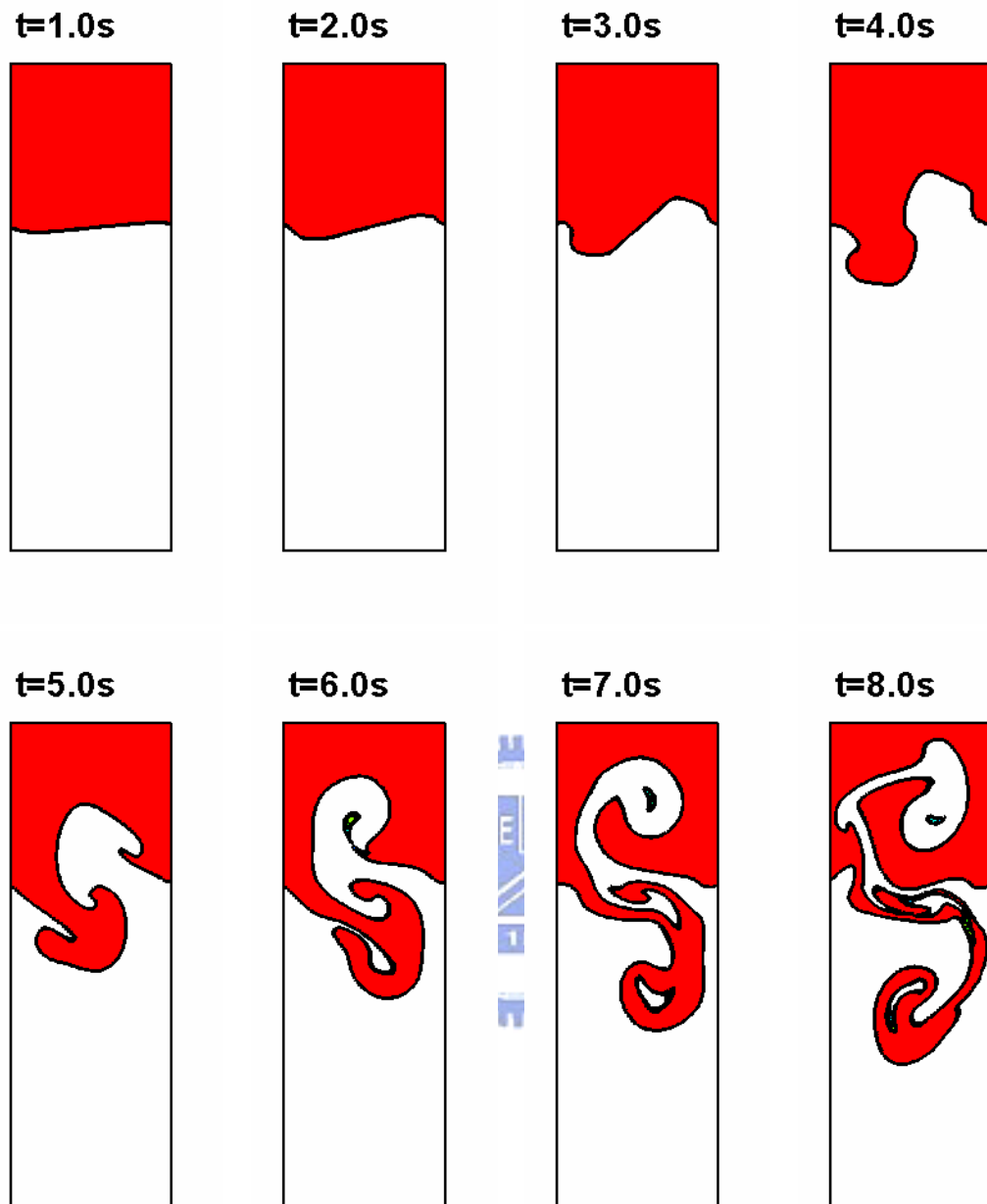


Figure 5.27 The numerical results of Rayleigh-Taylor instability adopting 4th kind of initial condition with uniform grids 64*192.

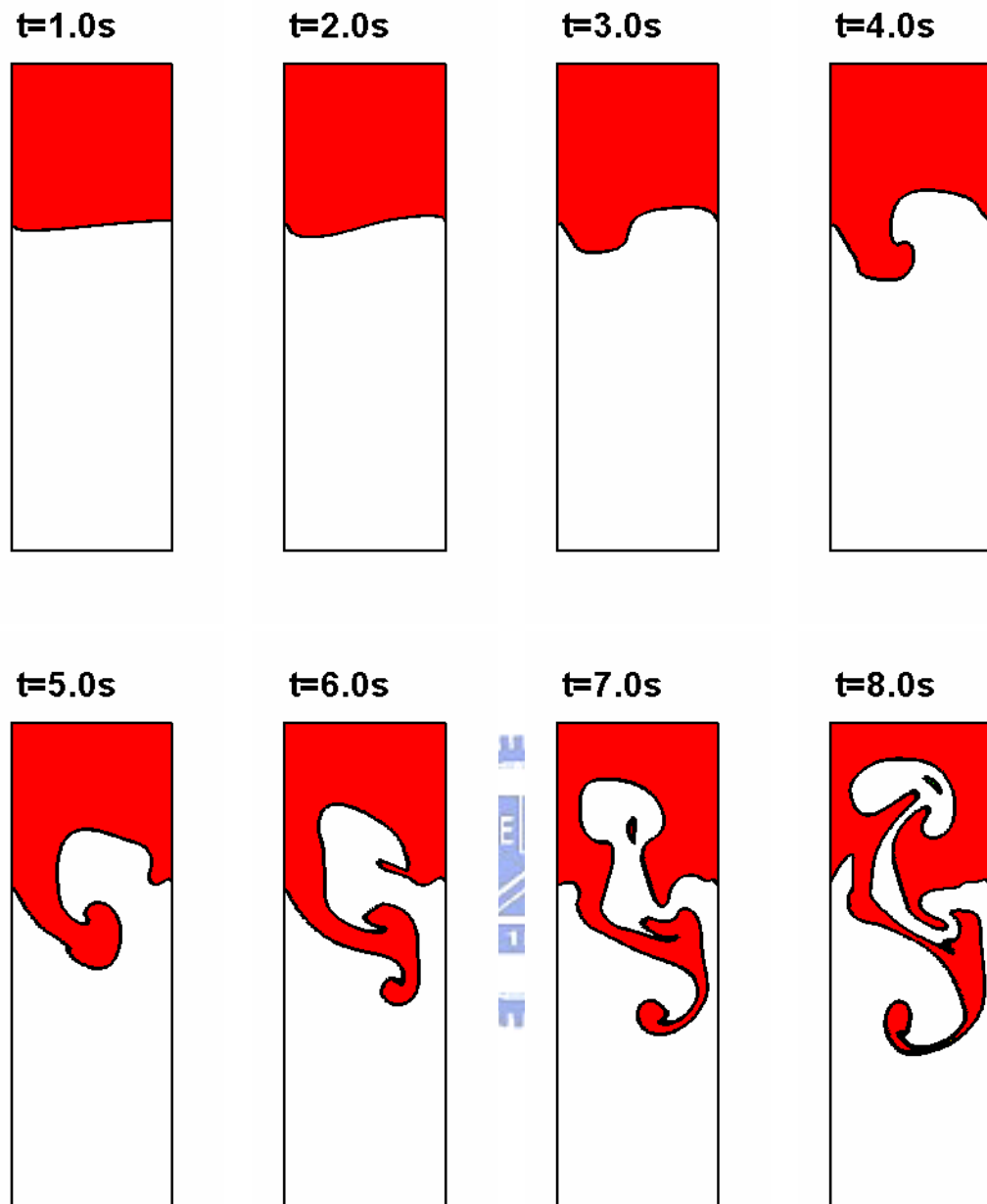


Figure 5.28 The numerical results of Rayleigh-Taylor instability adopting 4th kind of initial condition with non-uniform grids 80*284.

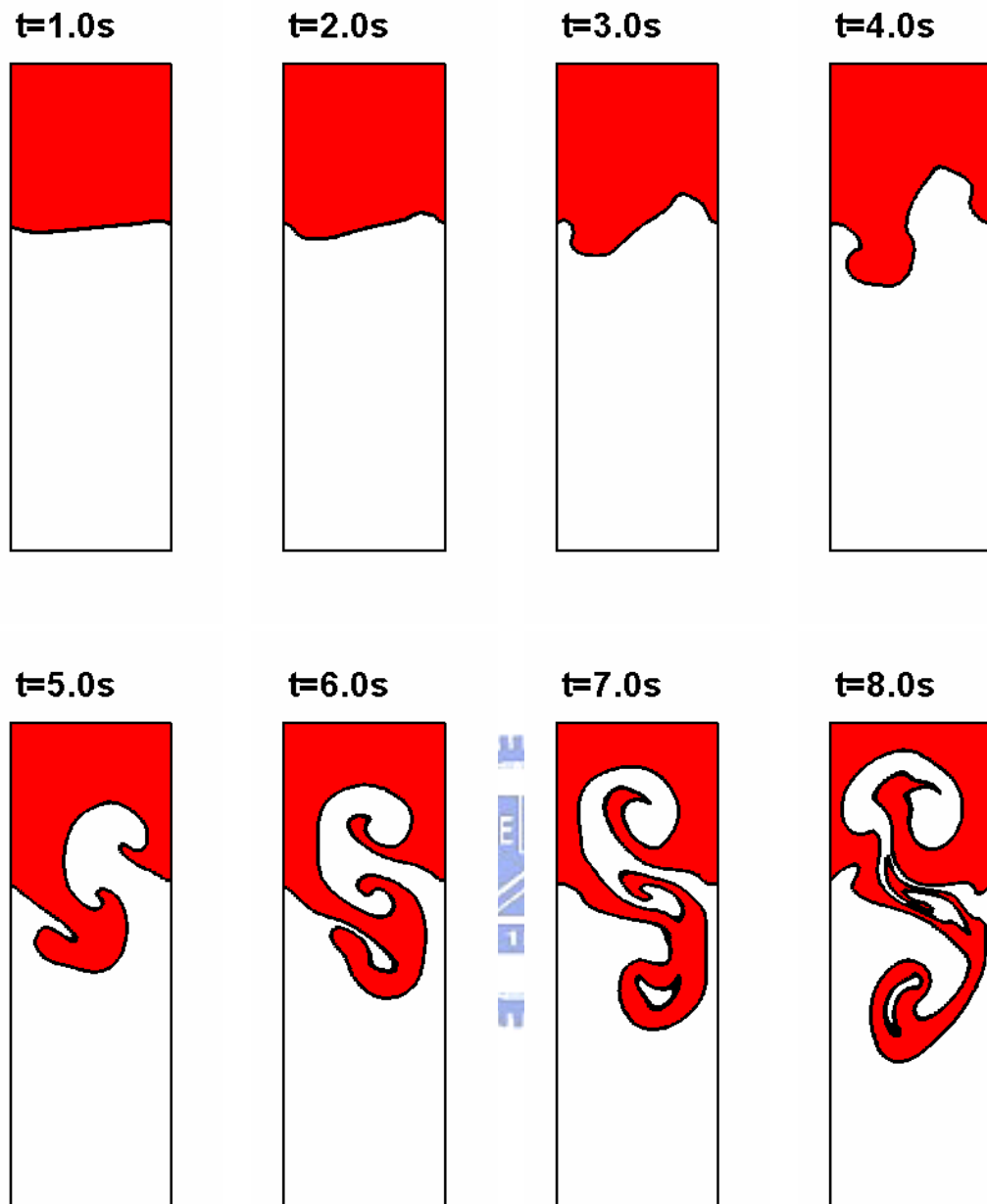


Figure 5.29 The numerical results of Rayleigh-Taylor instability adopting 5th kind of initial condition with uniform grids 64*192.

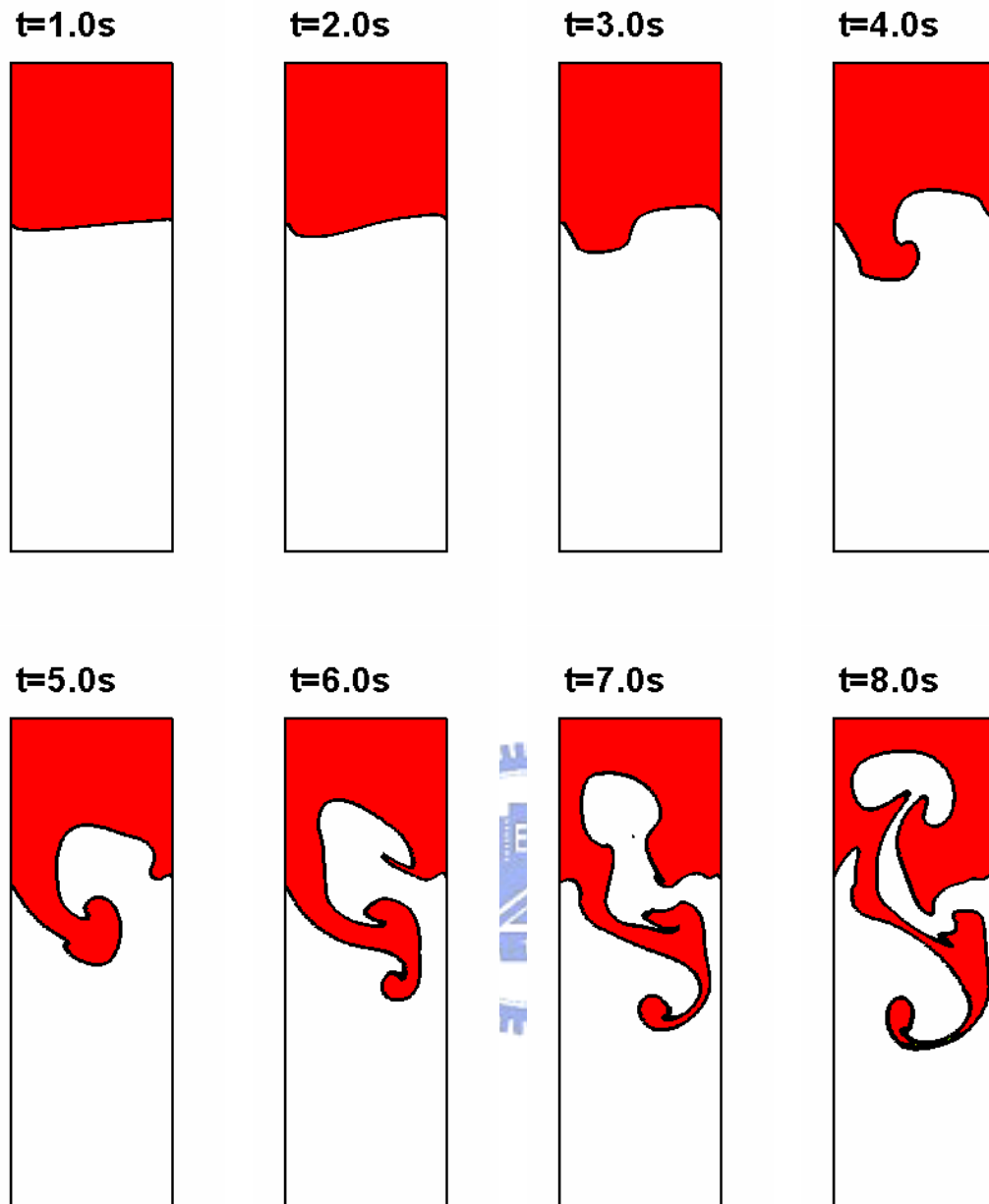


Figure 5.30 The numerical results of Rayleigh-Taylor instability adopting 5th kind of initial condition with non-uniform grids 80*284.

Furthermore, the following case uses similar settings but slip boundary condition is adopted at walls. The coefficients of two fluids are the same with the former case. The points of interface at walls are not fixed. Figure 5.31 to 5.35 illustrate the time evolution of Rayleigh-Taylor instability with different initial conditions.



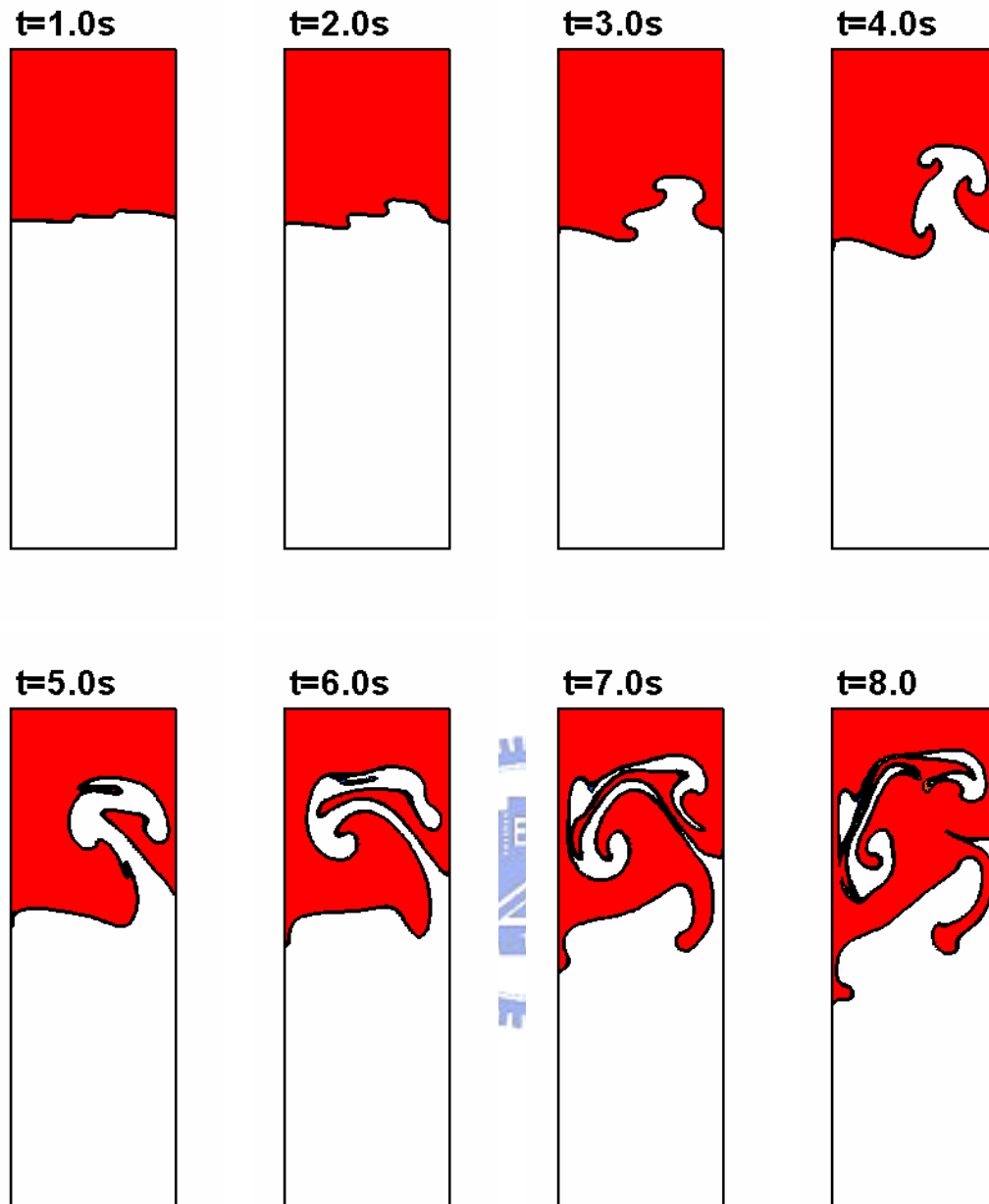


Figure 5.31 The numerical results of Rayleigh-Taylor instability adopting 1st kind of initial condition with non-uniform grids 64×192 and slip boundary condition.

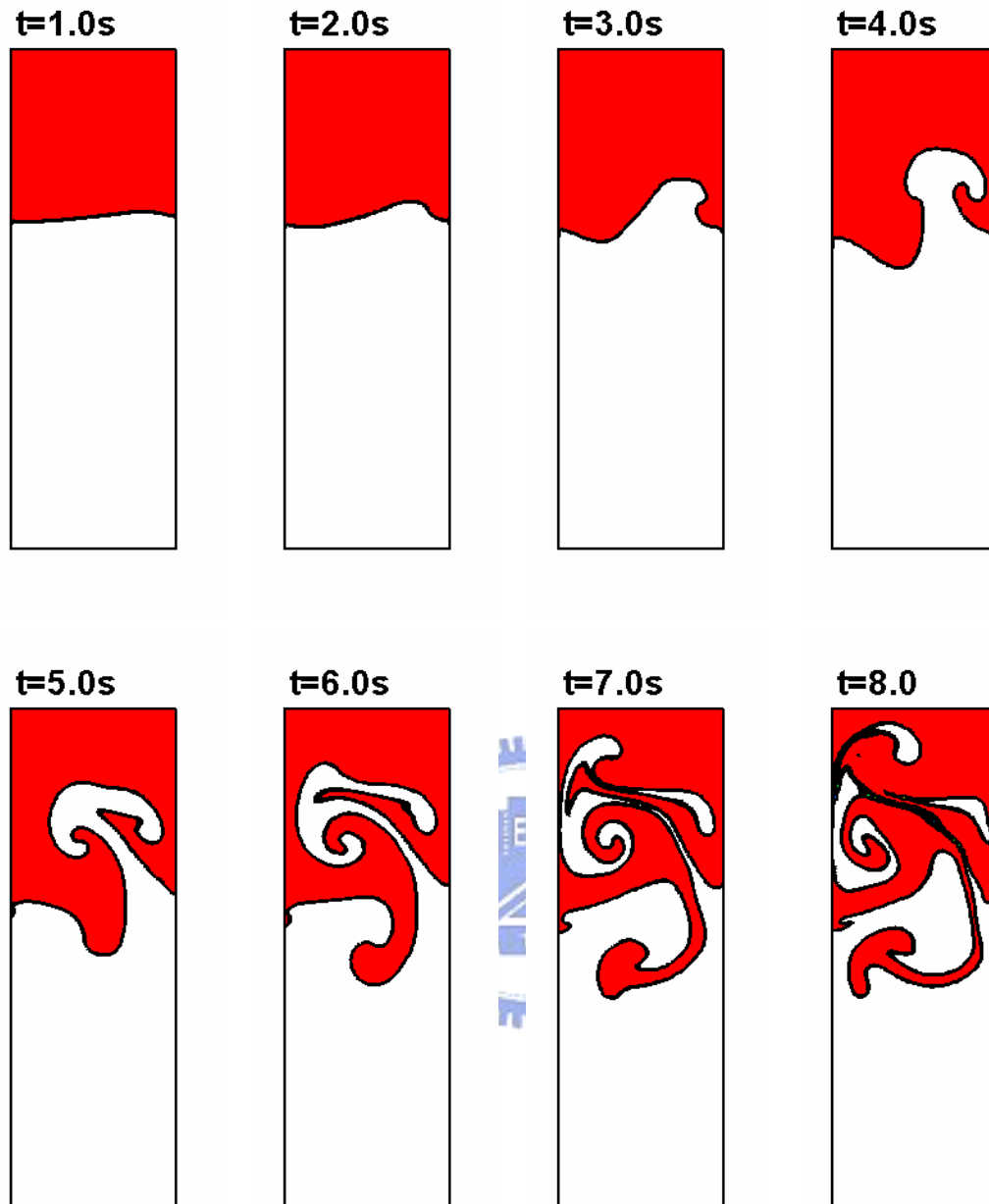


Figure 5.32 The numerical results of Rayleigh-Taylor instability adopting 2nd kind of initial condition with non-uniform grids 64*192 and slip boundary condition.

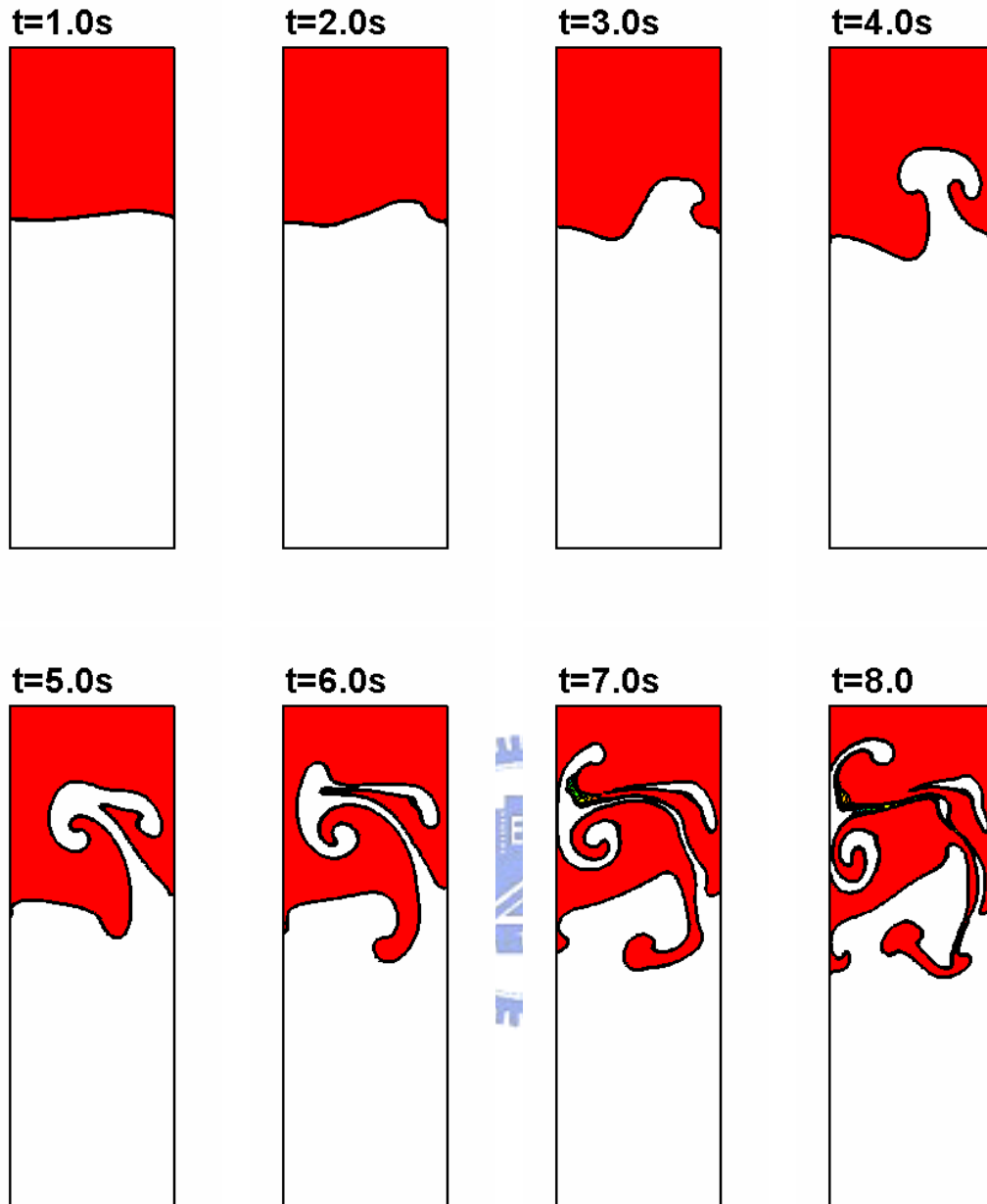


Figure 5.33 The numerical results of Rayleigh-Taylor instability adopting 3rd kind of initial condition with non-uniform grids 64×192 and slip boundary condition.

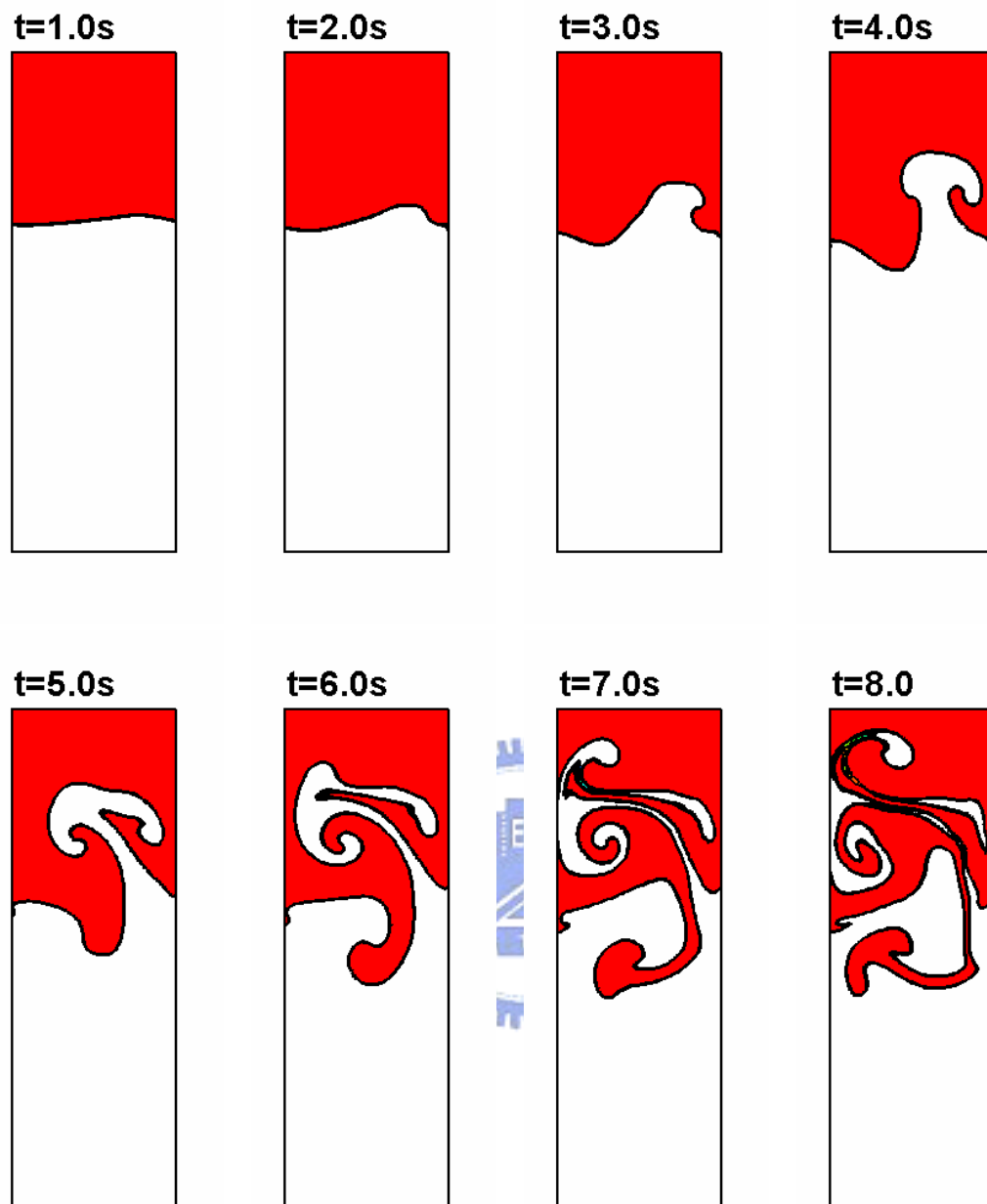


Figure 5.34 The numerical results of Rayleigh-Taylor instability adopting 4th kind of initial condition with non-uniform grids 64×192 and slip boundary condition.

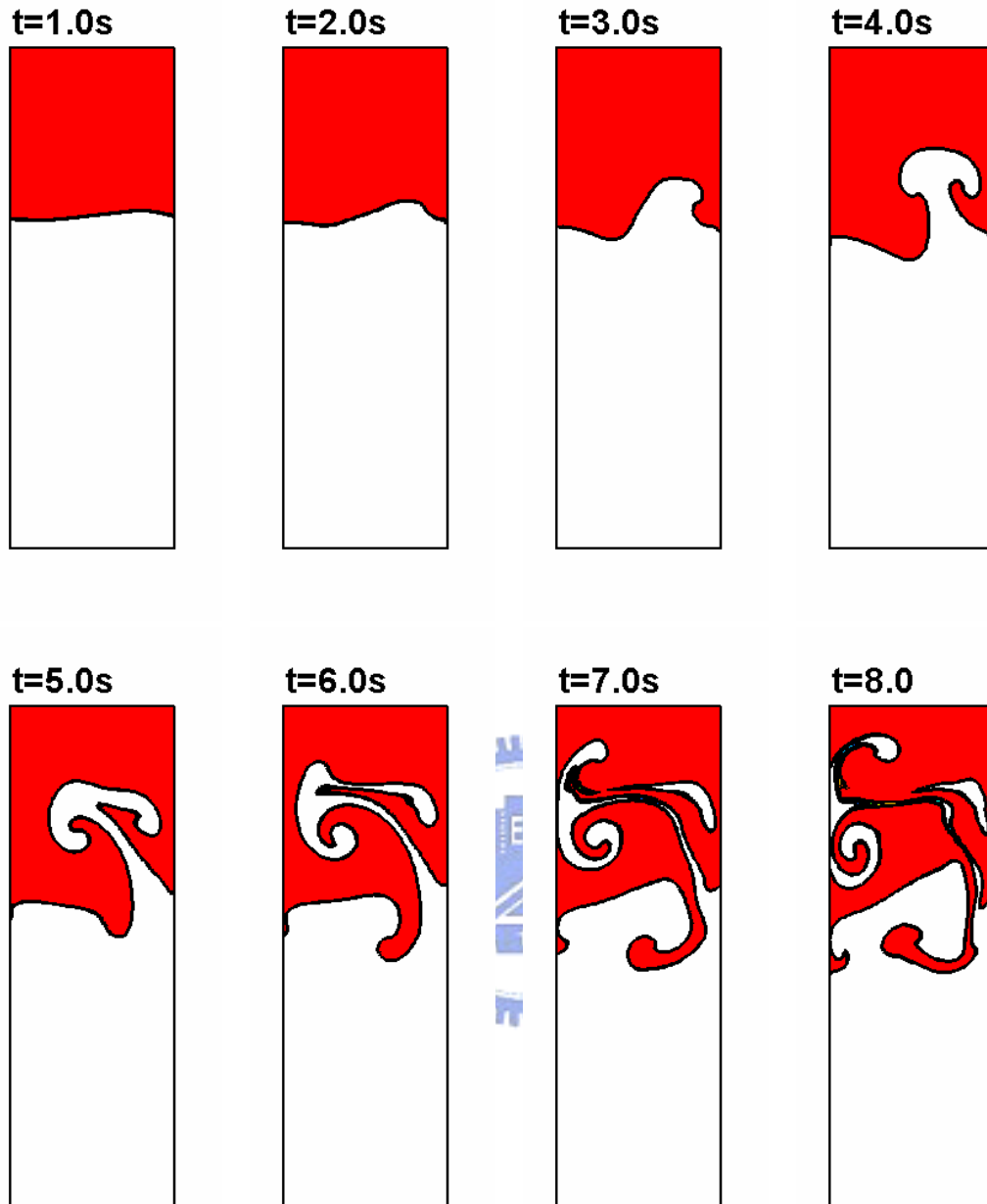


Figure 5.35 The numerical results of Rayleigh-Taylor instability adopting 5th kind of initial condition with non-uniform grids 64×192 and slip boundary condition.

5.8 Column collapse

Collapse with a return wave

Martin and Moyce [40] presented an experiment of column collapse and many numerical models are built for this example [4, 9, 30, 41]. Figure 5.35 shows the results of experiments by Koshizuka [41]. In the experimental setup, the tank is made of glass, with a base length of 0.584m. The water column, with a base length of 0.146m and a height of 0.292m, is initially supported on the right by a vertical plate drawn up at time $t=0.0s$. For the numerical calculation non-slip boundary conditions are applied to the bottom and sides of the tank. The top boundary is modeled as open boundary which pressure is fixed. The density of fluid 1 is 1000 and the viscosity is 0.01. For the fluid 2 the density is 1 and the viscosity is 0.001.

In this study, there are four types of grid configurations adopted: 48*28, 120*70, 240*104 and 120*165. The first three types of configurations have the same scale of computational domain (0.584m*0.340m). The last one increases the height of the tank and built for testing the open boundary condition.

The time evolutions are shown in Figure 5.37 to 5.40. The contour is $0.4 \leq \alpha \leq 0.6$ with 11 levels. At first, water column starts to collapse and the covered area at bottom increase until the leading edge touch the right wall. Then, water liquid splashes and starts to leave the domain at the top right corner. To continue, the water against the right wall starts to fall back under the influence of gravity. The backward moving wave has folded over and a small amount of air is trapped at $t=0.8s$. The water spray is produced. Finally, the spray touches the left wall again and traps a large air bubble.

Compare each configurations, the coarse grid introduces oscillation obviously. The flow field becomes unstable and numerical diffusion is produces when the water column returns to the left wall, especially in the coarse grid. Due to the region of air trapped is complex, the manner of reconstructing grid configuration can improve this problem.

In addition, surface tension force term is considered in the calculation and Figure 5.41 to 5.44 show the numerical results. It is not surprising that the results are not different from the former without surface tension. The shape of air bubbles in the returning water column is smoother.

Figure 5.45 shows the leading edge versus time. The calculated results show that the leading edge moves faster when the resolution of the grids increases. The height of the collapsing water column versus time is shown in Figure 5.46. For each calculations the predicted height is the same and it correspond very well with the experiment, except for the finer grids (240*140).



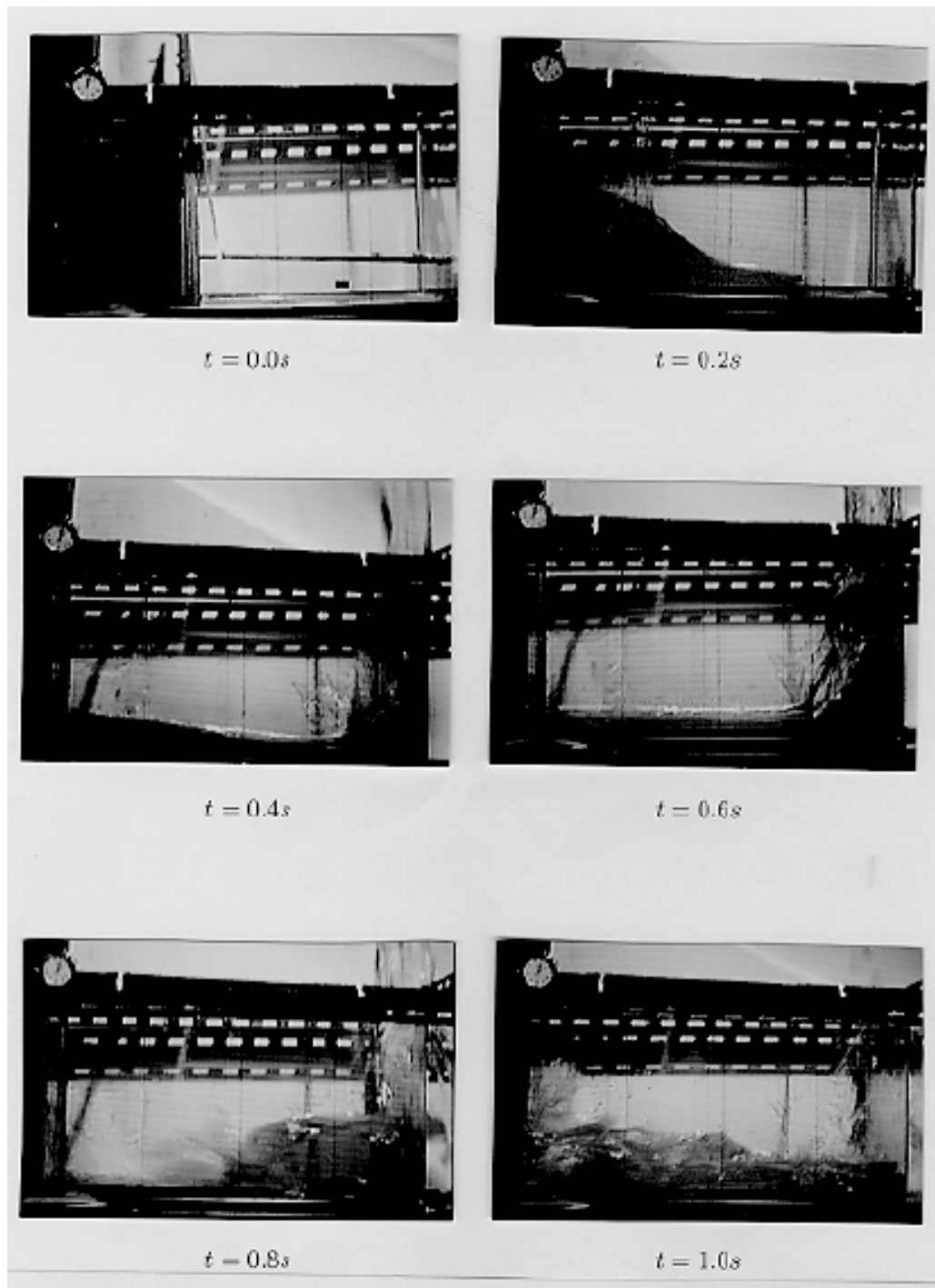


Figure 5.36 Experimental results of a collapsing water column by Koshizuka [40].

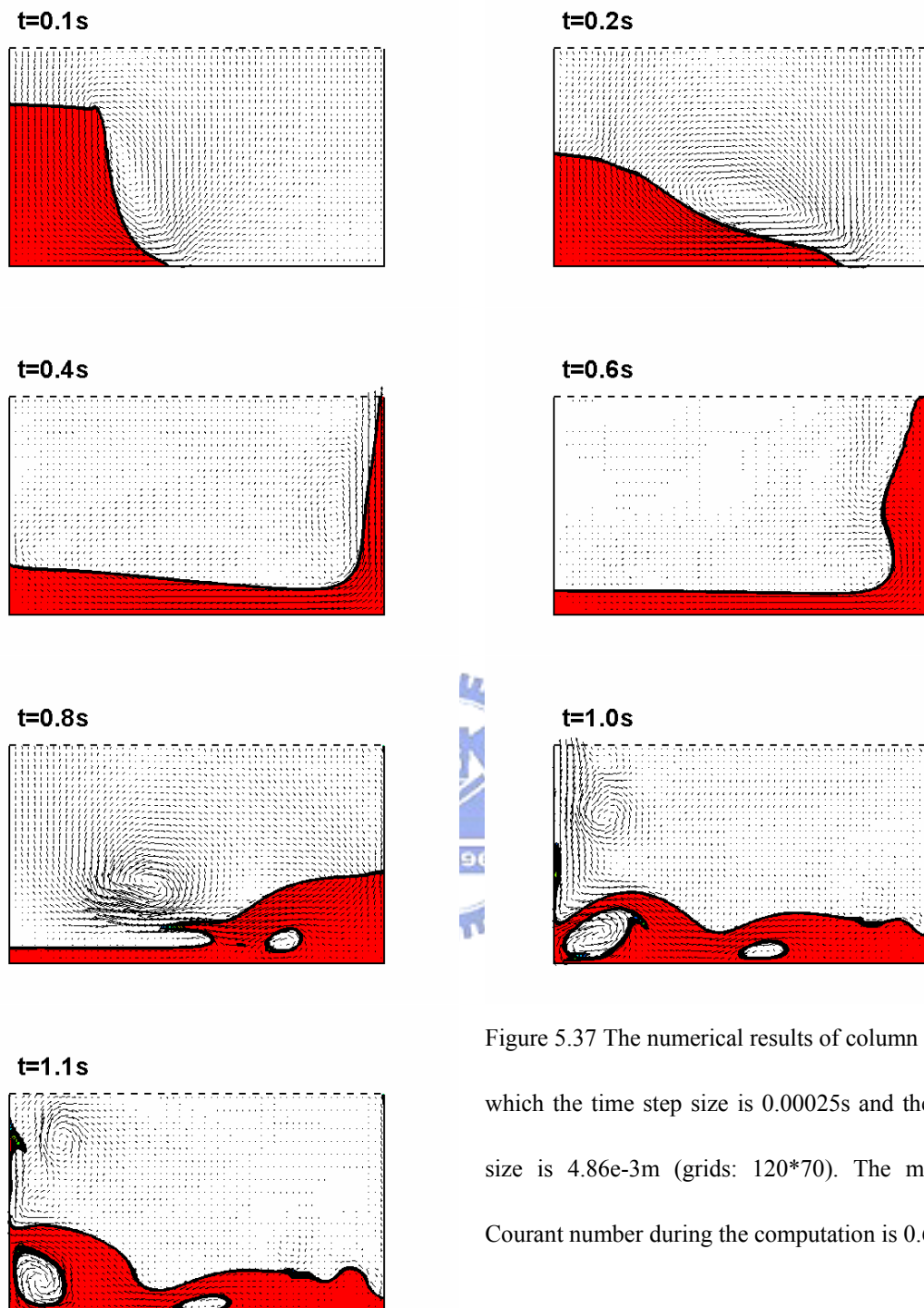


Figure 5.37 The numerical results of column collapse which the time step size is 0.00025s and the spatial size is 4.86e-3m (grids: 120*70). The maximum Courant number during the computation is 0.699.

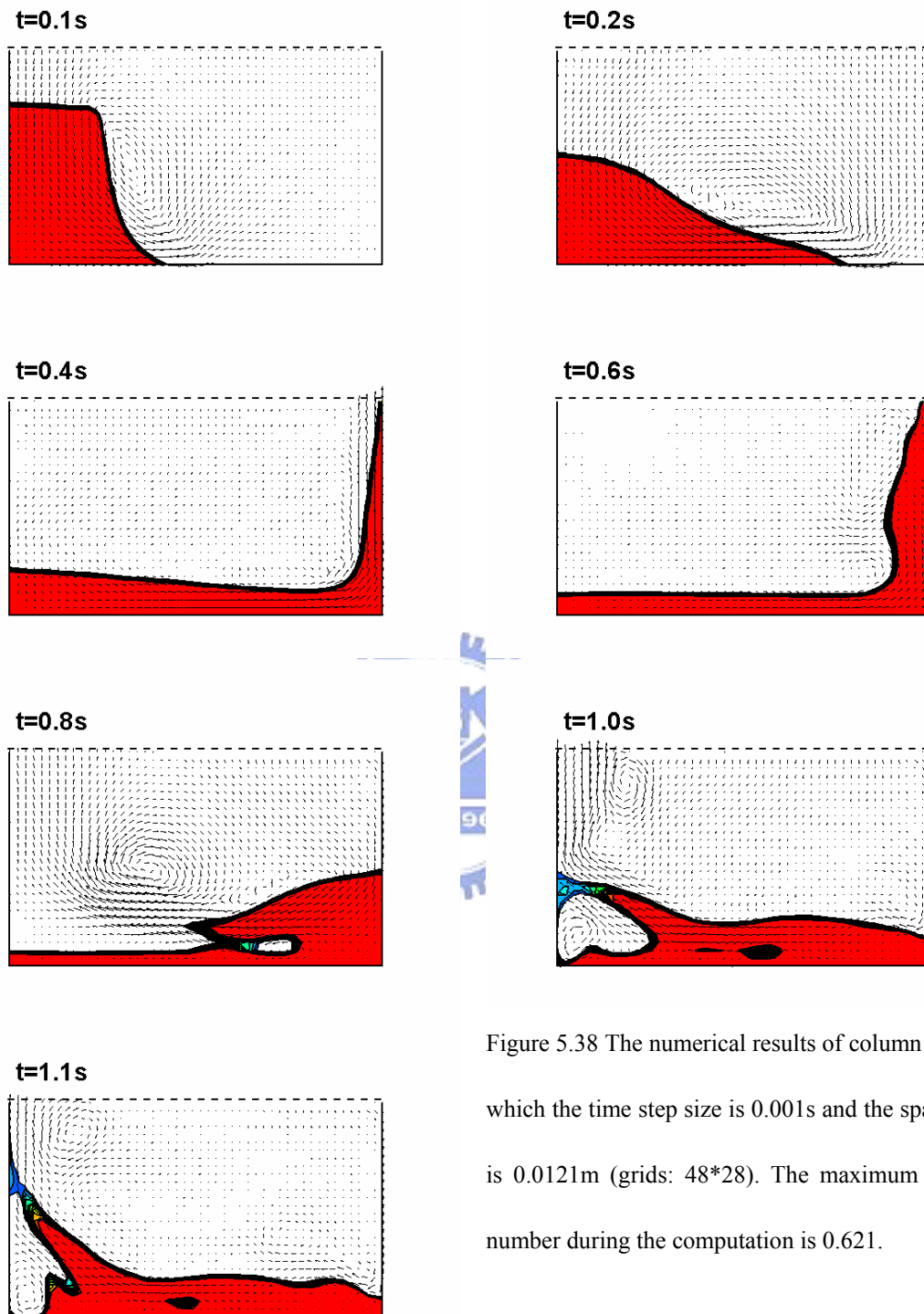


Figure 5.38 The numerical results of column collapse which the time step size is 0.001s and the spatial size is 0.0121m (grids: 48*28). The maximum Courant number during the computation is 0.621.

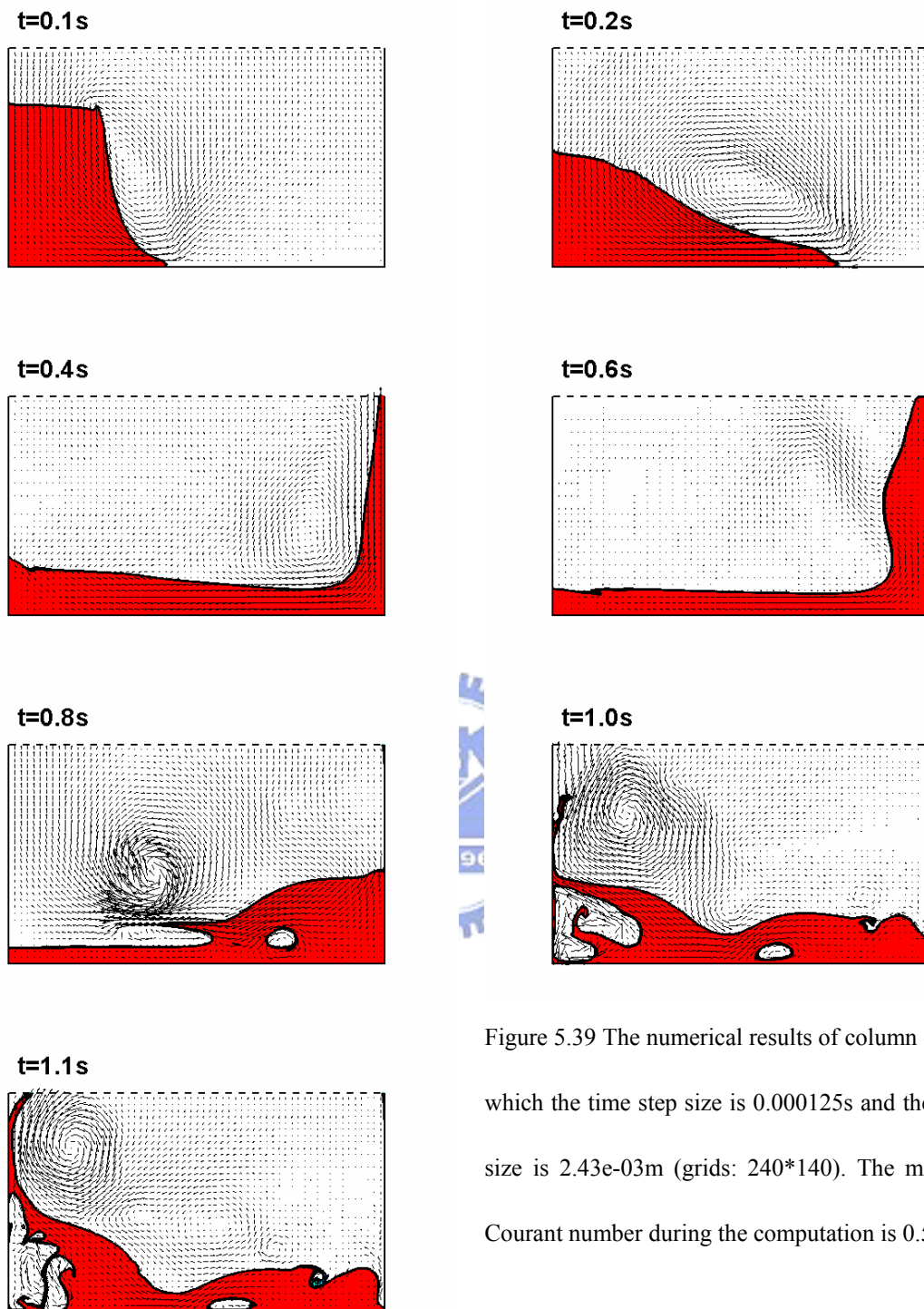


Figure 5.39 The numerical results of column collapse which the time step size is 0.000125s and the spatial size is 2.43e-03m (grids: 240*140). The maximum Courant number during the computation is 0.563.

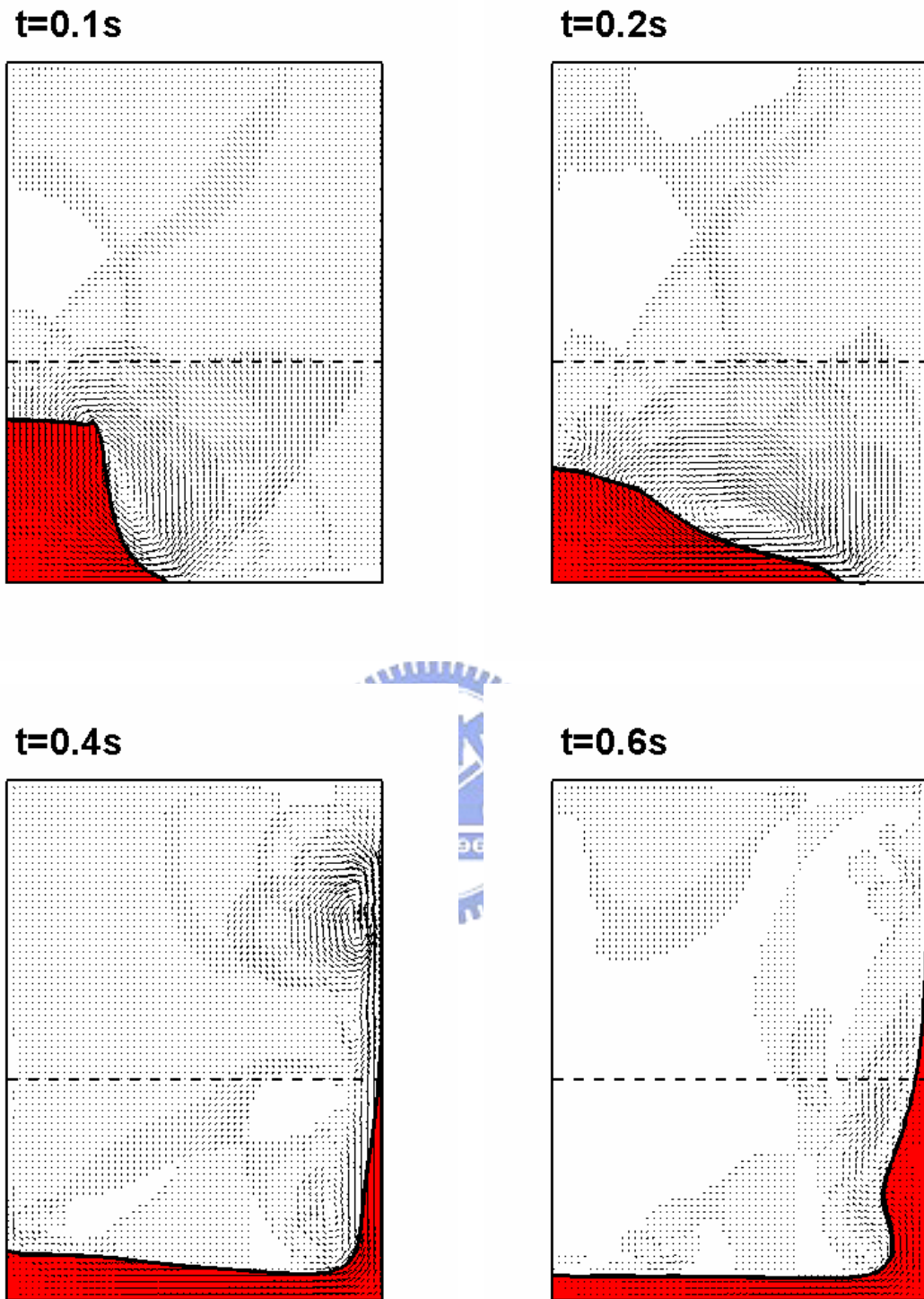


Figure 5.40 The numerical results of column collapse which the time step size is 0.00025s and the spatial size is 4.86e-03m (grids: 120*165). The maximum Courant number during the computation is 0.615.(*continue*)

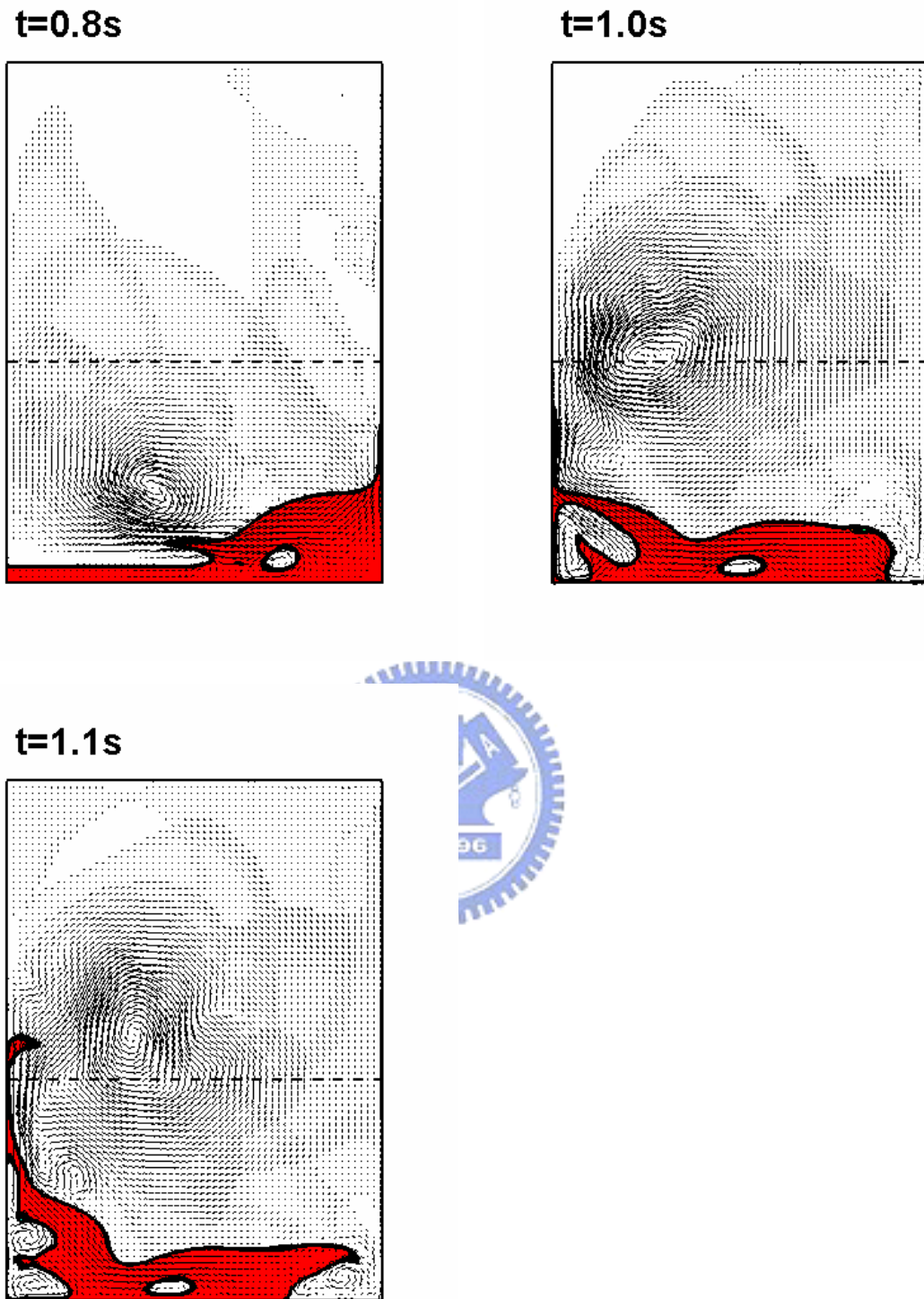


Figure 5.40 The numerical results of column collapse which the time step size is 0.00025s and the spatial size is 4.86e-03m (grids: 120*165). The maximum Courant number during the computation is 0.615.

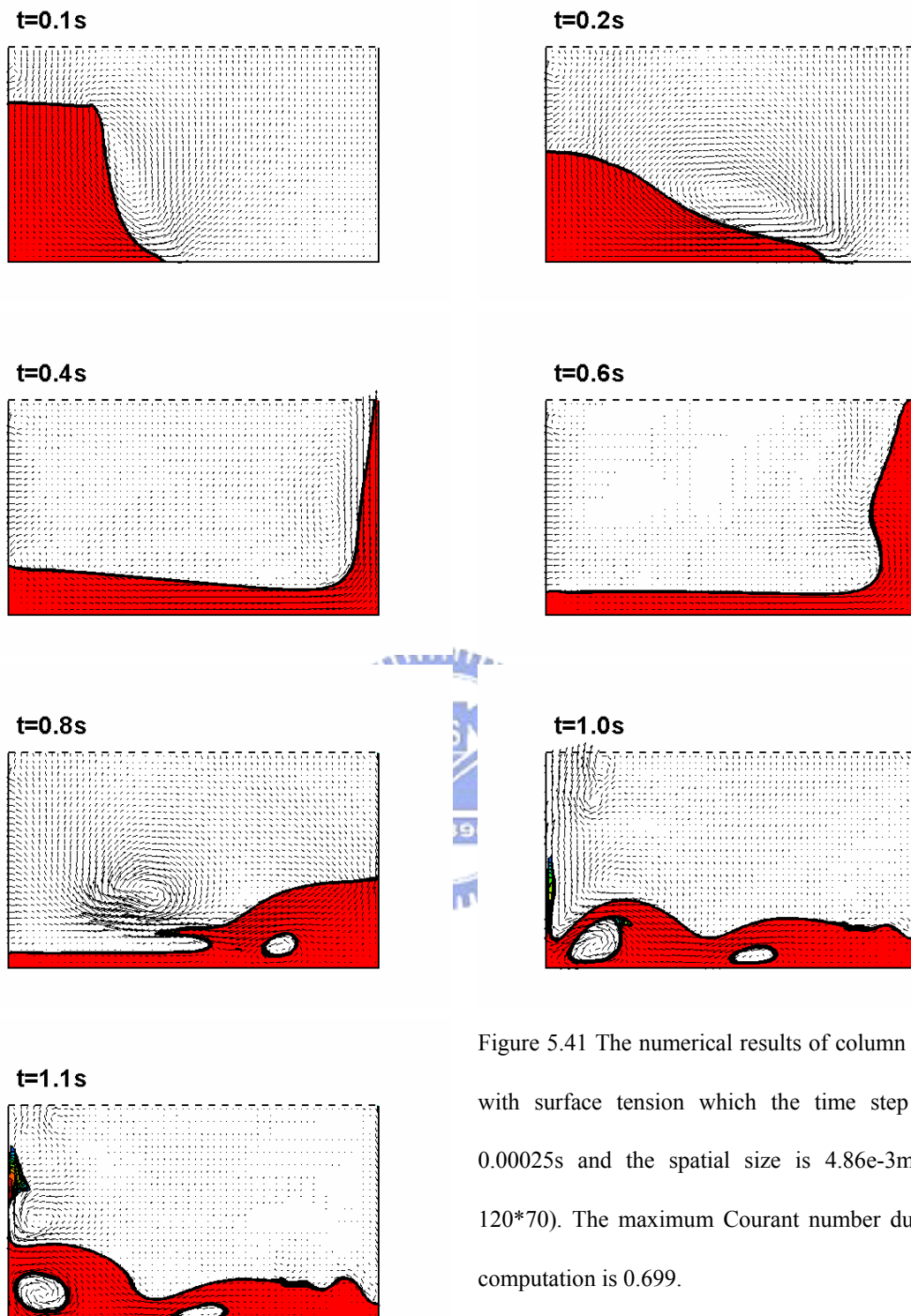


Figure 5.41 The numerical results of column collapse with surface tension which the time step size is 0.00025s and the spatial size is 4.86e-3m (grids: 120*70). The maximum Courant number during the computation is 0.699.

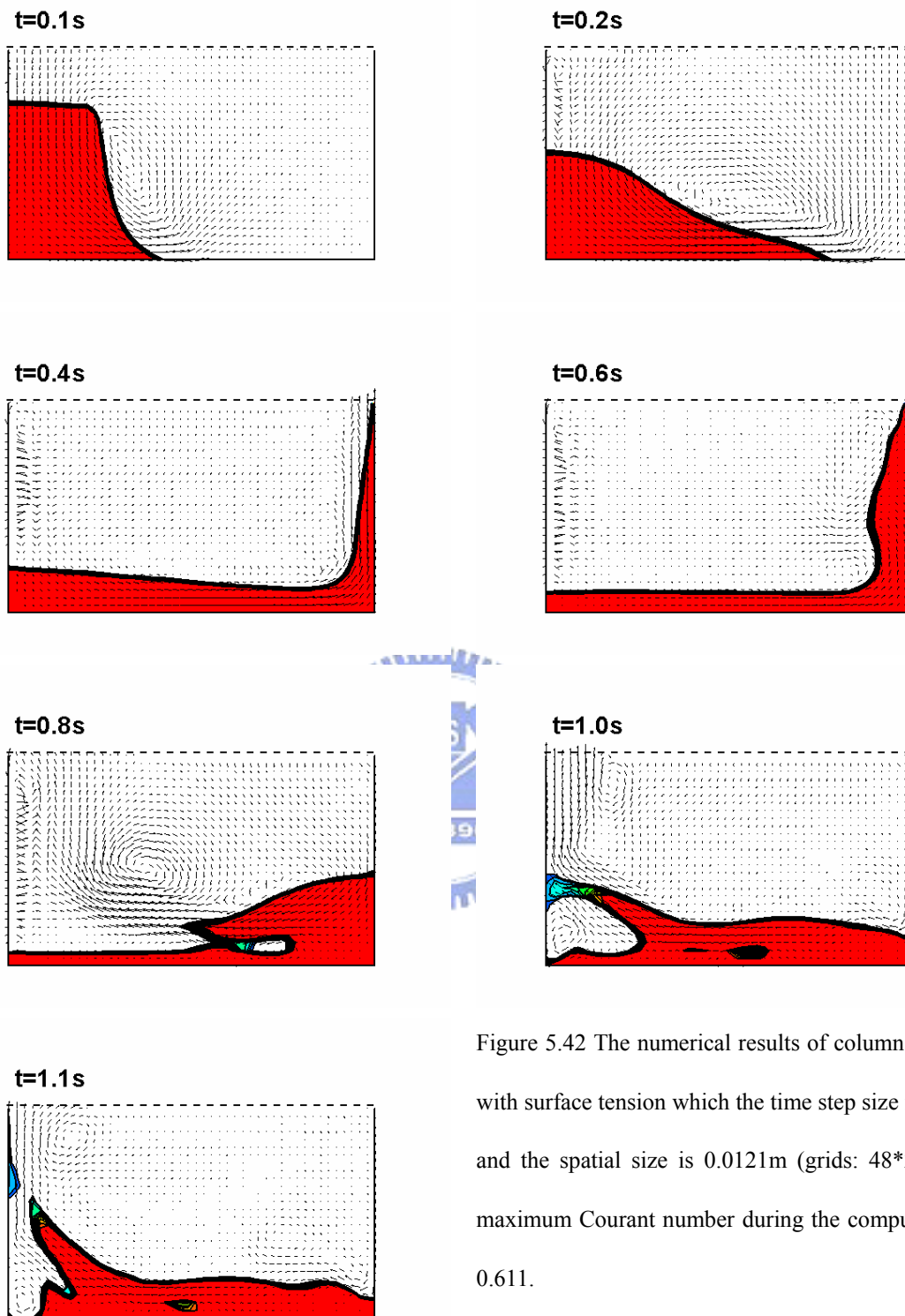


Figure 5.42 The numerical results of column collapse with surface tension which the time step size is 0.001s and the spatial size is 0.0121m (grids: 48*28). The maximum Courant number during the computation is 0.611.

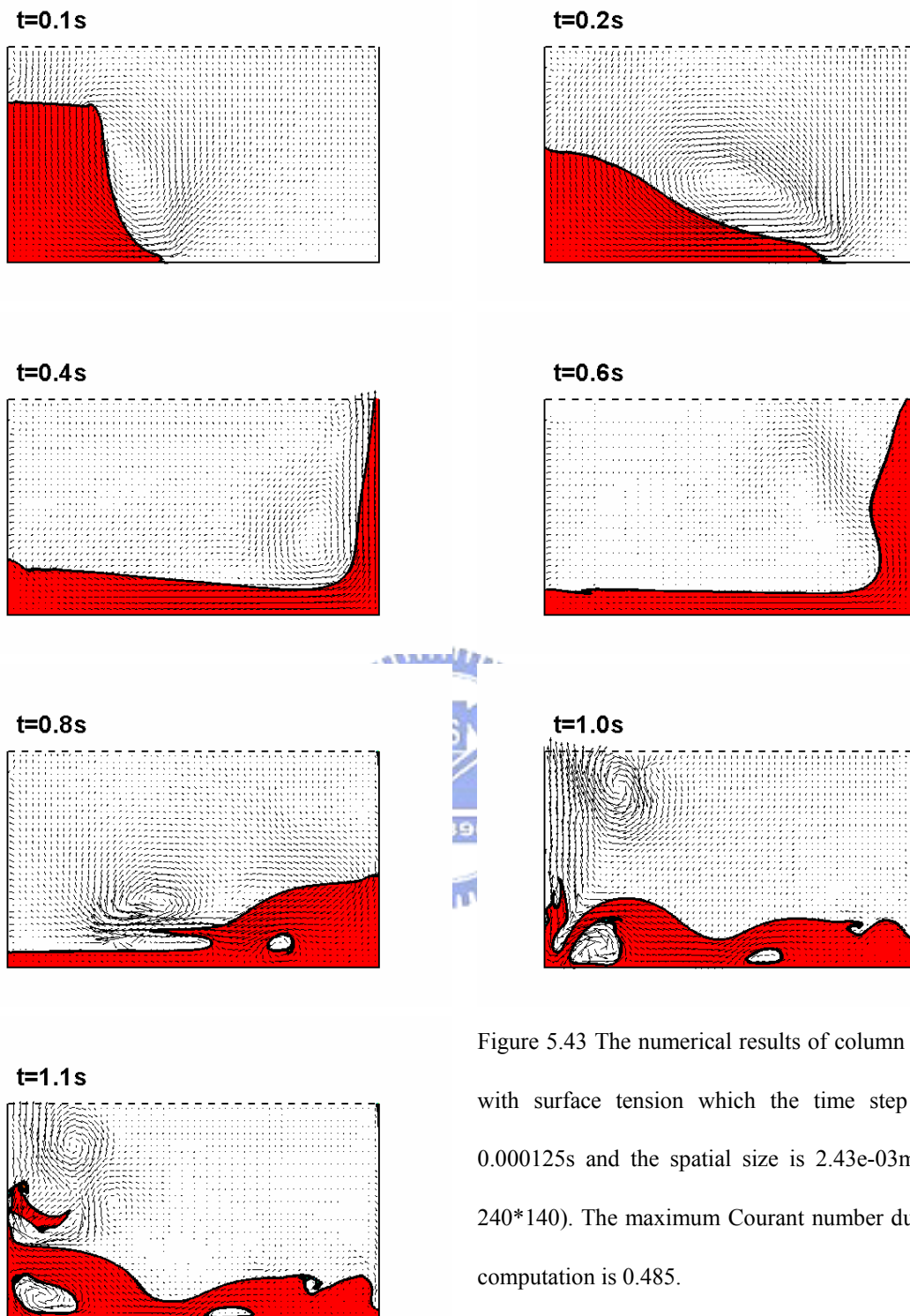


Figure 5.43 The numerical results of column collapse with surface tension which the time step size is 0.000125s and the spatial size is 2.43e-03m (grids: 240*140). The maximum Courant number during the computation is 0.485.

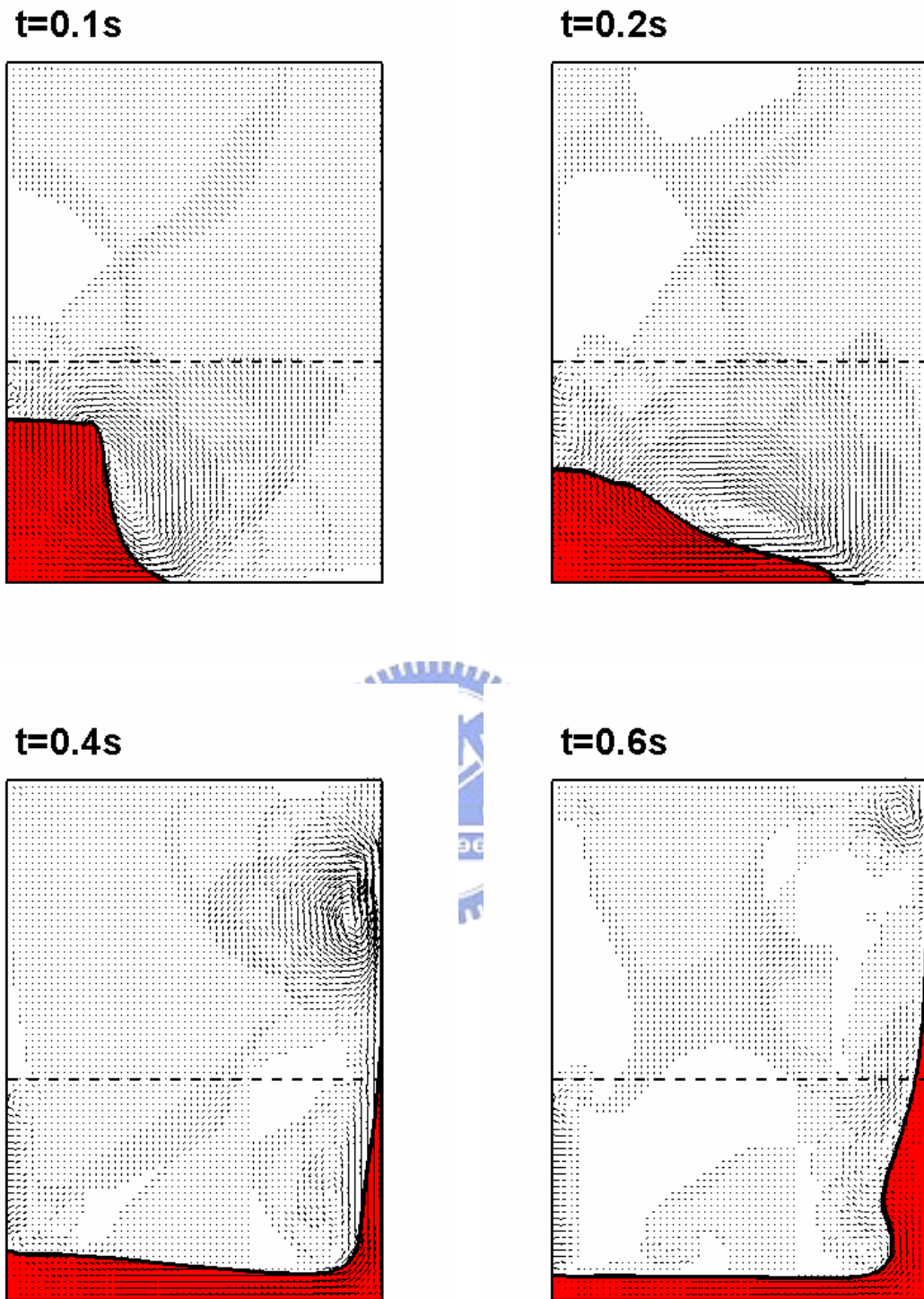


Figure 5.44 The numerical results of column collapse with surface tension which the time step size is 0.00025s and the spatial size is 4.86e-03m (grids: 120*165). The maximum Courant number during the computation is 0.597.(continue)

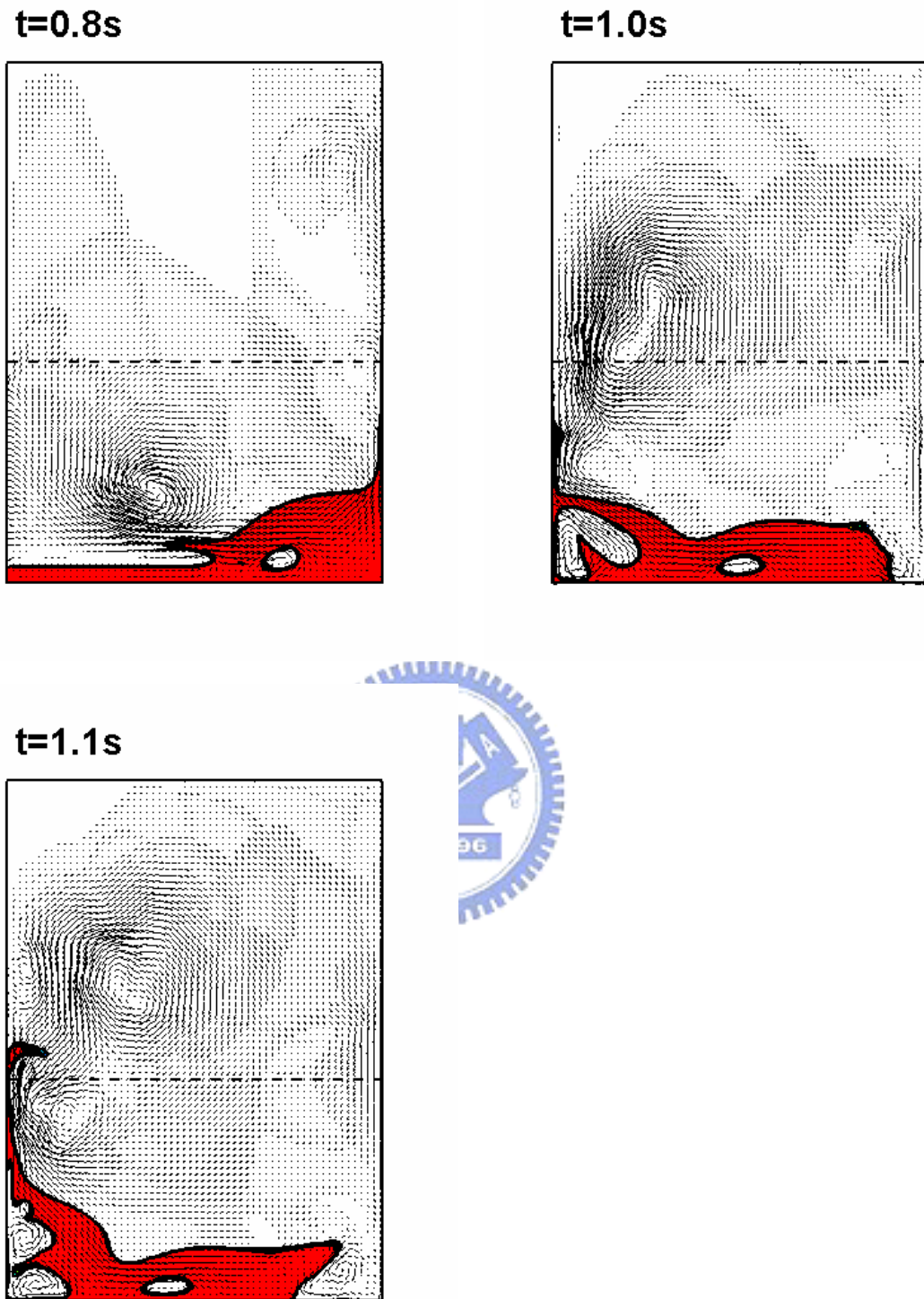


Figure 5.44 The numerical results of column collapse with surface tension which the time step size is 0.00025s and the spatial size is 4.86e-03m (grids: 120*165). The maximum Courant number during the computation is 0.597.

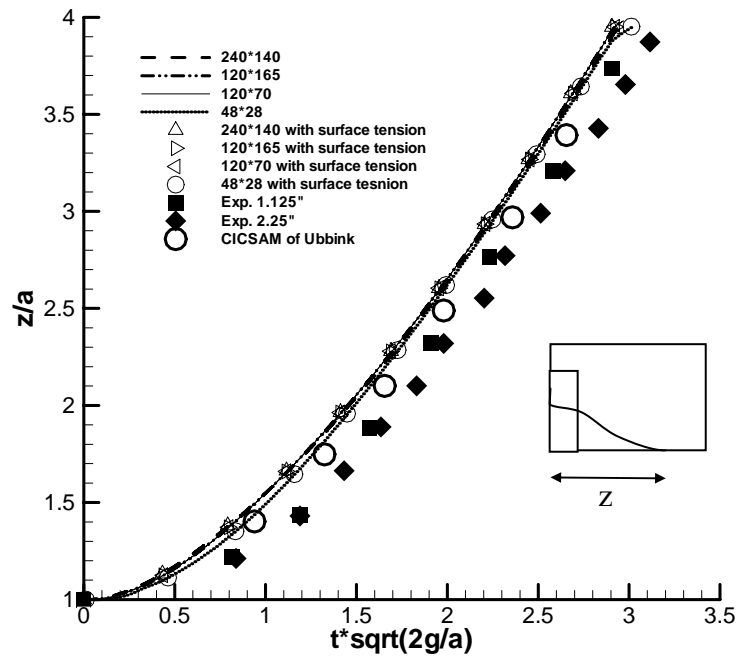


Figure 5.45 The position of the leading edge versus time.

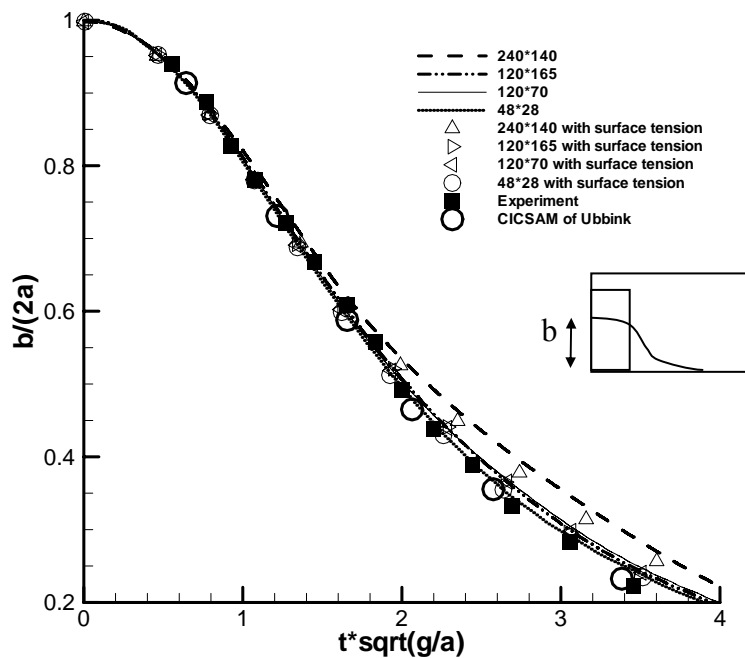


Figure 5.46 The height of the collapsing water column versus time.

Collapse with an obstacle

The example of column collapse with an obstacle is more complicated than the previous one. The dimensions of tank are the same as the previous experiment but a small obstacle is placed in the way of the wave front. The obstacle ($0.024\text{m} \times 0.048\text{m}$) is placed on the bottom of the tank, in the way of the moving front with its lower left corner in the center of the tank. For the numerical calculation, the computational domain increases in height. In this study, open boundary and close boundary (wall) at top are tested, respectively. Figure 5.47 shows the experimental result by Koshizuka. Figure 5.48 and 5.49 show the calculated results. The solid line stands for wall and the dashed line presents open boundary. The water column collapse and is the same with previous example until touch a small obstacle. Then, the movement of the leading edge has been obstructed by the small obstacle and a tongue of water splash up. As time goes by, the tongue continues its movement toward the opposite wall until impinges the wall and trapping air beneath it. Finally, water falls down under the action of gravity. Although the velocity flow fields are not totally similar, the distribution of fluids is almost the same.

Surface tension term is considered and Figure 5.50 and 5.51 show the results. As well as the previous case, the influence of surface tension is not important.

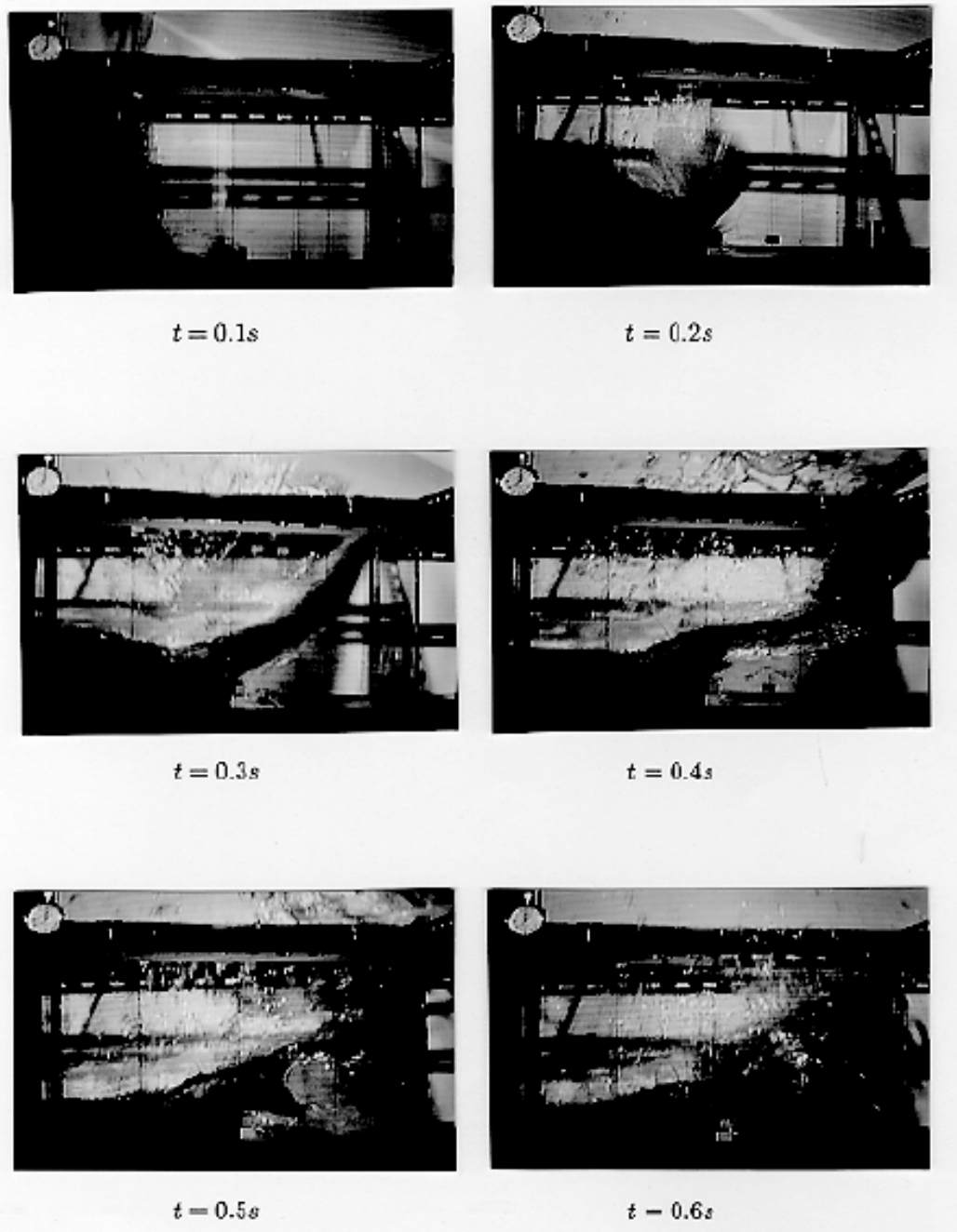


Figure 5.47 Experimental results of a collapsing water column hitting an obstacle (Koshizuka [40])

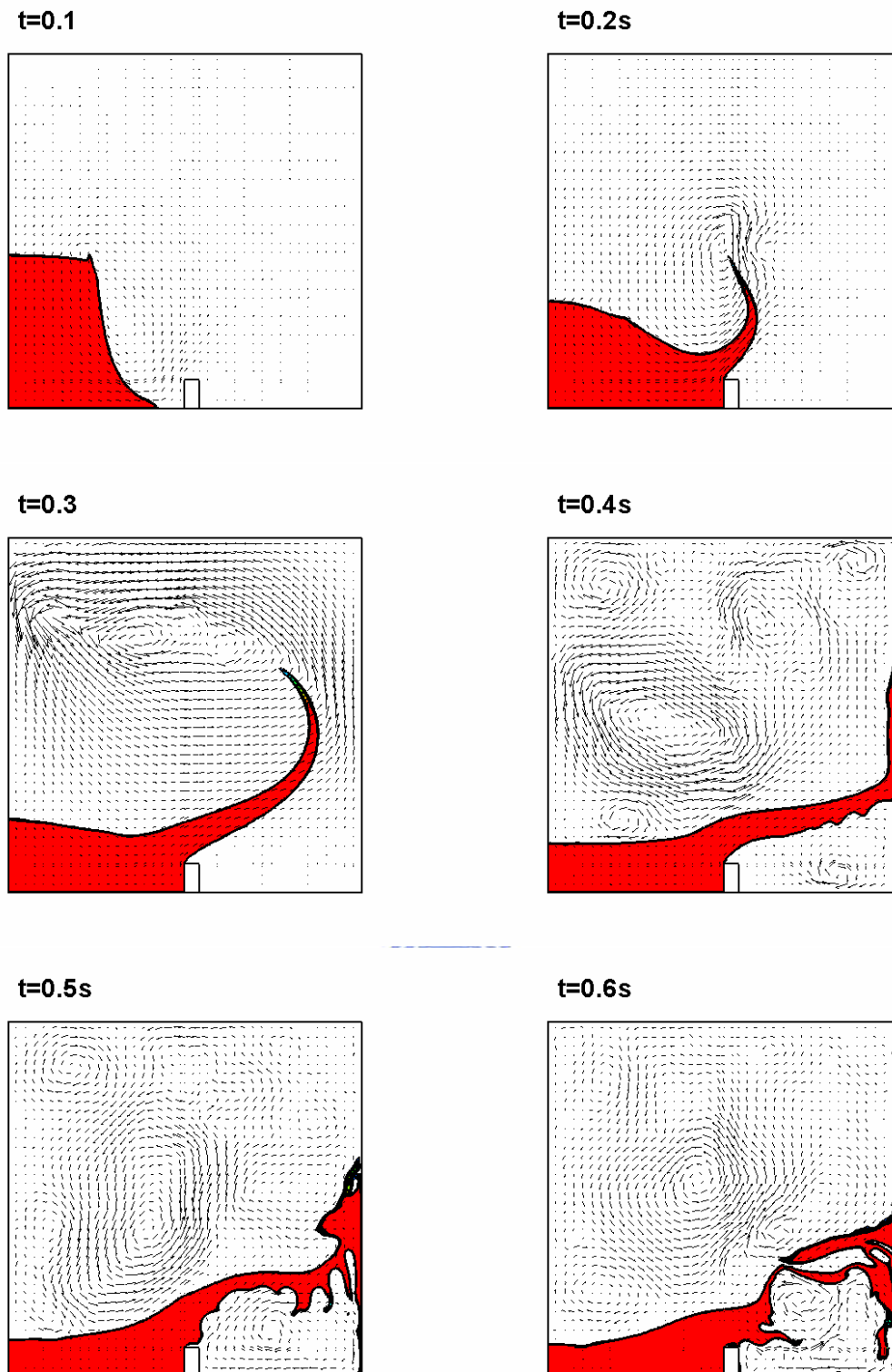


Figure 5.48 The numerical results of column collapse with obstacle without surface tension. The upper boundary at the computational domain is wall.

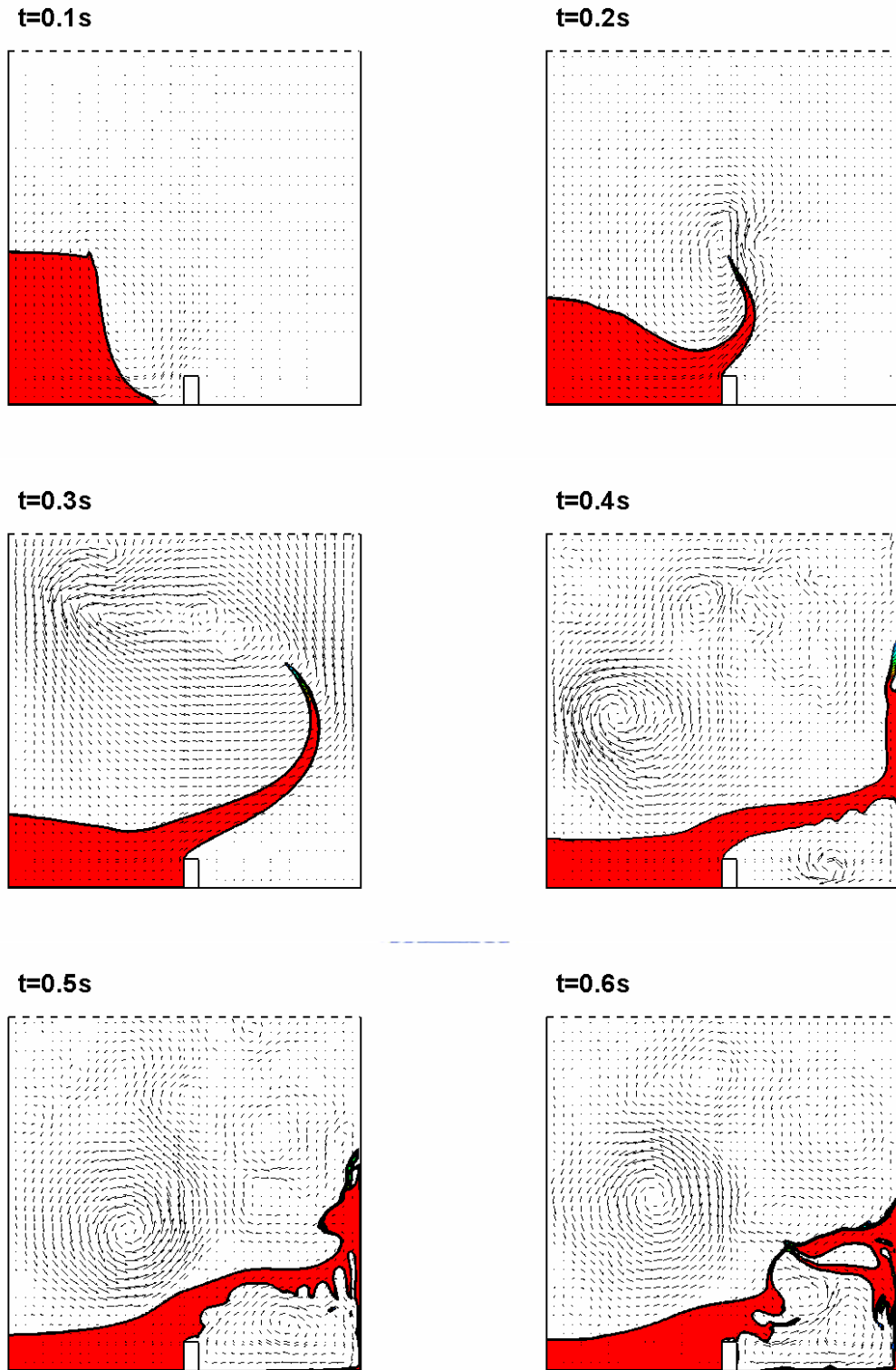


Figure 5.49 The numerical results of column collapse with obstacle without surface tension. The upper boundary at the computational domain is open boundary which pressure is fixed.

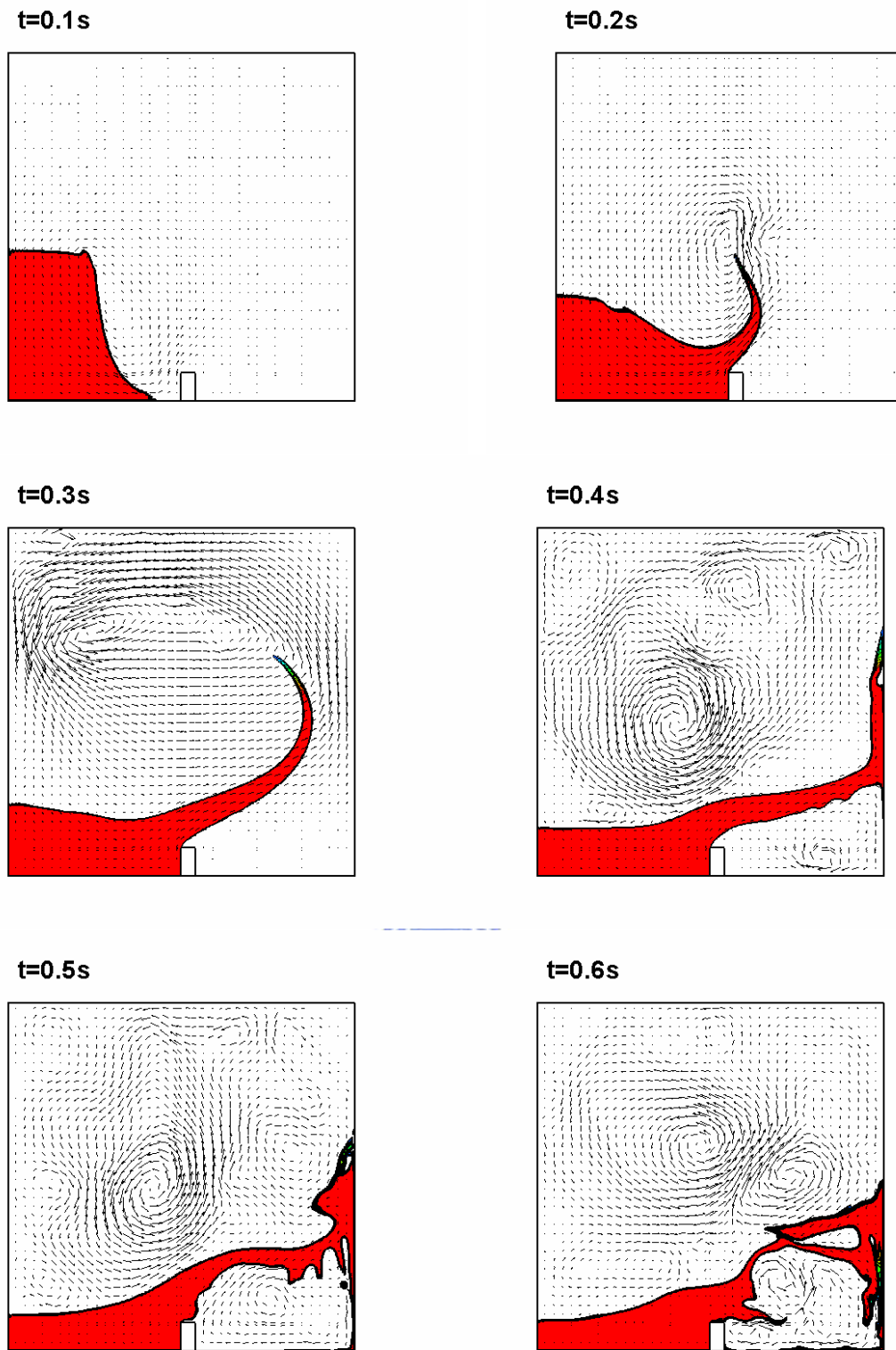


Figure 5.50 The numerical results of column collapse with obstacle with surface tension. The upper boundary at the computational domain is wall.

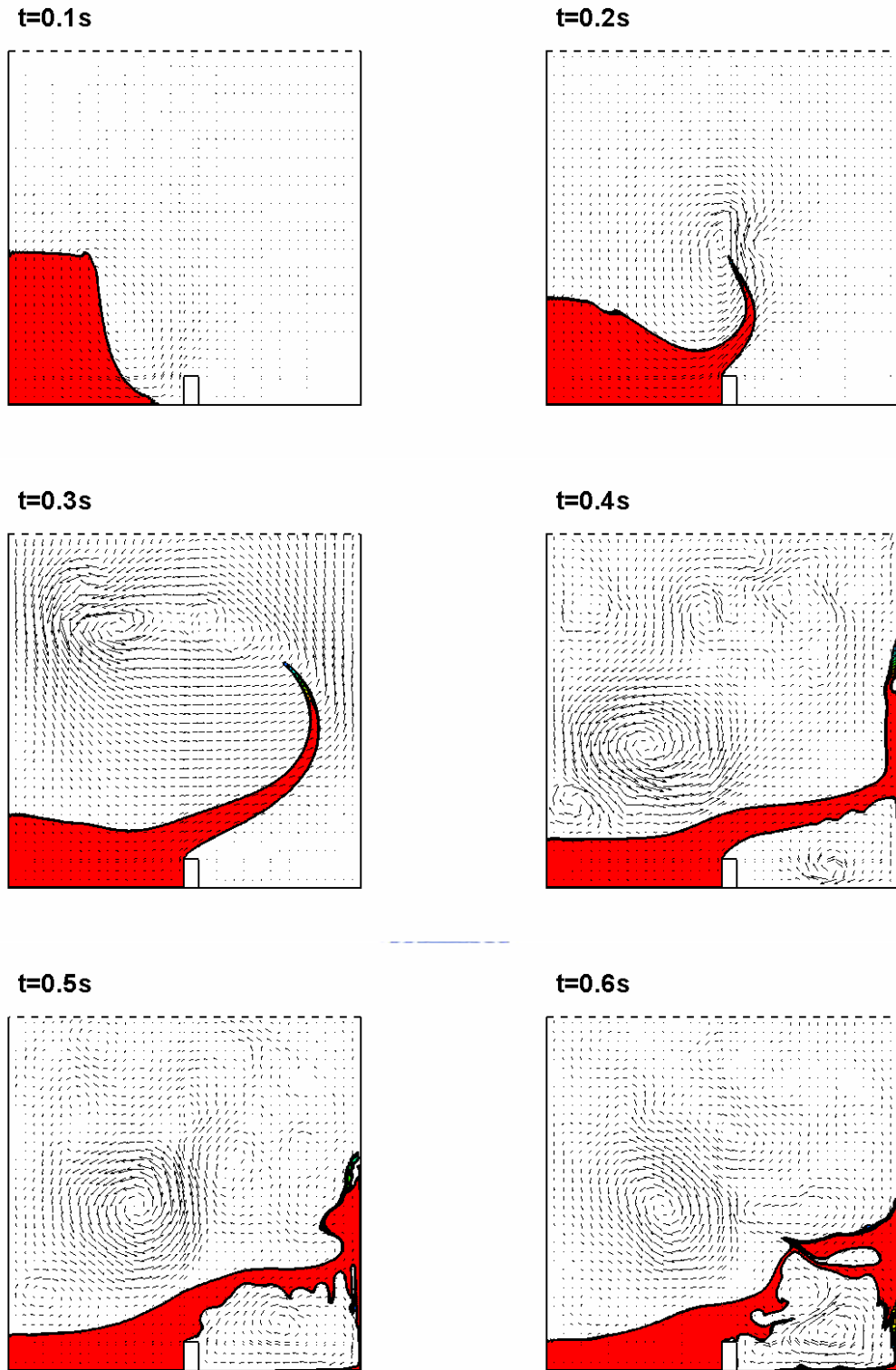


Figure 5.51 The numerical results of column collapse with obstacle with surface tension. The upper boundary at the computational domain is open boundary which pressure is fixed.

5.9 Hydraulic bore

A hydraulic bore can be generated by pushing a horizontal layer of liquid into a vertical wall [42]. The flow within the wave itself is very irregular and the exact interface is indeterminate. Hence, the other information which referred by Stoker [42] is the height of the vertical wall. Some numerical predictions are presented by Hirt and Nichols [4], and Ubbink [30]. Figure 5.52 presents the physical model of hydraulic bore. The base length of domain is 12.5m and the height is 4m. The initial depth of the liquid is 1m and it is moving uniformly to the right with unit velocity. Slip boundary conditions are applied at right, bottom and top-left boundary. The top boundary is treated as open boundary which pressure is specified. The computational domain is discretised with uniform grids of 50 cells in horizontal and non-uniform grids of 30 cells in vertical. Figure 5.53 illustrated schematic representation of grid configuration for this example.

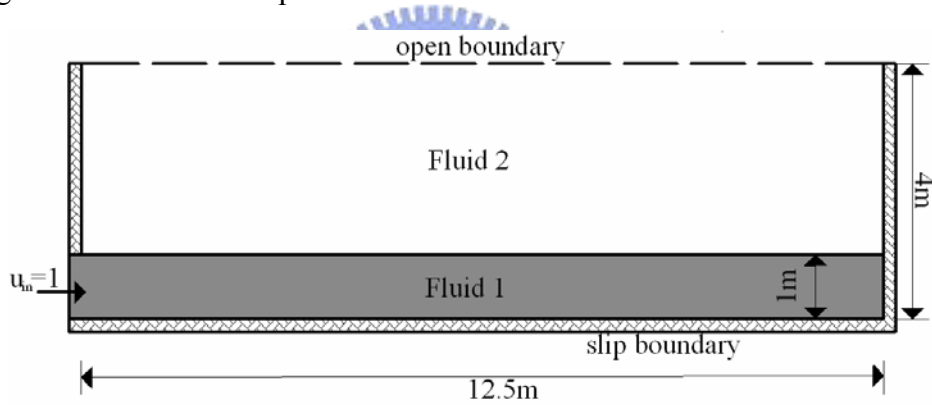


Figure 5.52 The Physical model of hydraulic bore.

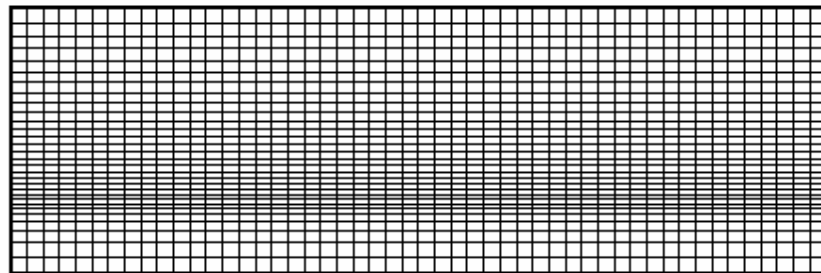


Figure 5.53 Schematic representation of grid configuration for the bore.

Viscosities of both fluids are taken as zero, because the theoretical solution is calculated for inviscid flow. The densities of fluid 1 (water) and fluid 2 (air) are $\rho_1=1000$ and $\rho_2=1$, respectively. The time step size is 0.005s and the gravity is 1 for this numerical calculation. (numerical results for this case are also presented by Hirt and Nichols [4], and Ubbink[30]). Time evolutions of the numerical results are shown in Figure 5.54. At first, water crashes the right wall and results in a reacting force. Interface continuously rolls itself and traps large air in.

The theoretical height, predicted height of percentage of error of this example and Ubbink are presented in Table 5.2. It reveals that this numerical method can deal with a breakup model well.

	Theoretical height	Predicted height	Error (%)
SUPERBEE+MUSCL	2.19	2.20	0.45
CICSAM of Ubbink	2.19	2.17	0.9

Figure 5.2 Comparison of the numerical results of hydraulic bore.

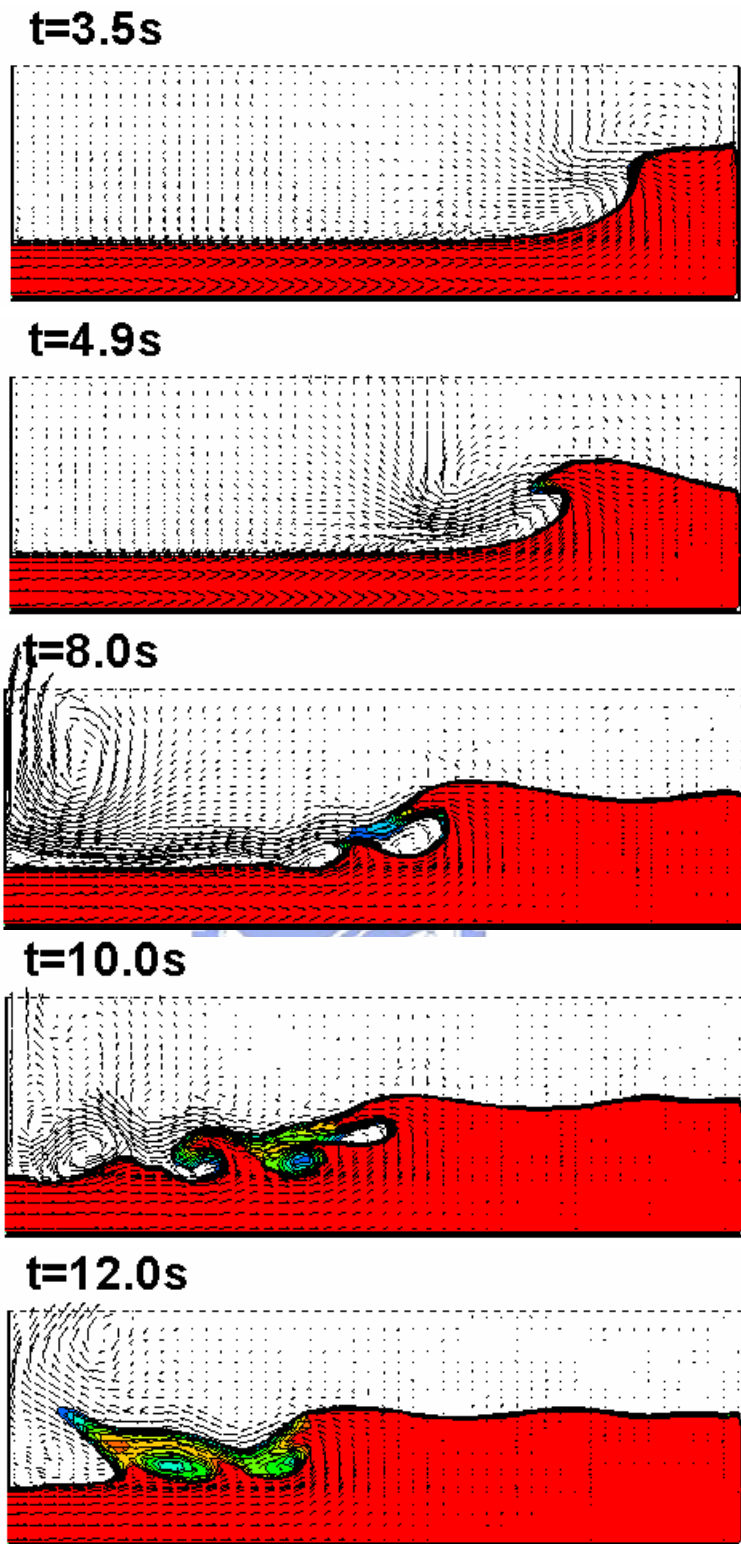
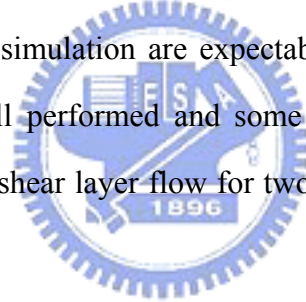


Figure 5.54 Velocity vectors and fluid configuration for the bore calculated with $g=1.0$ at times 3.5s, 4.9s, 8.0s, 10.0s and 12.0s.

The following uses the same computational domain and grid configuration with the former case but the bottom fluid layer is rest. There are no correlations with experimental or analytical data will be made. The density of both fluids are $\rho_1=1000$ and $\rho_2=1$. The gravity is 1 m/s^2 . Three types of inlet settings ($u=1 \text{ m/s}$, $u=2 \text{ m/s}$ and $u=3 \text{ m/s}$) are adopted and Figure 5.55 to 5.57 illustrated the time evolution of numerical simulation, respectively.

In Figure 5.55, the water on the left generates a pulse. This pulse, or water wave, will move forward until crashing the right boundary. Figure 5.56 reveals that the amplitude of water wave is greater and moves faster. After the water wave gets in touch with the right wall, the height of free surface raises gradually. In Figure 5.57, the second panel ($t=3.0\text{s}$) shows that the water wave rolls and transforms into a “tongue” shape. The velocity on this water tongue has opposite direction to the inlet velocity. As time goes by, some airs are trapped and produce a number of bubbles. Besides, the free surface separates with the right wall and traps air.

The results of numerical simulation are expectable and reasonable. In conclusion, this two-fluids flow system is well performed and some further investigation can be made in future work. For example, the shear layer flow for two immiscible fluids is a popular subject in biochemical engineering.



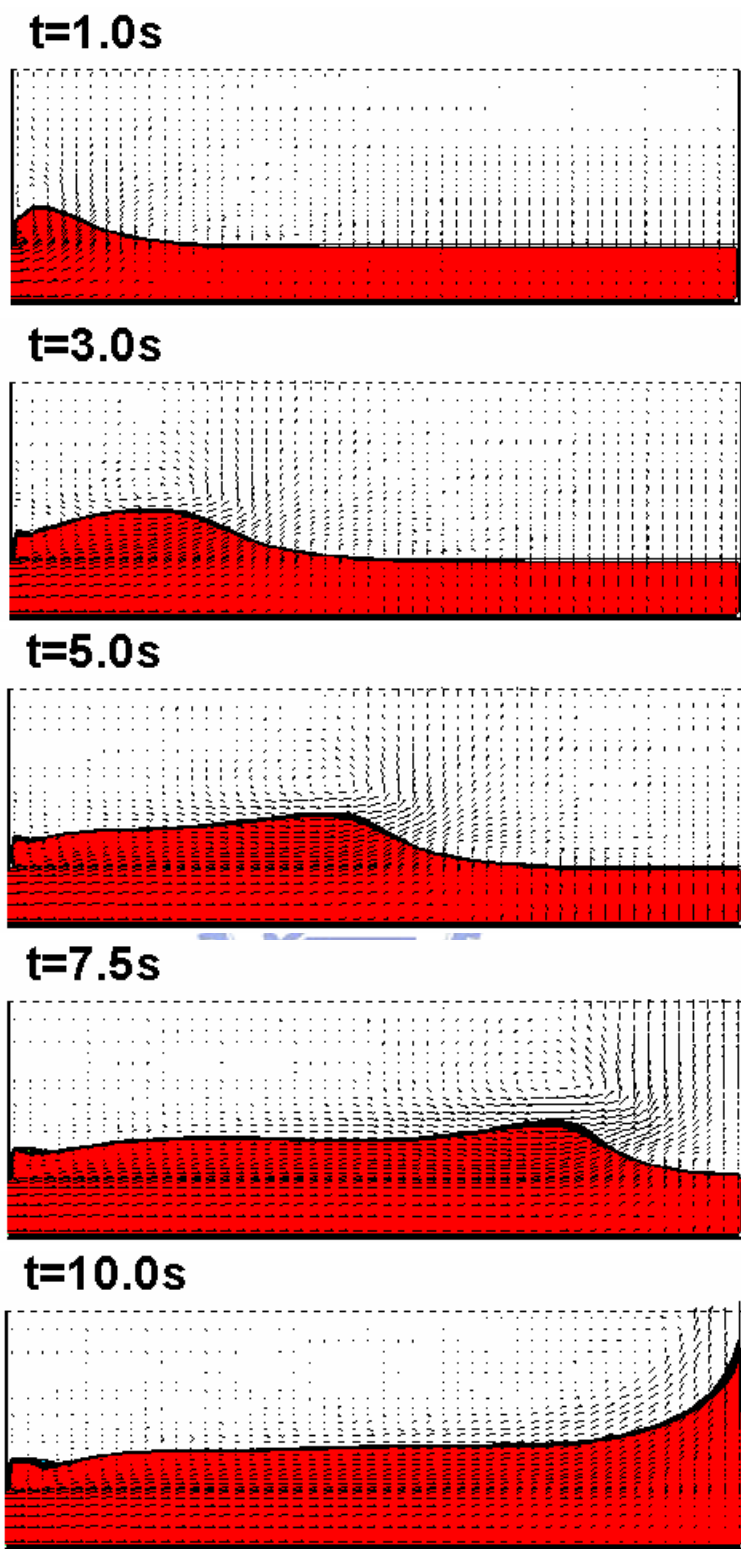
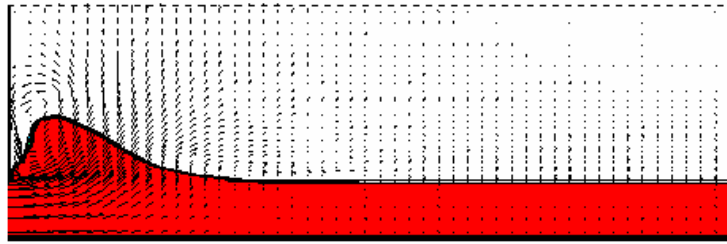
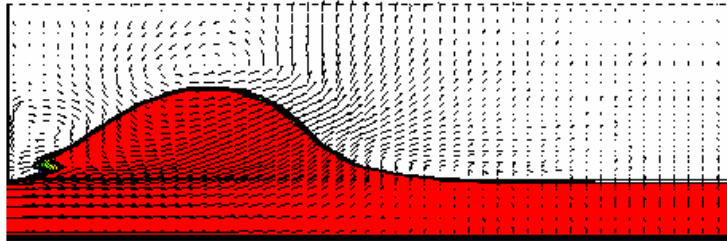


Figure 5.55 Velocity vectors and fluid configuration with velocity $u=1.0$ at inlet.

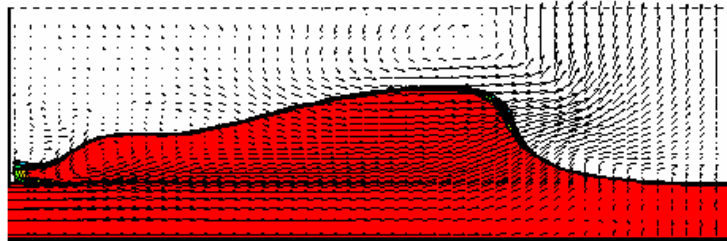
t=1.0s



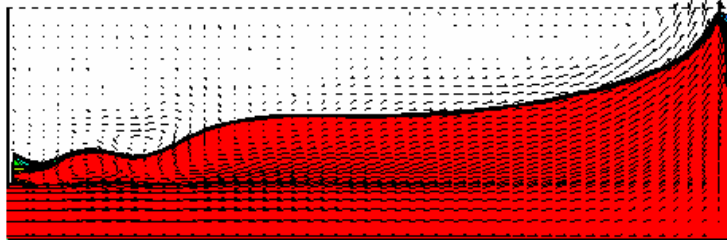
t=3.0s



t=5.0s



t=7.5s



t=10.0s

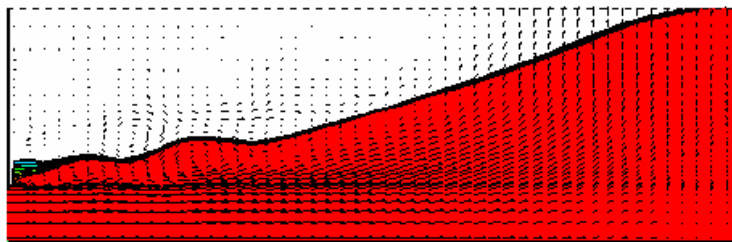
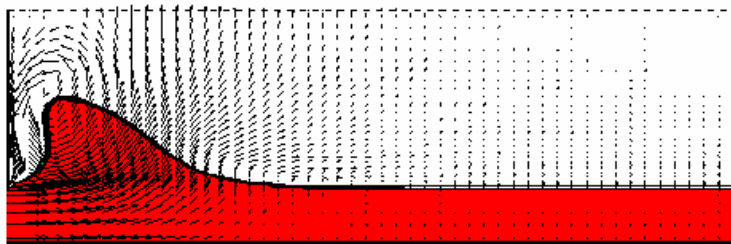
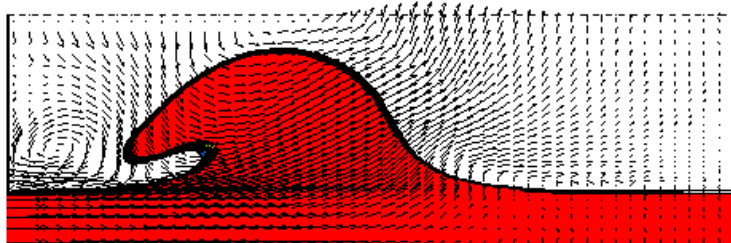


Figure 5.56 Velocity vectors and fluid configuration with velocity $u=2.0$ at inlet.

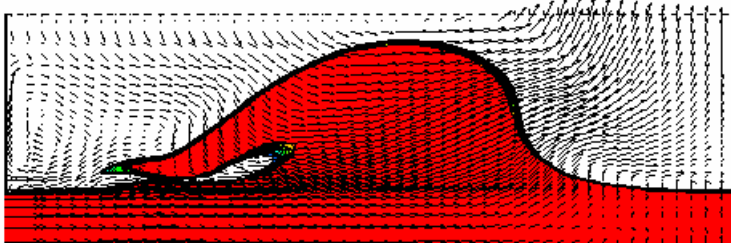
t=1.0s



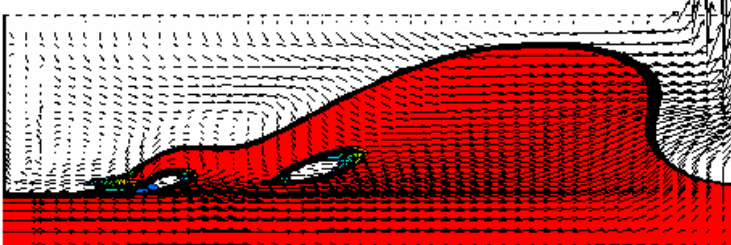
t=3.0s



t=4.0s



t=5.0s



t=6.0s

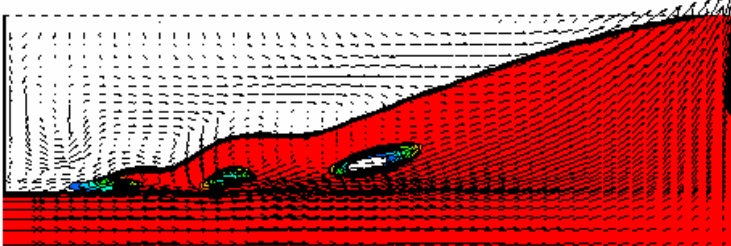


Figure 5.57 Velocity vectors and fluid configuration with velocity $u=3.0$ at inlet.

Chapter 6 Conclusion and Future Work

The aim of this study is to calculate two fluids flow and develop a robust, accurate and simple scheme by Volume-of-Fluid method. It is based on the solution of an indicator equation which is chosen to be the volume fraction. After a simple test and compared with the well-known HRIC, CICSAM and STACS, a composite scheme which uses the combination of SUPERBEE and MUSCL is adopted. To avoid the divergence and maintain high accuracy in the calculation of velocity field, the convective fluxes of momentum equation uses Van Leer scheme. The numerical results are demonstrated and show that this CFD methodology is well performed.

In addition, because of the investigations of two-fluids flow have many applications, some further improvements of this CFD methodology can be made in the future work. First, the two-fluids simulation can be applied in three-dimensional or axial symmetry for real cases. Besides, the analysis of heat transfer with two immiscible fluids is popular subject in industry, such as the soldering of IC package process, electroplate engineering and metal casting. The heat transfer calculation can be acceded into the numerical simulated system.

Reference

- [1] Jyi-Tyan Yeh, "A VOF-FEM and coupled inkjet simulation", 2001 ASME Fluid Engineering Division Summer Meeting, New Orleans, Louisiana, 2001
- [2] Kamisuki, S. et al., "A low power, small, electrostatically-driven commercial inkjet head", Proc. IEEE MEMS Workshop, Heidelberg, Germany, 25, 1998
- [3] Liou et al., "Three-dimensional simulations of the droplet formulation during the inkjet printing process", Int. Comm. Heat Mass Transfer, Vol.29, No.8, pp. 1009-1118,2002."
- [4] Hirt, C. W. and Nichols, B.D., "Volume of fluid (VOF) method for the dynamics of free boundaries", J. Comput. Phys., Vol. 39, pp. 201-225, 1981.
- [5] Feziger, J. H. and Peric, M., "Computational methods for fluid dynamics", Heidelberg: Springer, 1996.
- [6] Daly, B. J., "A technique for including surface tension effects in hydrodynamic calculations," J. Comput. Phys., Vol. 4, pp.97-117, 1969.
- [7] Nichols, B. D. and Hirt, C. W., "Calculating three-dimensional free surface flows in the vicinity of submerged and exposed structures," J. Comput. Phys., Vol. 12, pp, 234-246, 1973.
- [8] Osher, S. and Sethian, J. A., "Front propagating with curvature-dependant speed: algorithms based on Hamilton-Jacobi formulations," J. Comput. Phys., Vol.79, pp.12-49, 1988.
- [9] Harlow, F. H. and Welch, J. E., "Numerical calculation of time-dependent viscous incompressible flow of fluid with free surface", Phys. Fluids, Vol. 8, No.12, pp. 2182-2189, 1965.
- [10] Chen, S., Johnson, D. B. and Raad, P. E., "Velocity boundary conditions for the simulation of free surface fluid flow", J. Comput. Phys., Vol.116, No.2, pp. 262-276, 1995.
- [11] Noh, W. F. and Woodward, P. R., "SLIC (Simple Line Interface Method)", Lecture Note in Physics, Vol. 59, pp. 330-340, 1976
- [12] Youngs, D. L., "Time-dependent multi-material flow with large fluid distortion", in K. W. Morton and M. J. Baines (eds), Numerical Methods for Fluid Dynamics, Academic, New York, pp. 273-285, 1982.

- [13] Rider, W. J. and Kothe, D. B., "Reconstructing volume tracking," J. Comput. Phys., Vol. 141, pp. 112-152, 1998.
- [14] Ramshaw, J. D. and Trapp, J. A. "A numerical technique for low-speed homogeneous two-phase flow with sharp interfaces", J. Comput. Phys., Vol. 21, pp. 438-453, 1976.
- [15] Shyy, W. , Thakur, S. and Wright, J., "Second-order upwind and central difference schemes for recirculating flow computation", AIAA Journal, vol.30, pp. 923-932, 1992.
- [16] Leonard, B. P., "A stable and accurate convective modeling procedure based on quadratic interpolation", Computer Methods in Applied Mechanics and Engineering, Vol.19, pp.56-98, 1979.
- [17] Zalesak, S. T. , "Fully multi-dimensional flux corrected transport algorithms for fluid flow", J. Comput. Phys., Vol.31, pp.335-362, 1979.
- [18] Rudman, M., "Volume-tracking methods for interfacial flow calculations", Int. J. Numer. Methods Fluids. Vol. 24, pp.671-691, 1997.
- [19] Leonard, B. P., "Simple high-accuracy resolution program for convective modeling of discontinuities", In. J. Numer. Methods Fluids, Vol. 8, pp.1291-1318, 1988
- [20] Harten, A. "High resolution schemes for hyperbolic conservation laws", J. Comput. Phys., vol.49, pp. 357-393, 1983.
- [21] Van Leer, B., "Towards the ultimate conservative difference scheme. II . Monotonicity and conservation combined in a second-order scheme", J. Comput. Phys., Vol.14, pp.361-370 1974.
- [22] Sweby, P. K., "High resolution schemes using flux limiters for hyperbolic conservation laws", SIAM J. Numer. Analysis., Vol.21, No.5, pp. 995-1011, 1984.
- [23] Gaskell, P. H. and Lau, A. K. C., "Curvature-compensated convective transport: SMART, a new boundedness-preserving transport algorithm." Int. J. Numer. Meth. Fluids, vol. 8, pp. 617-641, 1988.
- [24] Jasak, H., Weller, H. G. and Gosman, A. D., "High Resolution NVD Differencing Scheme for Arbitrary Unstructured Meshes", Int. J. for Numer. Meth. Fluids, vol. 31, pp.431-449, 1999.
- [25] Roe, P. L., "Large scale computations in fluid mechanics, Part2", In Lectures in Applied

- Mathematics, Vol. 22, pp. 163-193, 1985.
- [26] Darwish, M. S., "A new high-resolution scheme based on the normalized variable formulation", Numer. Heat Trans, Part B, Vol. 24, pp. 353-371, 1993.
- [27] Van Leer, B., "Towards the Ultimate Conservative Difference Scheme V. A Second-Order Sequel to Godunov's Method", J. Comput. Phys., vol. 135, No.2, pp. 229-248, 1997.
- [28] Muzaferija, S., Peric, M., Sames, P. and Schellin, T., "A Two-Fluid Navier-Stokes Solver to Simulate Water Entry", Twenty-Second Symp. On Naval Hydrodynamics, Washington, D.C., pp.638-649, 1998.
- [29] Darwish, M. and Moukalled, F., "Convective schemes for capturing interfaces of free-surface flows on unstructured grids.", Numer. Heat Trans., Part B, 49, pp.19-42, 2006
- [30] Ubbink, O., "Numerical prediction of two fluid systems with sharp interfaces," thesis submitted from Department of Mechanical Engineering Imperial College of Science, Technology & Medicine, January 1997.
- [31] Issa, R. I., "Solution of the implicitly discretised fluid flow equations by operator-splitting," J. Comput. Phys, Vol.62, pp. 40-65, 1985.
- [32] Brackbill et al., "A continuum method for modeling surface tension", J. Comput. Phys, vol.100, pp. 335-354, 1992.
- [33] Batchelor, G. K., "An introduction to fluid dynamics," Cambridge: Cambridge University Press, 1967.
- [34] Adamson, A. W., "Physical chemistry of surfaces," New York: John Wiley & Sons, 1976.
- [35] Orlanski, "A simple boundary condition for unbounded hyperbolic flows", J. Computational Physics, vol.21, pp.251-269, 1976
- [36] Ubbink, O. and Issa, R. I., "A method for capturing sharp fluid interfaces on arbitrary meshes," J. Comput. Phys., Vol. 153, pp.26-50, 1999.
- [37] Lafaurie, B., et al., "Modeling merging and fragmentation in multiphase flows with SURFER," J. Comput. Phys., Vol. 113, pp.134-147, 1994
- [38] Puckett, E. G., et al., "A high-order projection method for tracking fluid interfaces in

- variable density incompressible flows,” J. Comput. Phys., Vol. 130, pp. 269-282, 1997.
- [39] Raad, P. E., Chen, S. and Johnson, D. B., “The introduction of micro cells to treat pressure in free surface fluid flow problem,” J. Fluids Engineering, Vol. 117, pp.683-690, 1995.
- [40] Martin, J. C. and Moyce, W. J., “An experimental study of the collapse of liquid columns on a rigid horizontal plane,” Philos. Trans. Roy. Soc. London, Vol. A244, pp.312-324, 1952.
- [41] Koshizuka, S., Tamako, H. and Oka, Y., “A particle method for incompressible viscous flow with fluid fragmentation,” Comput. Fluid Dynamics JOURNAL, Vol.4(1), pp.29-46, 1995.
- [42] Stoker, J. J., “Water waves,” New York: John Wiley & Sons, 1958.

